UNIVERSITY OF CALIFORNIA SAN DIEGO

Tunable Optical Frequency Comb Assisted Radio Frequency Receiver

A dissertation submitted in partial satisfaction of the
requirements for the degree Doctor of Philosophy

in

Electrical Engineering (Photonics)

by

Daniel Esman

Committee in charge:

Professor Stojan Radic, Chair
Professor Leonid Butov
Professor Joseph Ford
Professor Shayan Mookherjea
Professor Oleg Shpyrko

2017

The Dissertation of Daniel Esman is approved, and it is acceptable in quality and form for publication on microfilm and electronically:

_____

_____

_____

_____

_____

Chair

University of California, San Diego

2017

DEDICATION

To my family.

TABLE OF CONTENTS

LIST OF FIGURES

LIST OF ABBREVIATIONS

ADC	Analog to Digital Converter
AWG	Arrayed Waveguide Grating
BPSK	Binary Phase Shift Keyed
CMOS	Complementary metal-oxide-semiconductor
CS	Cyclostationary
DAC	Digital to Analog Converter
DCI	Detect Classify and Interpret
DFT	Discrete Fourier Transform
DSP	Digital Signal Processing
DSSS	Direct Sequence Spread Spectrum
EDFA	Erbium-doped fiber amplifier
ENOB	Effective Number of Bits
E-YDFA	Erbium and Ytterbium Doped Fiber Amplifier
FFT	Fast Fourier Transform
FH	Frequency Hopping
FLOPS	Floating Point Operations Per Second
FOM	Figure of Merit
FWM	Four wave mixing
HNLF	Highly nonlinear fiber
LO	Local Oscillator

ML	Master Laser
MPI	Multi Path Interference
MZM	Mach-Zehnder Modulator
NFoM	Nonlinear Figure of Merit
NOLM	Nonlinear Optical Loop Mirror
OFC	Optical Frequency Comb
OSNR	Optical signal-to-noise ratio
PG	Pattern Generator
PM	Phase Modulator
PPM	Pulse Position Modulation
PRBS	Pseudo-random bit sequence
PSD	Power Spectral Density
QPSK	Quadrature Phase Shift Keyed
RF	Radio Frequency
SBS	Stimulated Brillouin Scattering
SCF	Spectral Correlation Function
SNR	Signal-to-noise ratio
SPM	Self-phase modulation
STFT	Short Time Fourier Transform
TM	Time Modulated
UWB	Ultra-Wideband
WDM	Wavelength Division Multiplexer

WGN	White Gaussian Noise

ACKNOWLEDGEMENTS

I owe my deepest gratitude to the many people that have helped me directly or indirectly complete this dissertation. First, I would like to thank my advisor, Professor Stojan Radic, for his never ending support and understanding. His persistent motivation, support, scientific intellect, and acceptance to suggestions have encouraged me to strive for excellence and allowed for unconventional thinking in many different research projects. His attitude towards proposed research topics and scientific results have only made me strive to do more.

Second, I would like to thank my committee members, Professor Stojan Radic, Professor Shayan Mookherjea, Professor Joseph Ford, Professor Leonid Butov, and Professor Oleg Shpyrko for their constructive comments and guidance through this dissertation and defense talk.

I am grateful to the Department of Electrical and Computer Engineering at the University of California, San Diego for providing financial support over the past four years. I would also like to thank the support of Defense Advanced Research Projects Agency for providing the funding for part of this work.

Upon entering the Photonic Systems lab, I had the fortune to work closely with Dr. Andreas Wiberg on developing photonic assisted analog to digital converters. His guidance and introduction to the lab were essential in building a solid foundation in the lab for the following years. I would also like to acknowledge Dr. Ana Pejkic for her help and knowledge in our collaborative experiments, in addition to providing a template for this thesis. A special thanks is also in order to my colleague and friend

Eduardo Temprana for fruitful experimental discussions, and most importantly for keeping me sane, even in the late hours of the night. After my work on photonic analog to digital converters, I then began working on optical frequency combs with Dr. Vahid Ataie, whose extensive knowledge and efficient work ethic will undoubtedly shape how I work in the future. During these experiments, I also had the privilege to participate in multiple discussions with Dr. Nikola Alic, Dr. Evgeny Myslivets, and Dr. Bill P.-P. Kuo, whose vast knowledge and insight on a number of topics helped tremendously with this thesis work. Also, I would like to thank both past and present members of the lab for their source of encouragement and constructive comments: Dr. Zhi Tong, Dr. Faezeh Gholami, Dr. Ron R. Nissim, Dr. Lan Liu, Dr. Kevin Young, Chris Huynh, Jason Leng, Motohiko Eto, Jin Zhang, Huan Hu, Elham Serahati, and Dr. Liangshun Han.

To my friends, I owe my gratitude for making this journey so much more enjoyable. I wish to also send a special thanks to my friends Jr, Denise, and Brent for always keeping me entertained after work. Finally, I would like to thank my family – my father Rich, my mother Sue, my brother Ben, my sister Beth, and all my nephews and nieces, for their never-ending support and love.

Chapter 4, in part, is a reprint of the material as it appears in the IEEE/OSA Journal of Lightwave Technology, volume 34, issue 22, 5214-5219 (2016), titled "Subnoise Signal Detection and Communication," by Daniel Esman, Vahid Ataie, Bill P.-P. Kuo, Nikola Alic, and Stojan Radic. Chapter 4 also contains in part material submitted for publication as it may appear in the IEEE/OSA Journal of Lightwave

Technology, titled "Comb Assisted Spread Spectrum Subnoise Wireless Communication Link," by Daniel J. Esman, Vahid Ataie, Bill P.-P. Kuo, Nikola Alic, and Stojan Radic. Lastly, Chapter 4 in part is a reprint of the material as it appears in the IEEE/OSA Journal of Lightwave Technology, volume xx, issue xx, x-x (2016), titled “Frequency-Hopping Pulse Position Modulation Ultrawideband Receiver,” by Daniel Esman, Vahid Ataie, Bill P.-P. Kuo, Nikola Alic, and Stojan Radic. The dissertation author was the primary investigator, and the primary author of these articles.

Chapter 5, in part, is a reprint of the material as it appears in the IEEE/OSA Journal of Lightwave Technology, volume 34, issue 24, 5669-5674 (2016), titled "Detection of Fast Events in a Noisy Background" by Daniel Esman, Vahid Ataie, Bill P.-P. Kuo, Eduardo Temprana, Nikola Alic, and Stojan Radic. Chapter 5 also contains in part material submitted for publication as it may appear in the OSA conference proceedings, titled "Comb Assisted Subnoise Microwave Signal Detection," by Daniel J. Esman, Vahid Ataie, and Stojan Radic. The dissertation author was the primary investigator, and the primary author of these articles. Lastly, Chapter 5 in part is a reprint of the material as it appears in the Science Journal, volume 350, issue 6266, 1343-1346 (2015), titled "Subnoise detection of a fast random event" by Vahid Ataie, Daniel Esman, Bill P.-P. Kuo, Nikola Alic, and Stojan Radic. The dissertation author was the primary investigator, and the co-primary author of this article.

Chapter 6, in part or in full is currently being prepared for submission for publication of the material by Daniel. J. Esman, Vahid Ataie, Bill P.-P. Kuo, Eduardo

Temprana, Nikola Alic and Stojan Radic. The dissertation author was the primary investigator, and the primary author of this article.

VITA

2012	Bachelor of Arts, Physics and Mathematics, Kalamazoo College, Kalamazoo, MI, USA.
2014	Master of Science, Electrical Engineering (Photonics), University of California, San Diego, USA.
2017	Doctor of Philosophy, Electrical Engineering (Photonics), University of California, San Diego, USA.

PUBLICATIONS

Journal articles:

Daniel J. Esman, Vahid Ataie, Bill P.-P. Kuo, N. Alic and Stojan Radic, "Subnoise Signal Detection and Communication," Journal of Lightwave Technology, 34(22), 5214-5219 (2016).

Daniel J. Esman, Vahid Ataie, Bill P.-P. Kuo, Eduardo Temprana, Nikola Alic, and Stojan Radic, "Detection of Fast Events in a Noisy Background," Journal of Lightwave Technology, 34(24), 5669-5674 (2016).

Daniel J. Esman, Vahid Ataie, Bill P.-P. Kuo, Nikola Alic, and Stojan Radic, "Frequency-Hopping Pulse Position Modulation Ultrawideband Receiver," (in preparation).

Daniel J. Esman, Vahid Ataie, Bill P.-P. Kuo, Eduardo Temprana, Nikola Alic, and Stojan Radic, "Comb-Assisted Cyclostationary Analysis of Wideband RF Signals," (in preparation).

Daniel J. Esman, Vahid Ataie, Bill P.-P. Kuo, Nikola Alic, and Stojan Radic, "Comb Assisted Spread Spectrum Subnoise Wireless Communication Link," (in preparation).

Ana Pejkic, **Daniel J. Esman**, Andreas O. J. Wiberg, Nikola Alic, and Stojan Radic, “Optimal Detection of ultrafast signals,” (in preparation).

Vahid Ataie, **Daniel J. Esman**, Bill P.-P. Kuo, Nikola Alic, and Stojan Radic, “Subnoise detection of a fast random event,” Science 350(6266), 1343-1346 (2015).

Daniel J. Esman, Andreas O. J. Wiberg, Nikola Alic, and Stojan Radic, "Highly Linear Broadband Photonic-Assisted Q-Band ADC," Journal of Lightwave Technology, 33(11), 2256-2261, (2015).

Andreas O.J. Wiberg, **Daniel J. Esman**, Lan Liu, James R. Adleman, Sanja Zlatanovic, Vahid Ataie, Evgeny Myslivets, Bill P.-P. Kuo, Nikola Alic, Everett W. Jacobs, "Coherent Filterless Wideband Microwave/Millimeter-wave Channelizer based on Broadband Parametric Mixers, Journal of Lightwave Technology, 32(20), 3609-3617, (2014).

Conference proceedings:

Daniel J. Esman, Vahid Ataie, and Stojan Radic, "Photonic Aided Subnoise Microwave Signal Detection," Invited, in Avionics and Vehicle Fiber-Optics and Photonics Conference, and International Topical Meeting on Microwave Photonics, (2016).

Huan Hu, **Daniel J. Esman**, Vahid Ataie, Eduardo Temprana, Nikola Alic, Stojan Radic, "Real-time Discrete Fourier Transform Using Optical Parametric Combs," (in preparation).

Vahid Ataie, **Daniel J. Esman**, Bill P-P. Kuo, Nikola Alic, and Stojan Radic, "Wideband optical parametric frequency comb applications in real-time signal processing," Summer Topicals Meeting Series (SUM), (2015).

Eduardo Temprana, Evgeny Myslivets, Lan Liu, Ana Pejkic, Vahid Ataie, Bill P.-P. Kuo, **Daniel J. Esman**, Andreas O.J. Wiberg, Nikola Alic and Stojan Radic, "Transmission Reach Doubling Enabled by Transmitter-Side Digital Back Propagation and Frequency Referenced Carriers," European Conference on Optical communication (ECOC), Valencia, (2015).

Daniel J. Esman, Andreas O. J. Wiberg, Nikola Alic, and Stojan Radic, "High resolution broadband photonic sampled ADC: 8.0 ENOB at 40 GHz," OECC-ACOFT, Paper TU3E-1 (2014).

Daniel J. Esman, Andreas O. J. Wiberg, Mu-Han Yang, Lan Liu, Bill P.-P. Kuo, Nikola Alic, Stojan Radic, "Photonic parametric sampled analog-to-digital conversion at 100 GHz and 6 ENOBs," European Conference and Exhibition on Optical Communication (ECOC), Paper Mo.3.5.6 (2014).

Daniel J. Esman, Andreas O. J. Wiberg, Eduardo Temprana, Yauheni Myslivets, Bill P.-P. Kuo, Nikola Alic, Stojan Radic, "A fully frequency referenced parametric polychromatically sampled analog-to-digital conversion," Optical Fiber Communication Conference (OFC), Paper TH3D.4 (2014).

Andreas O.J. Wiberg, **Daniel J. Esman**, Lan Liu, Evgeny Myslivets, Nikola Alic, and Stojan Radic, "Photonic RF-Channelized Receiver based on Wideband Parametric Mixers and Coherent Detection," CLEO Science and Innovations, STu2I. 6, (2014).

Andreas O.J. Wiberg, **Daniel J. Esman**, Lan Liu, Zhi Tong, Evgeny Myslivets, Nikola Alic, and Stojan Radic, "Demonstration of 74 GHz Parametric Optical Sampled Analog-To-Digital Conversion," European Conference and Exhibition on Optical Communication (ECOC), Tu.1.C.1 (2013).

Andreas O.J. Wiberg, **Daniel J. Esman**, Lan Liu, Vahid Ataie, Evgeny Myslivets, Bill P.-P. Kuo, Nikola Alic, Stojan Radic, Sanja Zlatanovic, James R. Adleman, and Everett W. Jacobs "Agile Wideband Microwave/Millimeter-wave Analysis by Coherent Filterless Channelizer," 2013 IEEE International Topical Meeting on Microwave Photonics (MWP), Post-deadline paper, (2013).

ABSTRACT OF THE DISSERTATION

Tunable Optical Frequency Comb Assisted Radio Frequency Receiver

by

Daniel Esman

Doctor of Philosophy in Electrical Engineering (Photonics)

University of California, San Diego, 2017

Professor Stojan Radic, Chair

Agile wideband radio frequency receivers capable of not only detecting a signal with high accuracy, but also processing and classifying the data simultaneously is the Holy Grail for receivers spanning applications in defense, communication, nature, and biology. Conventional radio frequency receivers perform poorly over wide bandwidths

and rely on complex electrical processing, limiting the performance and requiring a large dissipation to operate. In this dissertation, a new processing and detection engine is introduced to address both the need for detecting wideband signals and processing them simultaneously. The cornerstone of the engine is the use of two optical frequency combs. The low noise tunable frequency combs allow for an unprecedented engine with agile tuning and computation free processing.

The capabilities of the developed engine are demonstrated across a wide range of applications. Specifically, a subnoise communication link with the potential to solve the current radio frequency spectral drought is introduced with the core enabler being the developed engine. Next, a transient signal detector is proposed with the potential to revolutionize a variety of different fields that require accurate detection of single events. Finally, a signal classification scheme capable of taking a large spectral bandwidth and simultaneously processing the data for signal intelligence is introduced. The core engine for each of these applications is also shown to be packaged into a standard telecommunications box, paving the way for a revolutionary device that is readily implementable across a variety of fields.

Chapter 1 Introduction

The power of desktop computing has transferred to handheld, wireless devices, thanks in part to rapid microprocessor evolution over the last decade [1], [2]. This transfer to mobile devices has not only unified social, scientific, and media functions on a single device, but also required that all these functions be confined to a single, untethered data portal. In contrast to a desktop computer that remains anchored by a wireline, mobile connections reside in strictly regulated, narrow radio frequency (RF) bands [3], [4], [5]. The price for unrestricted mobility is paid in terms of low connectivity: while a common wireline now exceeds 10 Gbps, the entire cellular network is confined to only 765 MHz [4]. Remarkably, the modern mobile network must accommodate all of its users within the spectral range that is four orders of magnitude narrower than that of a single physical wireline [6]. To satisfy the exponentially growing data rates, a transition will likely be made to speed up the current network limitations. Intuitively, increasing the bandwidth for cellular networks will help keep up with the growing data rates. Unfortunately, simply increasing the bandwidth is not a viable solution, as much of the wireless spectrum is already in use [5]. In addition, each receiver would also necessarily need a bandwidth increase, presenting its own set of challenges.

Significant detection challenges also occur in many other fields besides communications. For instance, thanks to many scientific advancements in fields such as

biology, astronomy, physics, and defense, far more advanced detection techniques are required. Specifically, in each of these fields, the observance of fast singular events is of great importance to understanding different phenomena. For example, the detection of neutrinos [7], the decay of a molecule [8], a fast radio-astronomy event [9] and the arrival of a data packet buried in noise [10] are all examples of nonrepetitive phenomena that pose basic detection challenges. Intuitively, if an event is repetitive, detection sensitivity can be significantly enhanced by averaging over time. However, these techniques rely on increasing detection sensitivity by averaging a signal over a period of time, making them unsuitable for detecting a single random event.

1.1. Motivation

The ability to detect, classify and interpret (DCI) signals across the entire RF spectrum poses both fundamental and technological challenges. While high resolution, high-sensitivity DCI can be performed in a local (narrow-band) manner, such spectral analysis is generally not viable over the contiguous RF range (3 kHz-300 GHz) hosting modern communication and sensing applications. The wideband challenge is further compounded by the fact that emission may contain transient, frequency-hopping or spectrally-spread signals that eliminate, even in principle, conventional averaging or fixed-band filtering techniques. The capability to perform DCI for these types of signals is discussed throughout this thesis.

In absence of dissipation, noise, and speed limitations in electronics, DCI across the entire RF range can in principle be implemented using only electronic analog to digital converters (ADC) and processors. Unfortunately, current state of the art all electronic approaches have limited applicability to broadband DCI applications.

Recognizing these limitations, many photonic approaches have been introduced to detect a much larger bandwidth than what is available in electronics [11]. Even still, many of these approaches only convert a signal to the digital domain, but would still require an electric processor to perform signal processing for classification or interpretation. As a result, the ability to not only detect a wideband signal but also process the signal for classification or interpretation is a fundamental challenge.

Correspondingly, a dual optical frequency comb (OFC) setup can be implemented as a pre-processing unit allowing for a significant relaxation in not only the required electrical ADC bandwidth but also the required electrical processing speed. This core engine is used as an agile detector and real time processor for the RF range and is characterized for a variety of previously difficult to detect signals.

1.2. Dissertation Structure

This dissertation begins with trends and challenges in electrical signal processing techniques, indicating its inferiority to the ever growing speed demands in modern applications. Recognizing this main problem, a new dual OFC engine is introduced to relax the necessary electrical signal processing speed. The main theoretical background, OFC design, experiments, and various applications of this core engine is covered throughout this dissertation.

Chapter 2 gives a brief overview of all electrical ADCs and processors including their current trends and limitations. A review of photonic assisted ADCs is presented, showing the potential relaxation of electrical ADCs, yet still being limited by the processing speed of electronics. Finally, the challenges for real time electrical processors are discussed for various applications.

Chapter 3 is dedicated to covering the underlying mechanisms of wave propagation in dielectric media pertinent to this dissertation. Beginning with a linear model of propagation in a dielectric medium, chromatic dispersion and loss are introduced. Next, a nonlinear model is derived with relevant nonlinear processes discussed for nonlinear dielectric medium. Finally, the role of four wave mixing for agile OFC generation is discussed.

The first application of an agile, dual OFC is presented in Chapter 4, for low complexity synchronization and demodulation of a coded signal. The principle of the receiver is introduced with discussion on achieving both accurate synchronization and demodulation of a direct sequence spread spectrum (DSSS) signal. Two experimental verifications, each with their own advantages, are also provided and discussed. Next, the dual OFC is also shown to be able to demodulate a frequency hopping (FH) pulse position modulated (PPM) signal, with the principle of the receiver and experimental verification shown.

The ability for the dual OFC engine to detect non-repetitive phenomena is discussed in Chapter 5. The principle of the receiver is first discussed for extracting subnoise singular events with high confidence. The receiver architecture is demonstrated with two experimental verifications, first with a fully populated backplane and second with an emulated backplane, with the drawbacks and advantages of each discussed. The experimental setup is also used to predict the time of arrival of the event, with discussion on the optimal prediction method shown.

The applicability of the proposed dual OFC to cyclostationary analysis is discussed in Chapter 6. The principle of cyclostationary analysis, and its high

computational complexity are first discussed. Next, the complexity is shown to be significantly reduced by the proposed dual OFC setup. Experimental verifications are then presented utilizing the dual OFC setup to perform DCI with low computational complexity.

Finally, concluding remarks and a summary of the presented work are shown in Chapter 6. Future directions of each research topic are also discussed as potential extensions to this dissertation.

Chapter 2 Current State of the Art

The widespread adoption of digital signal processing (DSP) techniques in application domains spanning communication and sensing in commercial and defense applications mandate ADC functionality operable on the femtosecond time-scale and with uncompromised, high resolution. Currently, the A-to-D performance represents the limiting factor to the successful high speed DSP implementation and utility. The ADC performance, in turn, is limited by its underlying signal to noise ratio (SNR), linearity, aperture jitter, and sampling ambiguity (the width of the sampling gate/aperture) [12]. The state of the art electronic ADCs performance can be seen in [13], showing limited resolution for high speed operation. Prominently, recent advances have shown that these limitations can largely be removed, or mollified by the use of photonic assisted ADCs, thereby circumventing the shortcoming associated with conventional purely-electronic devices [14]. Indeed, photonic assisted ADCs have become a practical means to improving high accuracy in high speed signal detection and/or sensing. The basic advantage of these hybrid architectures lay in their ability to effectively combine the fast sampling techniques of photonics while relying on processing capabilities of electronics. As a result, with sufficient increase in ADC performance, the limiting factor for high speed DSP utilization will shift from the ADC to the electronic processing power.

A variety of photonic sampling frontends for real-time data acquisition have been implemented previously. Specifically, fast optical gates can be constructed by utilizing ultrashort optical pulses and as a front-end to assist in the electrical digitization. Such devices can be made employing parallel gates [15], sub-rate sampling

of high frequencies at multiple wavelengths [16] or polychromatic sampling [17]. Yet another class of implementations include sampling by an optical modulator. In all cases, the performance of the architecture, denoted by the effective number of bits (ENOB) or resolution, is significantly enhanced compared to their electrical counterpart under the same bandwidth considerations.

The ADC comparison first defined in [12] has long been used to compare performance measures of Nyquist sampled ADCs. However, for many photonic assisted ADCs, Nyquist sampling is not achieved, and subsampling is used instead. The subsampled ADCs possess an additional feature that needs to be taken into account for a rigorous comparison. For instance, a subsampled system performing with 8 ENOB at 20 GHz signal frequency and with a 10 GHz operational bandwidth is a superior architecture than one operating with the same resolution (i.e. 8 ENOB) and carrier frequency (i.e. 20 GHz) operating over 10 MHz available bandwidth. As a result, a new figure of merit (FOM) was introduced in [18] which is better suited to sub-sampled ADCs. The proposed FOM encapsulates the performance of single tone input ADCs, based on ENOBs, N, operational bandwidth, Δf, and signal carrier frequency, f_c. In particular, the FOM is defined as follows:

$$FOM = 2^N \sqrt{\Delta f} f_c \tag{2.1}$$

It should be emphasized that a system characterized at f_c with available bandwidth Δf should have the same FOM as the same system characterized at $2f_c$, Δf (if jitter limited), or at f_c, $4\Delta f$ (if noise limited), as N should reduce by 1 in either latter case. Thus, this FOM correctly includes the bandwidth that is missing from the analysis of Nyquist-sampled ADCs in [12]. Finally, as shown in Figure 2.1, taking the all-

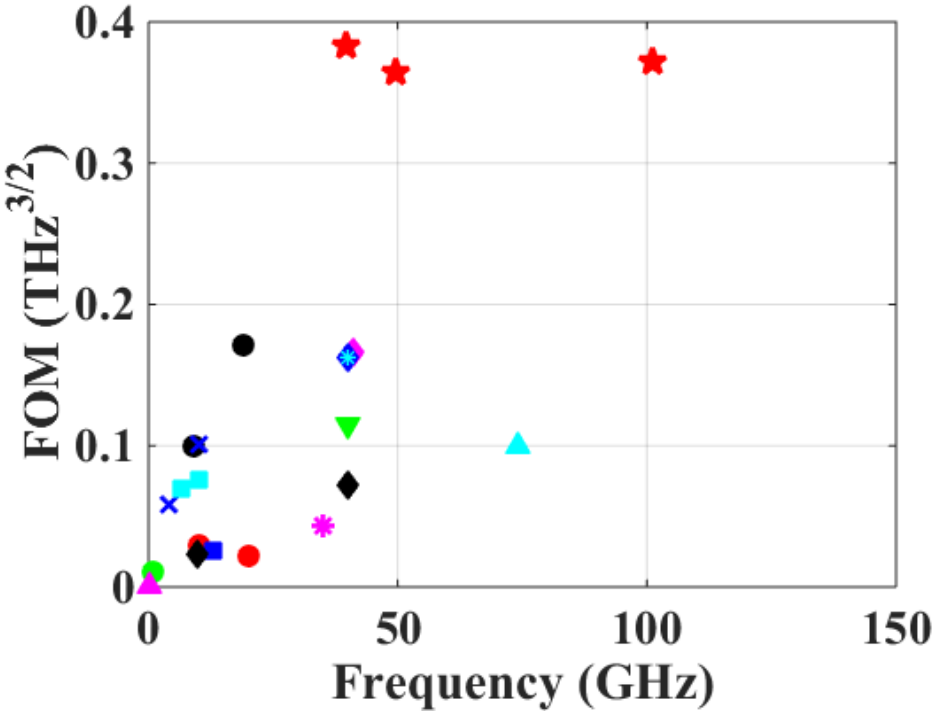

Figure 2.1 Figure of merit as a function of input signal frequency for existing photonic assisted ADC architectures. References for each point in the plot can be found in [18].

important (for sub-sampled ADCs) operational bandwidth parameter into account the performance of photonic assisted ADCs has been steadily increasing. While photonic assisted ADC architectures parallelize the electronic digitization, yielding a greatly reduced bandwidth, full bandwidth processing, or stitching all parallelized channels together necessitates that the electrical processing speed be at least as fast as the full field being analyzed. This sets an important limitation if the field to be analyzed is wideband.

Unfortunately, even if arbitrary resolution and bandwidth exists for any type of ADC, the overall performance of the detection and processing will be limited by the processing speed and precision of electronics. Many processing schemes rely on fast, high precision fast Fourier transforms (FFT) before subsequent processing. While high

precision is indeed possible in conventional electronic FFT processors, operating at sub-GHz rates [19], this is not viable at rates of interest here (10s of GHz) that remain nearly two orders of magnitude higher. The complexity-bandwidth FFT limit is deceptively similar to the familiar argument used in general-purpose processors, where one hopes to match any processing gain by a decrease in feature size. Unfortunately, this cannot be made in case of an FFT complementary metal-oxide-semiconductor (CMOS) architecture that underpins nearly all electrical processors. An FFT algorithm critically relies on multiplication and addition operations [19], with a multiplier CMOS cell dominating its dissipation [19]. In addition, any increase in FFT bit precision imposes a quadratic increase in gate count [20]. Even if one assumes that the gate increase can be accomplished with ideal gate-to-gate connectivity (i.e. zero-dissipation, at any operating rate), this effectively means that the FFT core precision still imposes at least a quadratic dissipation law. In practical terms, a two-order increase in operating speed is likely to lead to unsurmountable connectivity loss and unsustainable heat dissipation [21]. Thus, while photonic ADC architectures have aided to push the total bandwidth that can be processed to higher frequencies, if an FFT must be performed after reception, it is the electrical processing speeds that fundamentally limit a receiver architecture at these high frequencies.

2.1 Spread Spectrum Receivers

The widening gap between wireless RF capacity and a physical wireline can be, at least in principle, altered if interference-free transmission across the entire RF range were possible. To operate freely across the entire physically available range

(>100GHz), the transmitted signal must remain well below a regulated level. In practical terms, the signal can be allowed to exist in any band, as long as its power spectral density (PSD) remains small enough, i.e. if the signal resembles naturally occurring noise. In recent work [22], it was shown that a subnoise signal can indeed be detected, even when represented by a random, nonrepetitive event where conventional averaging is ineffective, even in principle. Unfortunately, detection of a randomly occurring signal event is necessary but not sufficient for construction of a sub-noise communication link with arbitrarily low PSD. This important fact was recognized early by spread-spectrum communication that sought to minimize interference and share bandwidth with many users [23], [24], [25]. Indeed, spectrum regulation can be circumvented by suppressing the signal PSD below a strictly defined level, as shown in Figure 2.2. In a spread-spectrum link, data is rapidly modulated by a specific sequence (code) to produce a waveform with much wider bandwidth. Intuitively, the PSD can be arbitrarily lowered by a mere increase in code rate, implying that regulation-free transmission across the entire RF range can be easily attained. As an illustration, to reduce the PSD of a MHz-wide channel by 10,000 times, its physical bandwidth should be increased to 10 GHz. While multi-GHz modulation is easily accomplished [26], the reconstruction (decoding) of 10 GHz-wide spread-spectrum channel poses a basic challenge. The received signal must be synchronized to within a fraction of 100 ps, sampled and quantized at the spreading rate (10 GHz) and finally correlated with the code (spreading keyword). In addition to this decoding challenge, the interference generated by different arrival paths at the receiver must be processed out [27], [28], [29]. All these can be accomplished, at least in principle, by computing the Fourier

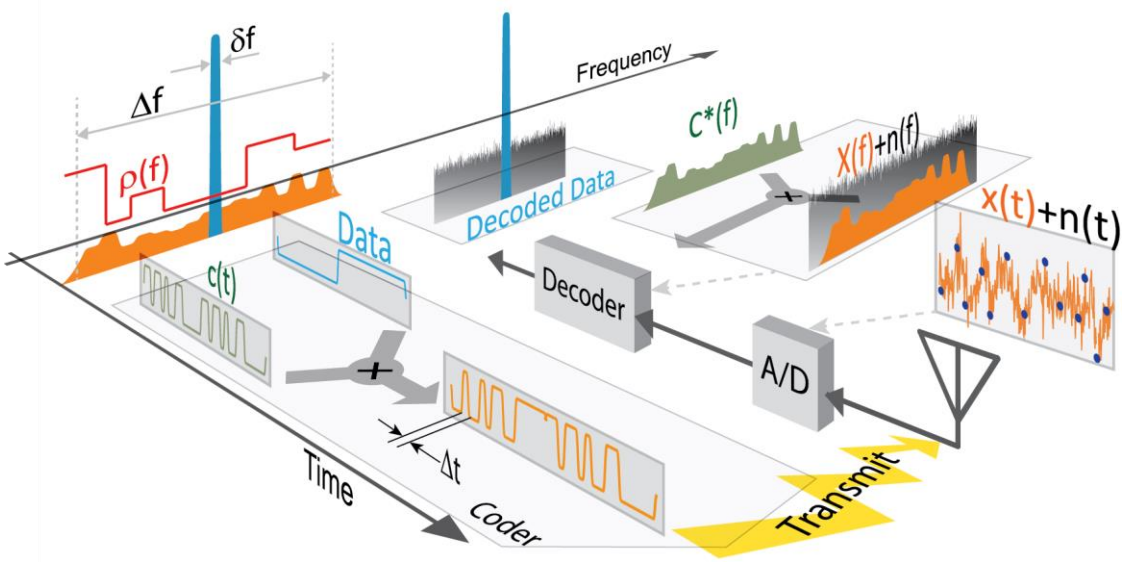

Figure 2.2 Spread-Spectrum Transmission. To transmit a signal in an interference-free manner, signal bandwidth δf is broadened to Δf, reducing its power spectral density below the band-regulated level $\rho(f)$. Spectral broadening is achieved by imposing a unique codeword $c(t)$, modulated at chip rate Δf. A transmission impaired, spectrally broadened signal must be sampled at the spreading rate (Δf) and subsequently decoded in real time. The decoding requires codeword synchronization with sub-chip precision and can be achieved in spectral domain by a single multiplication; $C(f)$ - Fourier transform of the codeword; $x(t)$ and $X(f)$ - received signal and its Fourier transform; n – reception noise.

transform of the received signal in real time. Unfortunately, for a 10 GHz-wide spreading, the last requirement calls for electronic processors approaching 10^{12} floating-point operations per second (FLOPS), well outside the mobile dissipation envelope [30], [31].

However, if the spread-spectrum signal does not have to be digitized at the spreading rate and its Fourier decomposition can be obtained in a computation-free, rate-invariant manner, then an arbitrarily wide spectral spreading becomes viable. The experiments presented in Section 4.1 and Section 4.2 show that data from a spread-spectrum channel can be recovered in the physical domain, without resorting to a high-speed electronic processor. In Section 4.1, to demonstrate the new principle, a 20 MHz wide signal was spectrally spread over 6 GHz by direct-sequence modulation and

decoded in the presence of noise. Encoded information was recovered by a single-step multiplication of the received signal and the spreading sequence in the physical domain. In Section 4.2, a 1 MHz wide signal was spread over 10 GHz by direct-sequence modulation and subsequently synchronized and demodulated to achieve 40 dB of processing gain. The measurements prove that a wideband, spread-spectrum channel can be reconstructed asynchronously, even when accompanied by a noise that exceeds signal power by ten-fold, across the entire signal spectrum.

2.2 Cyclostationary Analyzers

To detect and classify a wideband signal in a contested electromagnetic environment, it is necessary to discriminate a deterministic waveform from stochastic or quasi-stochastic radiation. A practical solution for noise discrimination was provided early [32] and embedded in modern cyclostationary (CS) and cumulant receivers [32], [33]. Intuitively elegant, CS analysis separates signal and stochastic interference using a simple criterion: a modulated waveform is periodically correlated, while noise remains inherently uncorrelated. Since its introduction, the CS approach, and its generalization (cumulant analysis), has been adopted in a broad range of applications, including communications [33], atmospheric sciences [34], [35], [36], machinery [37], biology [38], and econometrics [39].

A CS receiver separates signal from noise (interference) by taking advantage of the cyclical nature of any modulation format. To illustrate this principle, assume that the received radiation $r(t)$ can be written as a summation of modulated signal $s(t)$ and noise $n(t)$ contributions:

$$r(t) = \sum_{m} \Pi(mT)B(t - mT) + n(t) \tag{2.2}$$

where a cycle modulation waveform is denoted by Π, with modulation cycle duration *T* and encoded data by *B*. While the modulated signal portion of the received field is not strictly periodic, its autocorrelation $R_r(t) = \langle r(t)r(t-\tau)' \rangle$ is [32]:

$$R_r(t, \tau) = R_r(t + T, \tau) \tag{2.3}$$

Since the autocorrelation is temporally periodic, one can define the Fourier transform [32] using the auxiliary variable α:

$$R_r^{\alpha}(\tau) = \lim_{r\to\infty} \frac{1}{T} \int_{T} r\left(t + \frac{\tau}{2}\right) r\left(t - \frac{\tau}{2}\right)^{*} e^{-j2\pi\alpha t} dt \tag{2.4}$$

Finally, by mapping the last expression to the Fourier domain:

$$S_r^{\alpha}(f) = \int_{-\infty}^{\infty} R_r^{\alpha}(\tau)\, e^{-j2\pi f\tau} d\tau \tag{2.5}$$

one has defined the well-known spectral correlation function (SCF) that represents a complex transform in 2-dimensional α-f space.

The power of cyclostationary analysis is in its ability to discriminate between signal and noise. An example of an SCF function is plotted in Figure 2.3. Indeed, in case when the received waveform is white noise, its spectral components will exhibit no correlation, requiring that the SCF function vanishes for $\alpha \neq 0$. Conversely, signal features are prominent at non-zero α locations (α-f plane), providing for effective discrimination means between signal and noise, as seen in Figure 2.3. Unfortunately, the practical advantages of a CS analyzer fade when the signal bandwidth exceeds the speed of a viable electronic processor. Indeed, while real-time CS analyzers can be operated over sub-GHz bandwidths [40], [41], none, to the best of the author's knowledge, has approached a sizeable fraction of the contiguous RF range. To obtain

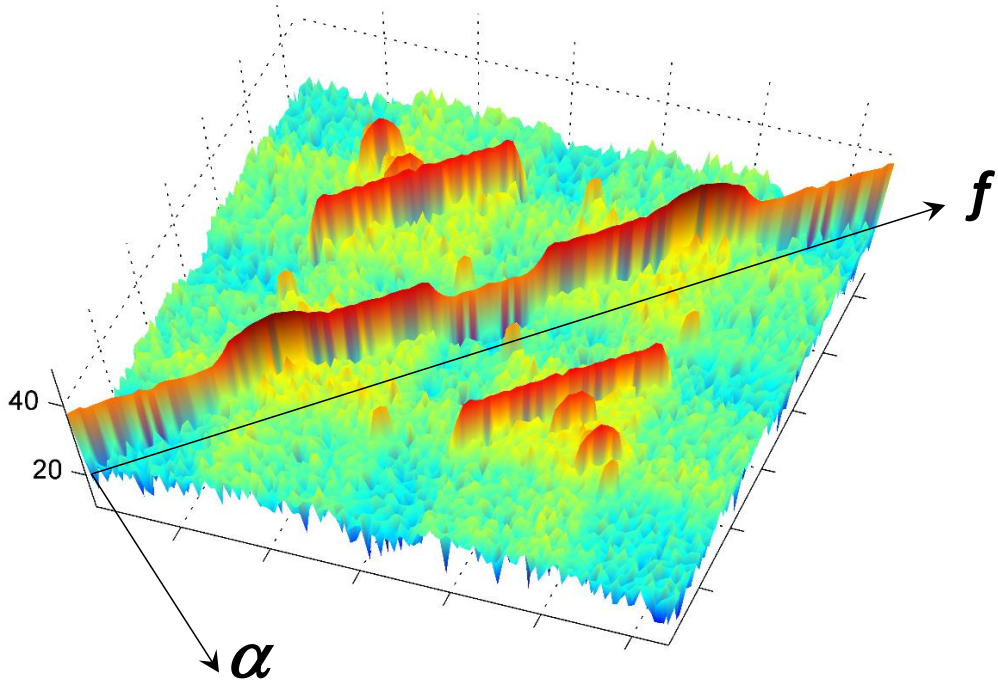

Figure 2.3 Two dimensional spectral correlation function (SCF) example.

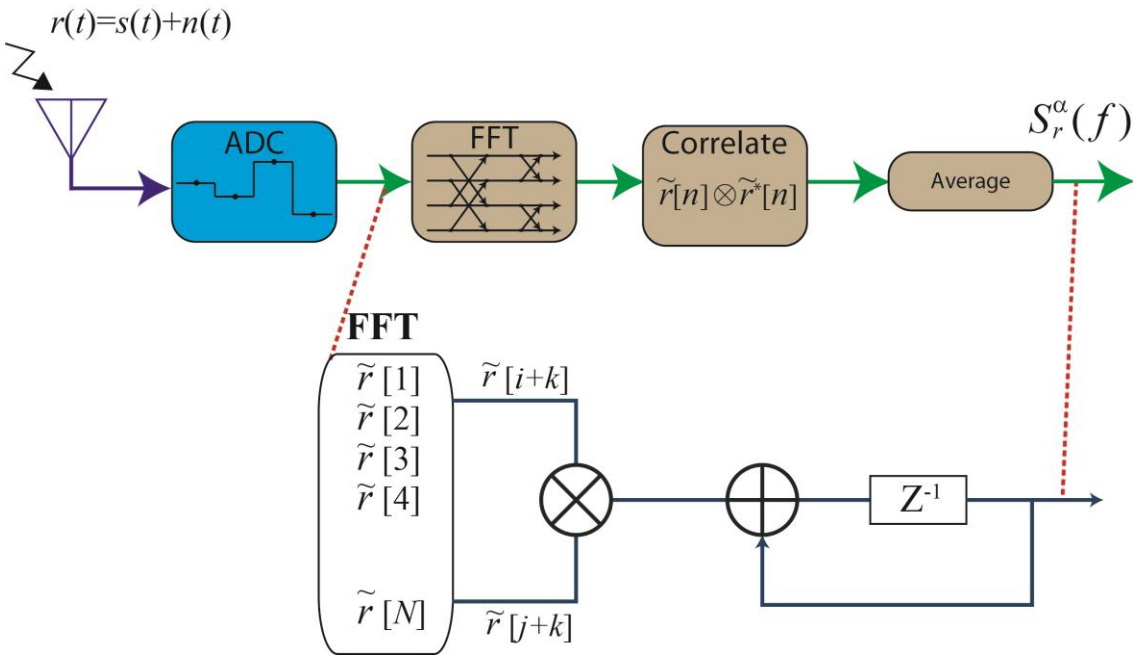

Figure 2.4 Conventional digital CS receiver architecture.

the 2-dimensional SCF mapping, a CS analyzer must use a chain of high-complexity processing blocks, as shown in Figure 2.4. The received signal is first digitized (ADC) and then subsequently mapped to the Fourier domain (FFT). After the spectral representation is obtained, spectral correlation is computed in order to generate the two-dimensional SCF representation, discriminating the noise. To analyze a wide RF range, a CS analyzer must possess an ADC that matches the received signal bandwidth. A wideband ADC poses the first processing challenge that can be quantified in terms of precision, operating bandwidth and dissipation. While an ADC capable of contiguous RF range is unlikely to be constructed in the near future [13], circuits operating beyond 20 GHz have been reported [13]. Assuming that an RF bandwidth of 100 GHz can be addressed by a combination of multiple ADC stages, such a compound digitizer would still dissipate nearly 100 Watts. Even if this were acceptable in a select set of CS applications, the ENOB of such a digitizer will strictly limit its utility. Indeed, while

recently reported ADC demonstrations were performed at rates above 20 GHz these still possess ENOB ~ 7 [13]. Limited digitizer precision is critical since it precludes, even in principle, classification of a high-complexity or closely spaced signals.

While an ADC imposed limit might indeed appear formidable, it is both the computational complexity and precision of the FFT processor as well as the computation of the correlation over large bandwidths that sets the fundamental limit on any CS construction. While much work has been done to reduce the computational complexity of the correlation computation [42], [43], [44], they still rest on a high precision, fast FFT. To understand this important notion, consider a case when one must detect and classify a spread-spectrum signal in presence of noise or interference.

A spread-spectrum channel carrying information x[k] (at kth bit of the transmitted stream) is modulated using a codeword c[k] at a much higher rate (chip-rate) [25], as discussed in section 2.1, and shown in Figure 2.5a. To understand the FFT-imposed limit, consider having to identify two different users each using two distinct codewords. In the complex Fourier plane (Figure 2.5b), with an increase in codeword length (N), the distance between the complex coefficients of the codeword in I-Q plane decreases. As an upper bound of the precision required to distinguish between two signals modulated by different codewords, it is sufficient to resolve the two closest points between codewords in I-Q constellations, as shown in Figure 2.5b (inset). This means that in this case, the FFT precision should be sufficient to resolve the smallest distance between two codeword points in the I-Q plane. Undeniably, this least upper bound on FFT precision will be much more stringent in a more practical situation. This can be understood in the case when signal time of arrival is unknown, yielding a

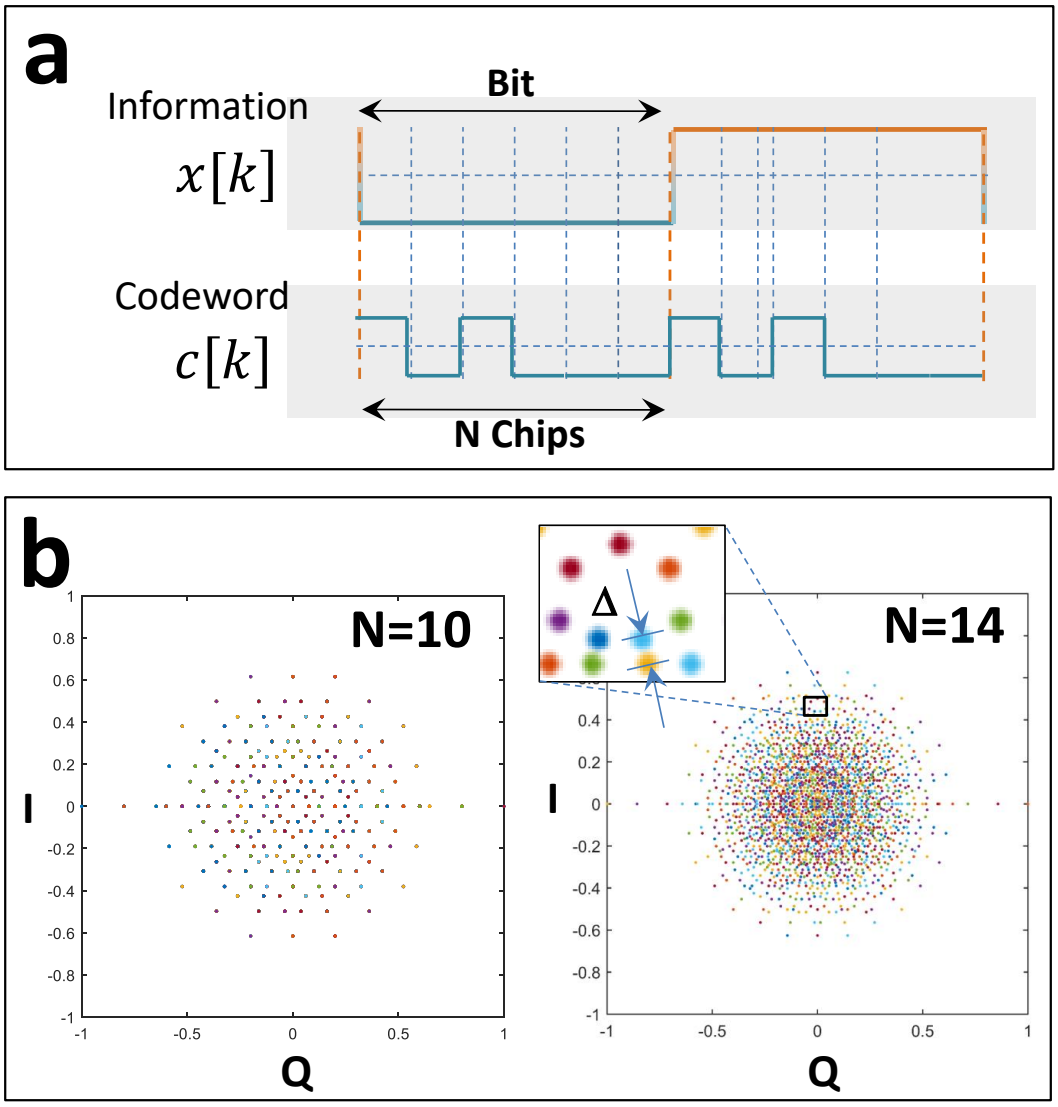

Figure 2.5 Spread-Spectrum Signal representation in Fourier domain: all possible combinations of direct-sequence coding is plotted for codeword length N = 10 (bottom left) and N = 14 (bottom right).

complex rotation amongst each of the codewords in the complex Fourier plane. This in

turn greatly reduces the distance between two coefficients, and hence, mandating a much higher FFT precision. While conventional (electronic) processors rely on a fast FFT algorithm [19], its complexity still prevents real-time processing at UWB rates. As a result, the combined (ADC/FFT) processing barrier imposes a strict limit on the cyclostationary receiver performance. A new receiver approach is introduced and discussed in Section Chapter 6 that circumvents these processing barriers and allows for the reception, analysis, and classification of broadband signals.

2.3 Pulse Position Modulation

The arrival of fast RF modulation has enabled a diversified family of ultra-wideband (UWB) transceivers [27], [45], [46]. The inherent advantages of a UWB link include power-efficient transmission [45], [47], [48], resistance to interference [45], multipath distortion [45], [49], and band-reuse [50]. A common feature in all systems, defined by regulations [51], is large physical bandwidth, exceeding 0.5 GHz in all cases. In practice, this means that a sub-nanosecond pulse is generated and manipulated in order to code a channel either in time or frequency domain. Early UWB work focused on time-modulated (TM) UWB emitters [45], [51], resembling, in its simplest form, well-known PPM. In contrast to a classical PPM scheme, often used with deep-space optical links [52], TM-UWB time reference is often dithered by a tailored quasi-random sequence in order to suppress channel spectral density [48] and equalize it across an allocated band [45]. Similarly, FH coding was also developed, particularly to minimize spectral channel density at “crowded” bands and to provide for adaptive

spectral provisioning [50]. In both schemes, strict temporal reference is absent and the correlator plays a critical role within the receiver. The incoherent nature of such a UWB link also puts high spectral efficiency coding such as pulse-amplitude modulation at a distinct disadvantage [49].

In addition to complying to non-interference regulation, useful wireless transceiver technologies must also bypass multipath propagation, interference from other devices, intentional jamming and provide either a physical or coding security layer. Consequently, conventional (time-referenced) PPM, formed with ultrashort pulses, cannot achieve these requirements. However, if UWB PPM is combined with fast frequency hopping, then goals of regulation-compliant spectral utilization, multi-access links, and low probability of intercept become realistic. Indeed, by combining FH with PPM will not only eliminate fixed harmonics seen in fixed time-frame TM-UWB [48] but will also add a level of link security not inherent in adaptive-band UWB links [50].

The qualities that make FP-PPM modulation attractive also pose a significant reception problem. Firstly, UWB pulses with bandwidth in excess of GHz need to be utilized in order to spread the signal in frequency domain and suppress the spectral power density below the FCC-specified power threshold [51]. Secondly, the introduction of frequency-hopping mandates an additional bandwidth at the receiver, in excess of PPM-only detection. While an excess frequency bandwidth requirement can be addressed by incorporating a set of local oscillator's and mixers at the receiver [53], this solution is not applicable in dissipation constrained receiver architectures. Thus, to address the bandwidth challenge, a sufficient ADC possessing speed must be utilized.

While possible, at least in principle, the use of a high-bandwidth ADC imposes a practical challenge for a multi-GHz-wide channel [13]. Conversely, when the physical bandwidth of FH-PPM link exceeds 10 GHz, this challenge also becomes fundamental as it induces a runaway dissipation requirement [13]. A new receiver approach is introduced in Section 4.3 to bypass the detection challenges of receiving a FH-PPM broadband link.

2.4 Transient Signal Detection

Observation of random, non-repetitive phenomena is of critical importance in astronomy [9], spectroscopy [54], biology [8] and remote sensing [55]. Heralded by weak signals, hidden in natural [56] or artificially-induced [57] noise, they pose basic detection challenges. In contrast to repetitive waveforms, a single-instance signal cannot be separated from noise by averaging [56]. In addition to requiring a fast and sensitive detector, a randomly occurring signal must be extracted from the background noise in either the optical or electrical domain. Intuitively, if an event is repetitive, detection sensitivity can be significantly enhanced by averaging over time [56], or by utilizing stochastic resonance [58]. The gain in sensitivity originates from a fundamental difference between the noise and signal fields: the former is characterized by temporally uncorrelated statistics, while the latter is correlated in time domain. When the noise correlation time is much shorter than the event duration, an arbitrary SNR improvement can be realized by summation of a sufficiently large number of signal instances [56]. Simple to implement, averaging plays a critical role in the capture

of fast, weak or noisy signals. A powerful generalization of the averaging concept was developed for cyclostationary signals accompanied by spectrally uncorrelated noise, as described in section 2.2.

In contrast to temporal averaging, cyclostationary and cumulant analysis recognizes that noise spectral components can be rejected if the signal is cyclically modulated. Intuitively, a similar treatment could be extended to a single-instance signal if the Fourier transform coefficients can be calculated. As discussed in detail in Section 2.1 and Section 2.2, utilizing an ADC and a digital approach to measure the Fourier transform coefficients for a fast signal presents many significant detection challenges. One method to get around this is to produce the Fourier coefficients in the analog domain and measure them directly. To do this, the signal would first need to be replicated, and each of the replicated copies would be shifted in frequency and low pass filtered. The replication of a signal of interest presents the first set of challenges to an all analog Fourier transform approach. In earlier work [59], a recirculating loop was used to create multiple, serialized signal outputs that can be independently detected and subsequently averaged. Such replication requires an amplifier to overcome coupling losses, thus injecting excess (amplification) noise. Unfortunately, all known physical temporal replication mechanisms [59], [60] are inherently lossy and are subject to this basic limitation. Next, frequency shifting each of the replicated signals in the electrical domain is a challenge in itself, due to the loss and nonlinearity of electrical mixers, and the requirement of a bank of local oscillators. However, frequency shifting in the optical domain is a much simpler approach, as described in this dissertation. As a result, the exploitation of correlated signal frequency components and uncorrelated noise

components had not been realized for fast single instance signals prior to this work. To achieve this, a new temporal replication technique is introduced, and its application to the reception of single transient events is discussed in Chapter Chapter 5.

Chapter 3 Parametric Process

While nonlinear processes in optical fibers are typically detrimental to many types of systems, it will serve as a foundation for generating an optical frequency comb for this thesis. This chapter begins with Maxwell's equations and after some derivation, the origin of nonlinear processes will be apparent. The various types of parametric processes will then be discussed. Finally, the generation of wideband optical frequency combs will be discussed in detail.

3.1 Electromagnetic Theory

Beginning with Maxwell's equations [61] for non-magnetic materials with no free charge and neglecting any atomic variations of the field:

$$\nabla \boldsymbol{D} = 0 \tag{3.1}$$

$$\nabla \boldsymbol{B} = 0 \tag{3.2}$$

$$\nabla \times \boldsymbol{E} = -\frac{\partial \boldsymbol{B}}{\partial t} \tag{3.3}$$

$$\nabla \times \boldsymbol{B} = \mu_0 \frac{\partial \boldsymbol{D}}{\partial t} \tag{3.4}$$

where $\boldsymbol{E}$ and $\boldsymbol{B}$ are the electric field and magnetic flux density, respectively, and μ_0 is the vacuum permeability constant. The electric displacement is defined as:

$$\boldsymbol{D}(\boldsymbol{E}) = \varepsilon_0 \boldsymbol{E} + \boldsymbol{P} \tag{3.5}$$

where ε_0 is the vacuum permittivity constant and $\boldsymbol{P}(\boldsymbol{E})$ is the polarization describing the electric dipole moments induced in the medium. By taking the curl of Eq. (3.3), and substituting in Eq. (3.4) and Eq. (3.5):

$$\nabla \times \nabla \times \boldsymbol{E} = -\frac{1}{c^2}\frac{\partial^2 \boldsymbol{E}}{\partial t^2} - \frac{1}{\varepsilon_0 c^2}\frac{\partial^2 \boldsymbol{P}}{\partial t^2} \tag{3.6}$$

where $c = (\varepsilon_0\mu_0)^{-1/2}$ is the speed of light in a vacuum. Using the curl of a curl identity, and recognizing that ∇E is small for homogenous isotropic materials:

$$-\nabla^2 \boldsymbol{E} + \frac{1}{c^2}\frac{\partial^2 \boldsymbol{E}}{\partial t^2} = -\frac{1}{\varepsilon_0 c^2}\frac{\partial^2 \boldsymbol{P}}{\partial t^2} \tag{3.7}$$

Eq. (3.7) describes the wave equation for any homogenous isotropic dielectric material. It is clear from Eq. (3.7) that the evolution of an applied field is directly related to the material response.

3.1.1 Linear Regime

In order to understand Eq. (3.7) and its implication, it is more convenient to work in the Fourier domain. When the applied field strength in an optical fiber is much lower than the interatomic field strength, the polarization can be expressed in linear form in the Fourier domain:

$$\tilde{P}(z,\omega) = \epsilon_0 \chi^{(1)}(z,\omega)\tilde{E}(z,\omega) \tag{3.8}$$

Where z is the propagation direction, $\chi^{(1)}(z, \omega)$ is the first order susceptibility at position z and angular frequency ω, and $\check{E}(z,\omega)$ is the Fourier transform of $E(z,t)$. As a result, the Fourier domain representation for small applied field strength can be written:

$$\nabla^2 \tilde{E}(z,\omega) = -\epsilon_r(\omega)\frac{\omega^2}{c^2}\tilde{E}(z,\omega) \tag{3.9}$$

where $\epsilon_r(\omega)$ is the relatve dielectric constant:

$$\epsilon_r(\omega) = 1 + \chi^{(1)}(\omega) = (n(\omega) + j\alpha(\omega))^2 \tag{3.10}$$

and $n(\omega)$ is the refractive index, $\alpha(\omega)$ is the absorption coefficient associated with the medium, and $j = \sqrt{-1}$. The absorption coefficient is the main contribution of power loss in a medium, but is significantly low for silica fiber. However, $n(\omega)$ is the main contribution towards chromatic dispersion. Namely, the refractive index is frequency dependent, introducing a frequency dependent phase velocity equal to $v(\omega) = c/n(\omega)$. This frequency dependent phase velocity plays a critical role in nonlinear processes. To account for these effects, the mode propagation constant β is introduced, and conventionally is expanded by a Taylor series centered at a reference frequency ω_0:

$$\beta(\omega) = \frac{\omega}{c}n(\omega) = \sum_n \beta_n(\omega - \omega_0)^n/n! \tag{3.11}$$

where

$$\beta_n = \left(\frac{d^n\beta}{d\omega^n}\right)_{\omega=\omega_0} \quad (n = 0, 1, \dots) \tag{3.12}$$

and β is the mode propagation constant.

3.1.2 Nonlinear Regime

In many cases of optical fiber transmission, the optical intensity can be relatively high due to the high confinement of optical fibers coupled with the long

transmission length. Under these conditions, the applied field induces anharmonic motion of the bound electrons in the medium. Consequently, the polarization $\boldsymbol{P}$ can no longer be a linear function of the electric field $\boldsymbol{E}$. Assuming the applied field strength is significantly smaller than the interatomic field strength (a valid assumption for most optical powers used), but still strong enough to introduce a nonlinear response, the nonlinear response from the applied electric field can be approximated as a small perturbation to the state of polarization $\boldsymbol{P}$ and expanded into a power series [61]:

$$\boldsymbol{P} = \varepsilon_0\left(\chi^{(1)}\boldsymbol{E} + \chi^{(2)}\boldsymbol{EE} + \chi^{(3)}\boldsymbol{EEE} + \cdots\right) \tag{3.13}$$

where $\chi^{(n)}$ (n = 1, 2, …) is the n-th order susceptibility tensor of rank n + 1.

The most dominant contribution to $\boldsymbol{P}$ is $\chi^{(1)}$ which is prevalent even in the linear regime. The even order susceptibility tensors $\chi^{(2j)}$ (j = 1, 2, …) for materials such as silica theoretically vanish due to the symmetric atomic lattice structure of silica. However, due to defects along the core of a fiber during manufacturing, small $\chi^{(2)}$ responses can be observed in regular silica fiber. For the purposes of this thesis, these contributions are considered negligible. Therefore, the lowest order contributions to nonlinearities in silica fiber are from $\chi^{(3)}$. As a result, the polarization $\boldsymbol{P}$ can be approximated for silica fibers as

$$\boldsymbol{P} = \varepsilon_0\left(\chi^{(1)}\boldsymbol{E} + \chi^{(3)}\boldsymbol{EEE}\right) = \boldsymbol{P}_L + \boldsymbol{P}_{NL} \tag{3.14}$$

Where $\boldsymbol{P_L}$ and $\boldsymbol{P_{NL}}$ describe the linear and nonlinear contributions to polarization, respectively.

A. Nonlinear Phase Modulation

When the total field $E(z,t)$ possesses a spectral span small enough to neglect the frequency dependent material properties, the field can be partitioned as:

$$E(z,t) = F(x,y)A(z,t)e^{-j\omega t+j\beta z} + c.c. \tag{3.15}$$

where $F(x,y)$ is the modal distribution, (x,y) indicate the transverse coordinates, and $A(z,t)$ is the slowly varying temporal distribution. Under these assumptions, the temporal distribution will follow [62]:

$$\frac{\delta A}{\delta t} + jDA + \frac{\alpha}{2}A = j\gamma|A|^2A \tag{3.16}$$

$$D = \sum_n \frac{j^n}{n!}\beta_n \frac{\delta^n}{\delta t^n} \tag{3.17}$$

where γ is the nonlinear coefficient and defined as:

$$\gamma = \frac{n_2\omega}{cA_{eff}} \tag{3.18}$$

Here, n_2 is defined as the nonlinear refractive index, and A_{eff} is the effective core area:

$$n_2 = \frac{3}{8n}Re(\chi^{(3)}) \tag{3.19}$$

$$A_{eff} = \frac{\left(\int_{-\infty}^{\infty}\int_{-\infty}^{\infty}|F(x,y)|^2dx\,dy\right)^2}{\int_{-\infty}^{\infty}\int_{-\infty}^{\infty}|F(x,y)|^4dx\,dy} \tag{3.20}$$

From Eq. (3.16), conventionally coined the nonlinear Schrödinger equation, it is clear that the nonlinear interaction on the right sight of the equation is dictated by the parameter γ, and the intensity of the field $|A|^2$. As a result, the most efficient nonlinear processes occur in material with high confinement (minimizing A_{eff}) and high optical intensities. A common measure for the strength of the nonlinear process is the nonlinear

figure of merit (NFoM): γPL, where P is the optical power, and L is the total interaction length.

The nonlinear Schrödinger equation derived in Eq. (3.16) can be used to successfully describe many nonlinear effects, however, it may need to be adapted for some system implementations. For instance, the effects of stimulated inelastic scattering such as stimulated Raman scattering and stimulated Brillouin scattering (SBS) are not accounted for. In addition, some of the assumptions made in the derivation of Eq. (3.16) are not applicable in some cases. For instance, when the field consists of ultrashort (<100 fs) optical pulses, the spectral width becomes comparable to the carrier frequency, invalidating some of the assumptions made.

As an approximation, if dispersion and loss are both negligible ($D = \alpha = 0$), then Eq. (3.16) can be solved analytically:

$$A(z,t) = A(0,t)e^{j\gamma|A(0,t)|^2 z} \tag{3.21}$$

While this approximation is not always practical, it does provide some useful insight into the third order nonlinear process. In the absence of dispersion and loss, Eq. (3.21) indicates that the nonlinear effect manifests itself as a phase rotation on the envelop of the field. Intuitively, since no power is transferred or lost in this case, the power must remain the same at any point z and thus, only phase modulation can exist. This phase modulation occurs due to the high optical intensity modulating the nonlinear refractive index of the material, which in turn produces a phase shift to the optical field. This phase modulation is the core mechanism for the generation of parametric optical frequency combs when more than one optical frequency tone is propagating together.

B. Four Wave Mixing

When the total field $E(z,t)$ possesses a sum of four copolarized spectral components all travelling in the direction of z, a set of coupled equations can be derived based off the nonlinear Schrodinger equation [63], [64]:

$$\frac{\delta A_1}{\delta z} = -\alpha + jDA_1 + j\gamma\left(|A_1|^2 A_1 + 2\sum_{n=2}^{4}|A_n|^2 A_1 + 2A_2^* A_3 A_4 e^{j\Delta\theta}\right) \tag{3.22}$$

$$\frac{\delta A_2}{\delta z} = -\alpha A_2 + jDA_2 + j\gamma\left(|A_2|^2 A_2 + 2\sum_{n\neq 2, n=1}^{4}|A_n|^2 A_2 + 2A_1^* A_3 A_4 e^{-j\Delta\theta}\right) \tag{3.23}$$

$$\frac{\delta A_3}{\delta z} = -\alpha A_3 + jDA_3 + j\gamma\left(|A_3|^2 A_3 + 2\sum_{n\neq 3, n=1}^{4}|A_n|^2 A_3 + 2A_1 A_2 A_4^* e^{-j\Delta\theta}\right) \tag{3.24}$$

$$\frac{\delta A_4}{\delta z} = -\alpha A_4 + jDA_4 + j\gamma\left(|A_4|^2 A_4 + 2\sum_{n=1}^{3}|A_n|^2 A_4 + 2A_1 A_2 A_3^* e^{j\Delta\theta}\right) \tag{3.25}$$

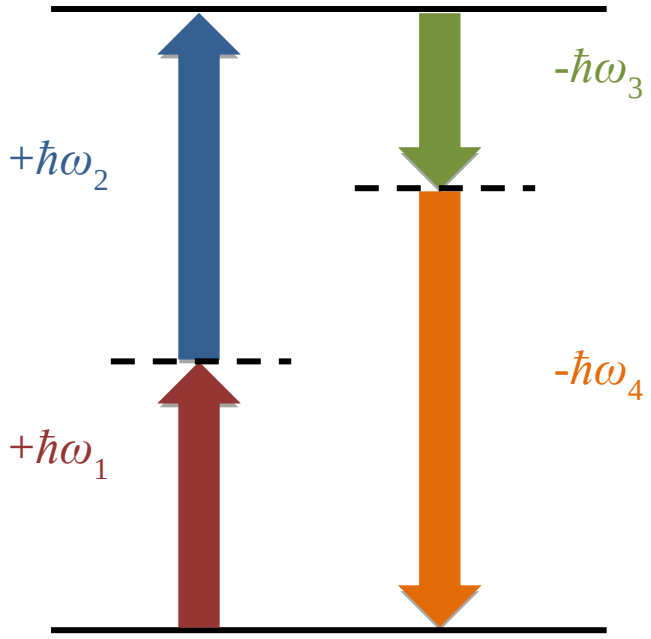

Figure 3.1 Energy level diagram for FWM process

where $\Delta\theta(z,t) = (\beta(\omega_1) + \beta(\omega_2) - \beta(\omega_3) - \beta(\omega_4))z + (\omega_4 + \omega_3 - \omega_2 - \omega_1)t$ describes the phase evolution of the two waves, assuming the phase of each of the input fields is aligned at $z = 0, t = 0$. The terms in Eq. (3.22) that are proportional to γA_1 are the result of self phase modulation (SPM) and cross phase modulation. The remaining term couples all input modes together and is the result of the four wave mixing (FWM) process. Under the correct conditions, the FWM process effectively couples power from two modes into two other modes, satisfying all energy conservation principles. From a quantum mechanical perspective, two modes each donate a photon, which annihilate together and generate two new photons satisfying the energy conservation principle, as shown in Figure 3.1. From a classical perspective, two strong modes propagate together at ω_2 and ω_3 and modulate the nonlinear refractive index at their frequency difference. This nonlinear refractive index modulation then phase modulates

the two modes propagating together, effectively generating sidebands at $\omega_1 = 2\omega_2 - \omega_3$ and $\omega_4 = 2\omega_3 - \omega_2$.

The efficiency of the FWM process is not only dictated by the material properties, optical field power, and interaction length, but also to the phase matching term $\Delta\theta(z,t)$. It's clear that the power evolution of a single mode will grow monotonically from FWM if the term $e^{j\Delta\theta}$ does not change sign during propagation. This indicates that the efficiency of the FWM process can be manipulated by altering the dispersion profile of the medium. For this dissertation, a wideband FWM process is desired, indicating the need for a unique dispersion profile to satisfy the phase matching condition. To achieve this, highly nonlinear fiber (HNLF) is used, which consists of small core diameter silica fiber doped with germanium, helping to increase the confinement area and refractive index [61].

3.2 Optical Frequency Comb Generation

One unique application of FWM is in the generation of optical frequency combs, one of the core components to this thesis. While FWM is certainly not the only way to generate an optical frequency comb, it is indeed the best method to satisfy all the needs for this thesis. Specifically, a frequency comb should have a large number of carriers (>250), large frequency separation (>10 GHz), high optical signal to noise ratio (OSNR>40dB) and freely tunable pitch and center frequency. Early combs based off of feedback mechanisms including mode-locked lasers [65], [66] and micro-cavities [67], [68] do not possess frequency configurability. Another drawback to these cavity-based combs is the low OSNR, typically much lower than standard telecom grade lasers (i.e.,

>40 dB). Another class of combs can be derived out of modulators [69], [70], allowing for frequency agile comb generation. However, these class of generators are limited in spectral span, at best, to only a few tens of spectral lines. Recognizing these limitations, a new class of optical frequency combs was recently developed to possess a large number of spectral lines, high OSNR, and frequency configurability [71], [72].

The optical frequency comb is generated based off the FWM effect in HNLF. To achieve efficient FWM, the field should consist of multiple equidistant frequency tones in a high confinement fiber, and possess a high power over a long length of medium, as described in section 3.1.2. The high confinement and high power maintained over a long distance is achieved with HNLF, possessing low loss. While many different mediums possess much higher confinements than HNLF, their intrinsic loss limits the total FWM effect. Finally, the multiple frequency tones and high peak

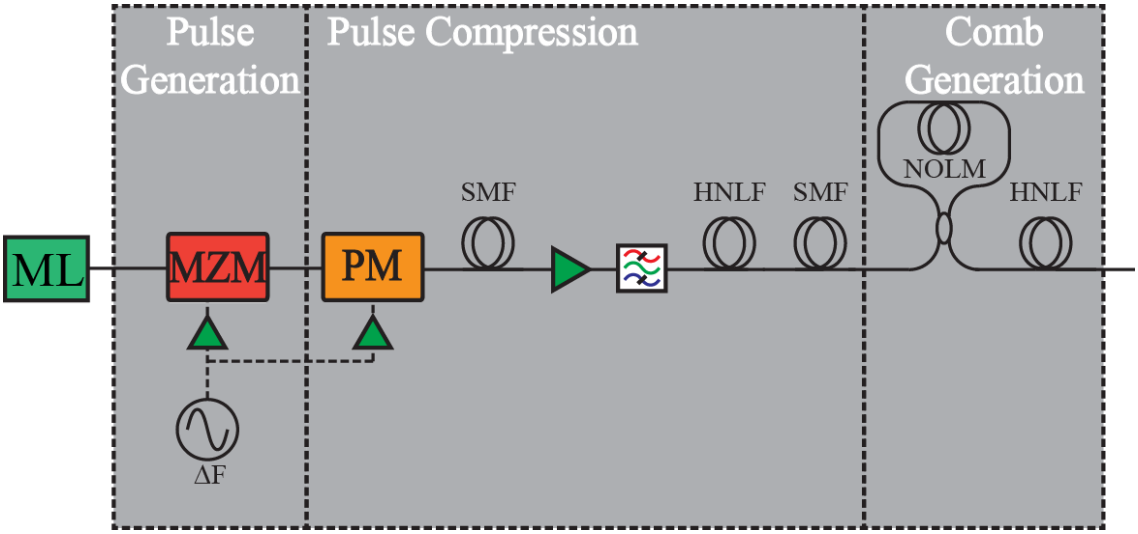

Figure 3.2 Overview of tunable optical frequency comb generation. ML: Master Laser, MZM: Mach-Zehnder modulator, PM: Phase modulator, SMF: Single mode fiber, HNLF: Highly nonlinear fiber, NOLM: Nonlinear optical loop mirror.

power are achieved with pulse modulation, with amplification and subsequent compression.

An overview of the tunable optical frequency comb generation process is shown in Figure 3.2. First, a high quality master laser (ML) is used to seed the comb. Next, broad (>10 ps) optical pulses are carved using an MZM driven with an electrical sinusoid at ΔF, which will set the pitch of the generated comb. To increase the peak power of the generated pulses, the pulses undergo a single compression stage, amplification, and a second compression stage. The first compression stage consists of pulse chirping and a dispersive element. Pulse chirping is achieved using a phase modulator (PM) driven with the same electrical signal as the MZM at ΔF. A tunable electrical delay is placed before the PM to optimize the induced chirp.

The field after the phase modulator can be approximated as [73]:

$$A(t) = A(0)\sum_{n} J_n(\Delta\phi)e^{j(\omega-2\pi n\Delta F)t} \tag{3.26}$$

where J_n is the n-th order Bessel function (n an integer), and ω is the optical frequency. The instantaneous frequency can then be derived as:

$$\nu(t) = \frac{\omega}{2\pi} - \Delta\phi\Delta F\cos(2\pi\Delta F t) \tag{3.27}$$

The intensity and instantaneous frequency profile of the field after the MZM and PM are shown in Figure 3.3. Near the peak of the intensity function in Figure 3.3, the instantaneous frequency profile can be estimated as a linear function. As a result, effective pulse compression can then be achieved down to <10 ps by propagating through a dispersive medium (such as SMF) that aligns each of these frequency

components at a single time instance. Interestingly, this method for pulse compression can be done with either an anomalous ($\beta_2 < 0$) or normal ($\beta_2 > 0$) dispersive medium simply by tuning the electrical delay before phase modulation to achieve either an up-chirp or down-chirp on the pulses, respectively. Unfortunately, the estimation of

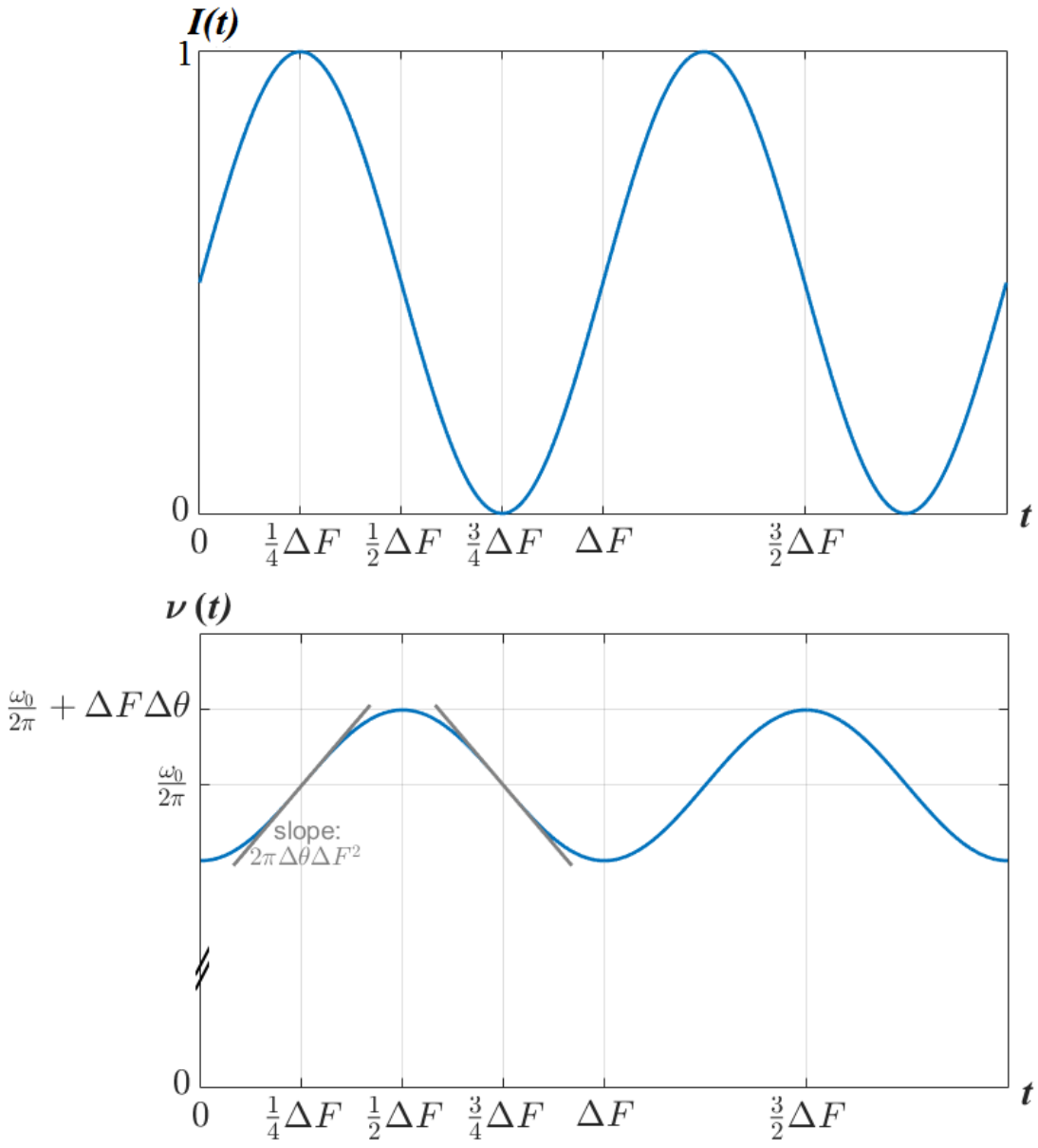

Figure 3.3 Plot of the optical intensity, $I(t)$, and optical instantaneous frequency, $\nu(t)$, after sinusoidal amplitude and phase modulation

instantaneous frequency as a linear function is not true away from the center of the intensity function in Figure 3.3. At time instances near the peak of the intensity profile, the chirp induced is quadratic and at even lower intensity levels the chirp has many higher order tones. Subsequently, parasitic pedestals will be generated if only a linear dispersive element is used. The effects and mitigation of these pedestals will be discussed later in the comb generation process.

Next, the peak power of the generated pulses is increased by transmitting through an erbium and ytterbium doped fiber amplifier (E-YDFA), boosting the average power to ~2 W. With sufficiently narrow high power pulses, a second compression stage can be implemented to compress the pulses even further. First, a positive Kerr-induced chirp is applied to the pulses in a length of HNLF. Next, a second dispersive stage possessing negative second order dispersion ($\beta_2 < 0$) is used to compress the pulses to <500 fs.

Possessing short duration pulses (<500 fs) and high peak power (>100 W), a highly efficient FWM process can be achieved if transmitted through HNLF. However, if this were done, the parasitic side lobes from the compression stages would manifest as power fluctuations in the envelop spectrum of the generated comb [72]. To combat this, the side lobes can be suppressed by a pulse shaping element. Since the pedestals will have sufficiently lower power than the main pulses, a device with a correct power dependent transfer function can be used to mitigate these pedestals. For the combs generated in this dissertation, a nonlinear optical loop mirror (NOLM) is used to achieve a power dependent transfer function sufficient to suppress the time domain pedestals by ~ 15 dB [72].

For generation of a wideband comb, phase matching ($\Delta\theta(z,t) = 0$) over a wide bandwidth is necessary. If dispersion and loss can be neglected, the width of the total comb generated will be limited only by how much power can be pumped into the fiber. Ultimately, the total power will be limited by SBS in fiber, which can be minimized using optical frequency dithering [74] or longitudinal fiber tensioning [75]. Practically, after SBS is suppressed, dispersion cannot be neglected and will be the main limiting factor for the total width of the comb, as terms far away from the zero dispersion wavelength of the fiber will experience a phase shift yielding a mismatched phase condition. Thus, to generate ultra-wideband combs, the dispersion of the fiber used needs to follow a strict set of parameters. Rather than imposing unrealistic targets on fiber manufacturing, the errors in manufacturing can be mitigated by applying longitudinal fiber tensioning to obtain a desired dispersion profile [76].

With dispersion engineered fiber by longitudinal tensioning, the high peak power, pedestal free pulses can be sent to the final stage of HNLF (>100m). The long interaction length coupled with the high peak power and phase matching condition satisfied over a large bandwidth yields an efficient FWM process where multiple new replica tones are generated. Thus, a wideband optical frequency comb with a high count of carriers is spawned, paving the way for high efficiency spectral processing.

Chapter 4 Comb Assisted Coded Signal Receiver

As discussed in Chapters 1 and 2, the ability to capture and simultaneously process broadband sources pose multiple physical and practical limitations. While much work has been focused on developing faster capturing devices, such as photonic ADCs, they each are still limited in their performance in high speed capturing and also rely on fast electronic processors for processing the captured data. Recognizing these limitations, a new receiver architecture is designed and constructed to simultaneously capture and process a wideband signal.

The new receiver design is introduced first in this chapter. The dual OFC receiver is demonstrated to capture two different types of wideband coded signals. The discussion begins with the reception of a DSSS data sequence by use of a computation free discrete Fourier transform (DFT) engine. Two different configurations of the receiver are presented in Section 4.1 and 4.2, respectively, with each section going into detail of the principle of the receiver, the experimental demonstration and concluding remarks. Finally, in Section 4.3, the dual OFC receiver is demonstrated to receive a FH-PPM signal, with a detailed discussion of the principle of the receiver, the experimental demonstration and concluding remarks.

4.1 Comb Enabled Spread Spectrum Demodulation and Synchronization

Recognizing that regulation free secure communication could be achieved if a broadband signal could be simultaneously captured with high precision and processed with low complexity, as discussed in Section 2.1, a new receiver design is introduced to achieve this. The new receiver design is introduced in this chapter and is demonstrated

to achieve quick synchronization and subsequent demodulation of a DSSS sequence with little computation. In addition, the new receiver design is demonstrated to predict the timing delay of an emulated multi-path interference (MPI) environment. Section 4.1.1 discusses the principle of operation of the proposed receiver. Section 4.1.2 describes the recipe to generate a near optimum channel selection function. Section 4.1.3 is dedicated to the experimental setup to test the newly developed receiver. Finally, concluding remarks and results are presented in section 4.1.4.

4.1.1 Principle of Operation

When a channel experiences negligible MPI, the encoded bit $b[n]$ can be recovered by correlating the quantized received signal $x[n]$ and the codeword [25], [27] $c[n]$. In the Fourier domain, correlation is mapped to a single multiplication:

$$b[n] = \sum_{m=-N/2}^{N/2} c[m]x[m+n] \xrightarrow{\mathcal{F}} \tilde{C}^{*}[k]\,\tilde{X}[k] \tag{4.1}$$

Where $\tilde{C}[k]$ and $\tilde{X}[k]$ are the DFT of the codeword and the received signal. In the temporal domain, when the delay between the received signal and codeword is not known, discrete summation in Eq. 4.1 must be performed repeatedly to recover data. However, this approach mandates for the DFT of the received signal to be computed in real time, posing a progressively larger challenge as the spreading rate increases [30], [31].

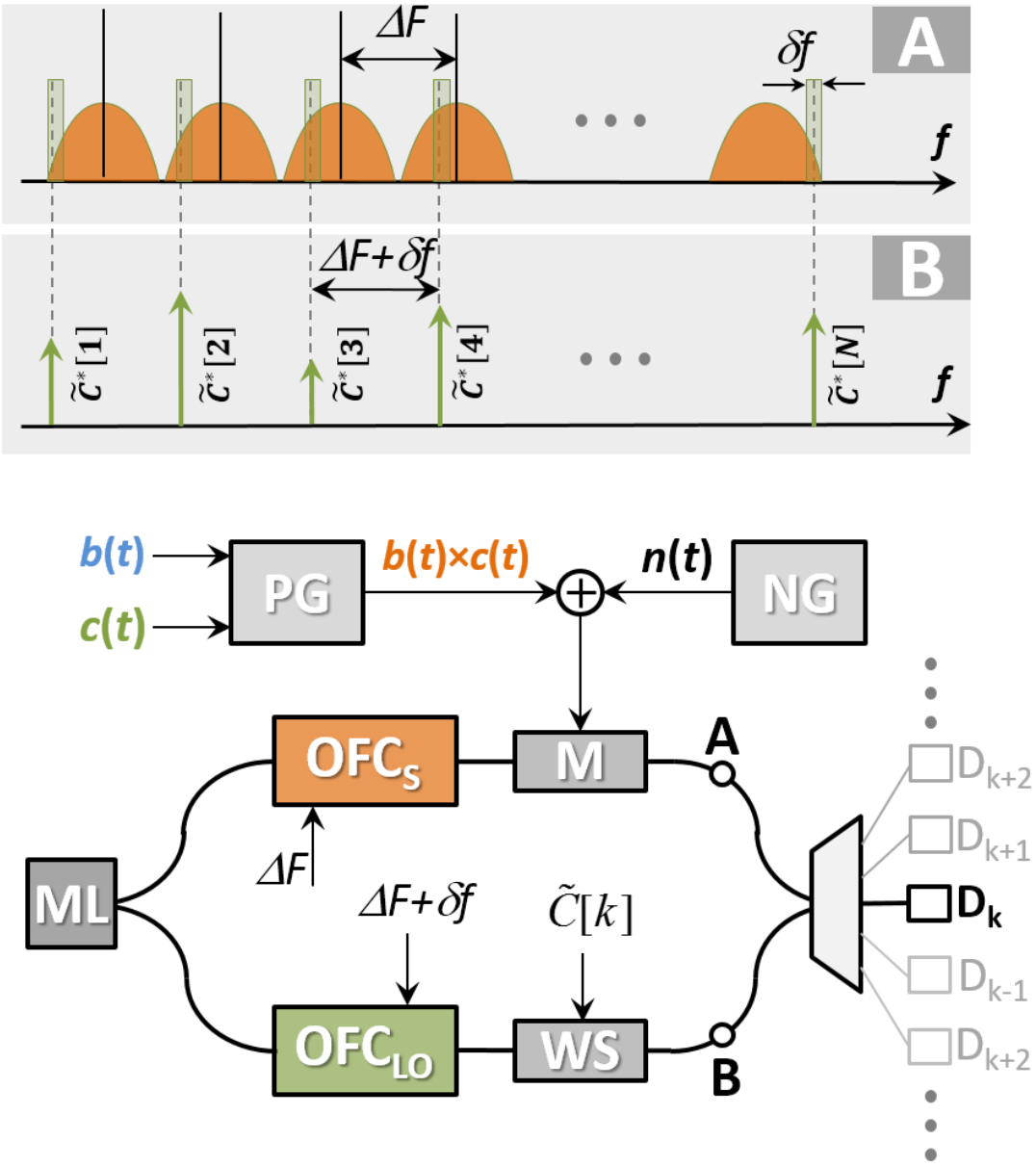

Figure 4.1 Comb-Assisted Spread Spectrum Receiver (CASSPER). Signal frequency comb (OFC_S) is modulated (M) to replicate the received signal to N comb modes. The local oscillator comb (OFC_{LO}) is modulated by the wave-shaper (WS), imprinting terms of the codeword DFT onto each comb mode (inset LO). In synchronized state, two combs are multiplied and integrated by a single sub-rate detector (D_k), decoding the spread-spectrum channel.

Recognizing this challenge, the new receiver, shown in Figure 4.1, performs

Fourier decomposition and code matching in the physical domain, eliminating the need for high-rate digitization and subsequent electronic processing. To understand its operating principle, consider the reception of a signal with bandwidth δf that was spectrally spread to $\Delta f = N \times \delta f$ width using a coding sequence of length N. The received spread-spectrum signal modulates N modes of the optical frequency comb (OFC_S), spectrally replicating the received field. The second, mutually coherent local oscillator (LO) comb (OFC_{LO}), is subsequently combined with signal replicas and detected by the detector array D. The difference in frequency pitch between the two combs $\delta f = \Delta F_{LO} - \Delta F_S = \Delta f / N$ is specifically chosen to guarantee that each OFC_{LO} mode overlaps with a different segment of the received spectrum, as shown in Figure 4.1. If each comb pair is sent to a sub-rate receiver (D_k) that matches the native signal bandwidth (δf), then the resulting array output is a discrete Fourier decomposition of the received field $\tilde{X}[k]$, $k = 1, \dots, N$. However, if OFC_{LO} modes are encoded by the spreading sequence $\tilde{C}[k]$, the output corresponds to the bit-decoding operation in Eq. 4.1. In a synchronized state, the receiver array is redundant and a single, sub-rate receiver is sufficient to decode the original bit-stream. As a consequence, the new receiver architecture completely eliminates the need for high-rate digitization and correlative processing at full-spreading rate (Δf).

To validate the comb-assisted decoding principle, it is not sufficient to operate the receiver in synchronous state, with a precisely aligned codeword and received channel. Instead, the experiment is conducted in asynchronous state, with unknown delay between the two. In conventional spread-spectrum receivers, the synchronization process greatly depends on the code length [27]. If the sequence is short, an unknown

delay can be found by imposing repeated multiplication and a chip-scale temporal shift. Unfortunately, this approach calls for up to N^2 multiplications and induces excessive delay as the code length (N) increases. To counter this, receivers are often parallelized [25], nesting coarse and fine delay searches. In contrast, if the DFT of the received signal does not need to be computed, a qualitatively different synchronization approach can be devised. In the Fourier domain, decoding corresponds to vector multiplication between the signal and the conjugate of the codeword. In synchronized state, this operation maps complex terms of signal DFT expansion onto the real axis, allowing for simple summation, as shown in Figure 4.2a.

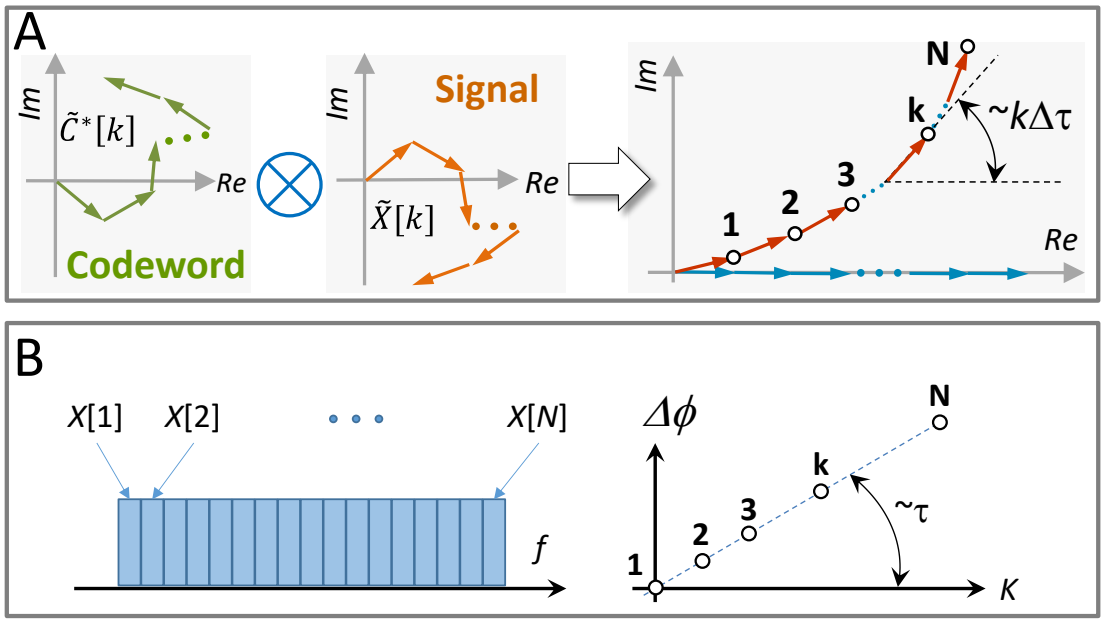

Figure 4.2 Receiver Synchronization. (A) Synchronous (blue) and asynchronous (red) decoding representation in Fourier domain. (B) Received signal DFT (X[k]) multiplication with the codeword (C*[k]) results in cross correlation function in frequency domain ($X[K] \times C^*[K]$) that has a linear phase ($\delta\phi$) proportional to signal-code delay (τ).

However, when signal $x(t)$ experiences unknown delay τ, its Fourier transform $\tilde{X}(f)$ sees frequency-dependent rotation $2\pi f\tau$, in complex plane: $\tilde{X}(f)e^{-j2\pi f\tau}$. This means that the k^{th} term of the signal DFT expansion will be rotated by $2\pi k\delta f\tau$ creating

a unique curvature, as shown in Figure 4.2A. Consequently, if the full complement (N) of sub-rate detectors is available, the synchronization problem can be reduced to an N-point curve interpolation in the complex plane. For a full backplane, when the receiver comprises a fully populated sub-rate detector array ($D_k, k = 1, \dots, N$ in Figure 4.1), the delay can be found by interpolating the N-point sequence, mapped to a delay-line in the $\Delta\phi$-k plane, as shown in Figure 4.2B. While superior in terms of latency (synchronization can be achieved during a single bit delay), this approach poses a fundamental challenge when the coding word is long and a very large backplane needs to be constructed. Indeed, the size of the detector array is strictly defined by the coding gain of the receiver. As an illustration, a comb-assisted receiver with 40dB-gain, operating with ~10GHz spreading range would guarantee a substantially interference-free, sub-noise transmission of MHz-rate channel. However, a direct implementation shown in Figure 4.1 would also require 10,000 detector elements in its backplane. While possible in principle, it is clear that an alternative must be examined: it is important to quantify the performance of the receiver when only a subset of M (M<N) sub-rate detectors is available to perform the Fourier-domain synchronization function.

In contrast to a fully populated receiver backplane, a significantly more difficult problem is posed by the need to synchronize the received signal with the codeword using a sparsely populated sub-rate detector plane, particularly in case when the signal is noisy. In absence of noise, only a few terms of the signal DFT expansion are sufficient to accurately interpolate the delay curve. With increased noise, DFT terms drift randomly, reducing the confidence with which the delay curve can be fitted. Consequently, the synchronization challenge in a comb-assisted receiver can be

articulated in simple terms: given the received SNR, what is the minimum number of sub-rate detectors necessary to achieve synchronization? Is it possible to synchronize the signal and the codeword in a short time interval, preferably during the first incoming bits of data? Remarkably, the answer to these questions greatly depends on the selection of the specific detector elements from the fully populated array, and not only on their total count. This is discussed in detail in the next section.

Once the channel selection function is chosen, the linear phase is estimated and the time of arrival prediction is estimated. To estimate this linear phase slope, the maximum likelihood condition for estimation [77] is used:

$$\tau = \max_{\tau_i} \left| \sum_{k=1}^{N} \tilde{X}[k] \tilde{C}^*[k] e^{-j2\pi k \delta f \tau_i} cs[k] \right| \tag{4.2}$$

where $\tau_i = i/(N\delta f),\ i = -\frac{N}{2}, -\frac{N}{2}+1, \ldots, \frac{N}{2}+1$ and $cs[k]$ is a channel selection function that selects a partial subset of the receivers as described in the next section.

4.1.2 Channel Selection Function

To understand the role of the selection, it is instructive to consider the frequency- and temporal-domain implication of a specific subset array selection. A qualitative argument can be provided by comparing the selection of a subset of adjacent receivers or selecting a periodic detector subset against selecting a sparse detector subset. In the first case, when $M << N$, the temporal resolution approaches that of a single sub-rate detector and is insufficient for accurate synchronization between the code and the signal. In the second case, when a sparse periodic subset of detectors is chosen, as shown in Figure 4.3, a high temporal resolution will be achieved but many

ambiguities due to phase unwrapping errors will remain. This effect can also be understood in terms of aliasing due to the uniform down-sampling [78].

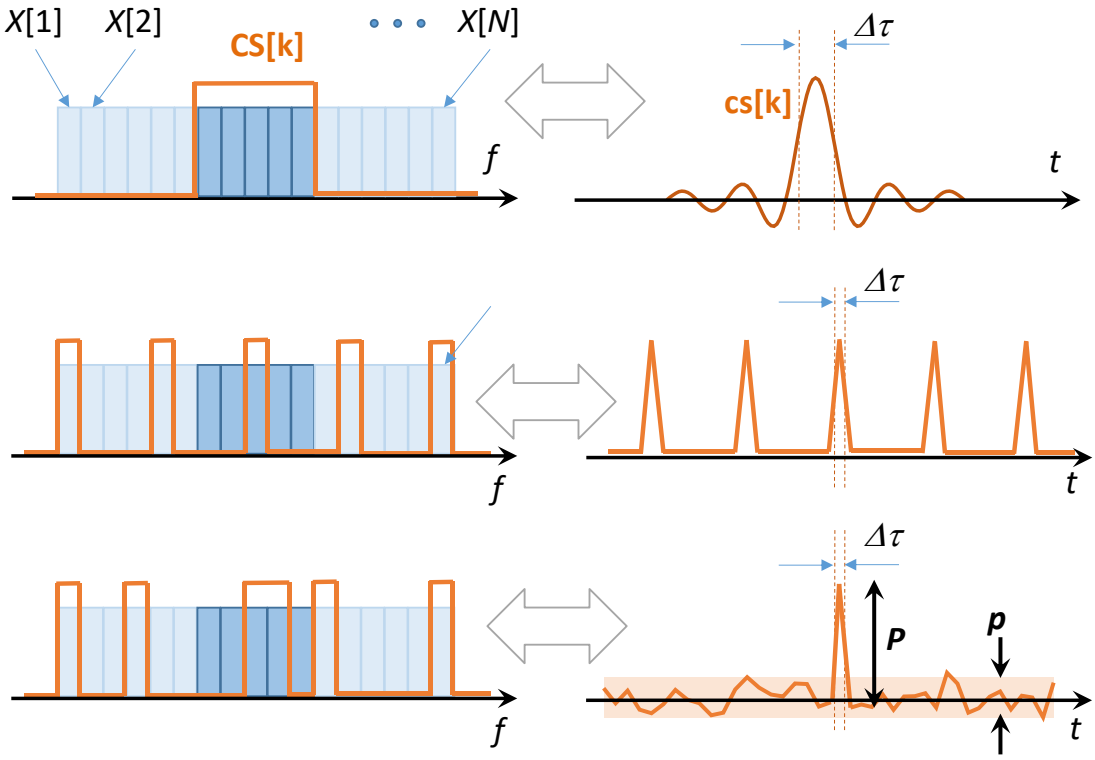

Figure 4.3 Synchronization Selection Function. (Top) A channel selection function (CS[k]) based on $M<N$ frequency bins that are either adjacent or periodic, results in insufficient resolution or ambiguity. Selection of aperiodic frequency bin set by a unique selection function CS[k] results in high-contrast function with high temporal resolution. $\Delta\tau$ – chip duration.

Consequently, the channel selection function that chooses either adjacent or strictly periodic frequency bins (i.e. detector elements) is sub-optimal and must be replaced by a unique set, under the constraint that the number of sub-rate detectors (M) remains constant. An intuitive selection criterion can be constructed in the temporal domain by requiring that the ratio between the peak (P) of the channel selection function CS[n] and any of its side lobes (p) remains as high as possible, as illustrated in Figure 4.3. However, to select a subset of M detectors from N-detector array, one must

evaluate N!/M!/(N-M)! possibilities. In the case of the proposed experiment (N=300), a selection of a 25 detector subset must be made out of a total of 1.95×10^{36} possibilities.

While sparsity plays a major role in the channel selection function, it is certainly not the only parameter to consider. Practically, in high noise environments, the SNR of each coefficient needs also to be considered. Specifically, the low SNR received coefficients with unknown time of arrival are multiplied by the conjugate of the known code word coefficients:

$$\widetilde{D}[k] = \left(\tilde{C}[k]e^{j2\pi\delta f\tau} + n[k]\right)\tilde{C}^{*}[k] \tag{4.3}$$

where τ is the unknown time of arrival and $n[k]$ is the interfering noise in the Fourier domain. For simplicity, Eq. (4.3) assumes that the modulated bit is in the one state and the total time interval is one bit in length. Then, the SNR of each coefficient will be:

$$SNR[k] = \frac{\left|\tilde{C}[k]\right|^{4}}{|n'[k]|^{2}} \tag{4.4}$$

where $n'[k]$ is the interfering noise field multiplied by the conjugate of the known code word coefficients. Thus, the SNR at each coefficient depends solely on the code word itself. As a result, the accuracy of the phase slope prediction can be maximized by choosing the highest SNR coefficients, ensuring the highest possible accuracy of the measured phase.

Ideally, the absolute optimal channel selection function will depend both on the sparsity of the selection as well as the SNR. For any given noise power and code word, a balance between sparsity and SNR maximization can be achieved. However, for very low SNR conditions, choosing the maximum SNR coefficients is likely sufficient to

achieve near optimal performance, and avoids having to search through such a colossally large number of possible subset combinations.

4.1.3 Experimental Demonstration

To experimentally prove and validate the proposed architecture, a comb-assisted spread-spectrum receiver was constructed by deriving two mutually coherent but frequency-tunable combs from a single master laser [72], [79]. The signal comb (OFC_S) with more than 300 highly coherent optical frequency tones separated by tunable pitch, with over 43 dB OSNR at 0.1 nm is plotted in Figure 4.4. The signal comb had frequency pitch of ΔF_S = 24.99 GHz, while the LO comb pitch was ΔF_{LO} = 25.01 GHz to accommodate 20 MHz signal bandwidth. The optical modulator was used to replicate the combined spread-spectrum and noise input onto N = 300 comb tones, allowing for 300-fold spectral spreading. The local oscillator comb was modulated by a static pattern using an optical waveshaper, as the conjugation of the local oscillator field is achieved in the coherent detector.

The data channel was spectrally spread in the digital domain, using a 13 GHz-wide pulse pattern generator (PG) to synthesize a 6 GHz-wide coding sequence. The minimum transition time that could be created in this manner was 20 ps. The DSSS signal is created by DSP, prior to its mapping into the optical domain. The 20 MHz binary phase shift keyed (BPSK) channel data content (payload) was generated by a 2^{10} long pseudo random bit sequence (PRBS). This bit pattern was then multiplied by a 300-chip long codeword, spreading the 20 MHz signal to 6 GHz width (chip duration

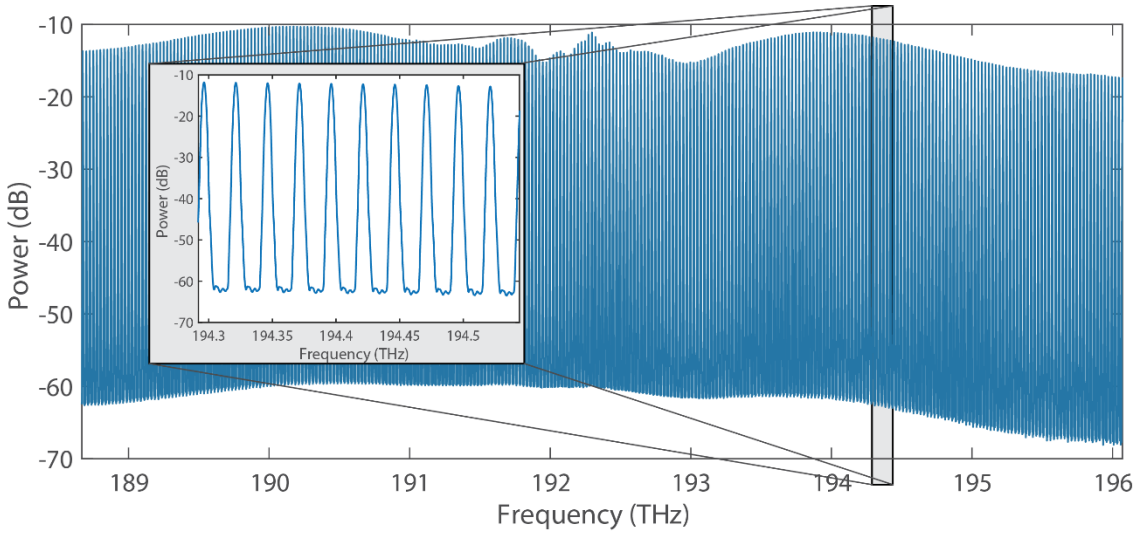

Figure 4.4 Optical frequency combs were generated by a single master in shock-wave parametric mixer, resulting in more than 300 coherent carriers possessing signal-to-noise-ratio (SNR) in excess of 43dB (inset). Resolution bandwidth set to 0.02 nm.

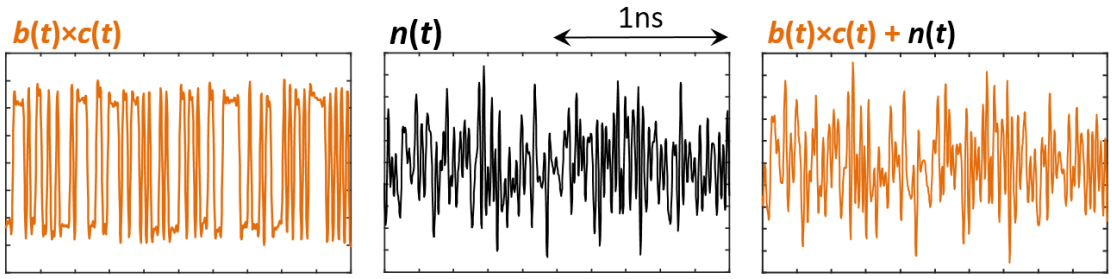

Figure 4.5 Experimental setup combines spread-spectrum channel (bxc) and noise (n) to modulate OFCs at varied SNR level. Generated waveforms correspond to 6GHz-wide spread-spectrum signal at SNR=-10dB. b-bit pattern; c-codeword.

Δt = 167ps). The codeword was synthesized by selecting the first 300 symbols of a 2^9 long PRBS. The resultant waveform was then uploaded to the PG and subsequently electrically filtered to limit the output bandwidth to 7 GHz. Separately, a 6 GHz wide, 170.6 μs long white-Gaussian-noise (WGN) waveform was generated using a 10GS/s, 10-bit resolution digital to analog converter (DAC). A plot of the generated signal and noise is shown in Figure 4.5.

Digital noise generation, while requiring a high-speed DAC, was specifically selected over a simpler, conventional (analog) noise source in order to allow for repeated backplane measurements under identical noise loading conditions. This allows for a complete and calibrated measurement of the receiver without physically assembling a full 300-detector sub-rate array. An arbitrary detector element response and its contribution to the array output can be measured by repeating the digital noise stimulus at the input. Conversely, this would not be possible if an analog (thermal) noise source was used, since the identical noise loading condition cannot be replicated in this manner. The synchronization between the noise-generating DAC and the data pattern generator was controlled to guarantee that the sequential capture of sub-rate detector outputs (corresponding to DFT coefficients) was performed under a precise noise-loading condition. This also required that both optical combs remain stable during the entire capture process. The latter was achieved by deriving both combs from a single, 8-kHz linewidth master laser. The output of the pattern generator was attenuated to vary the received signal power and combined with calibrated noise power to create a given SNR level at the receiver input. The combined signal and noise were imprinted onto modes of the signal comb using a bias-controlled Mach-Zehnder modulator (MZM).

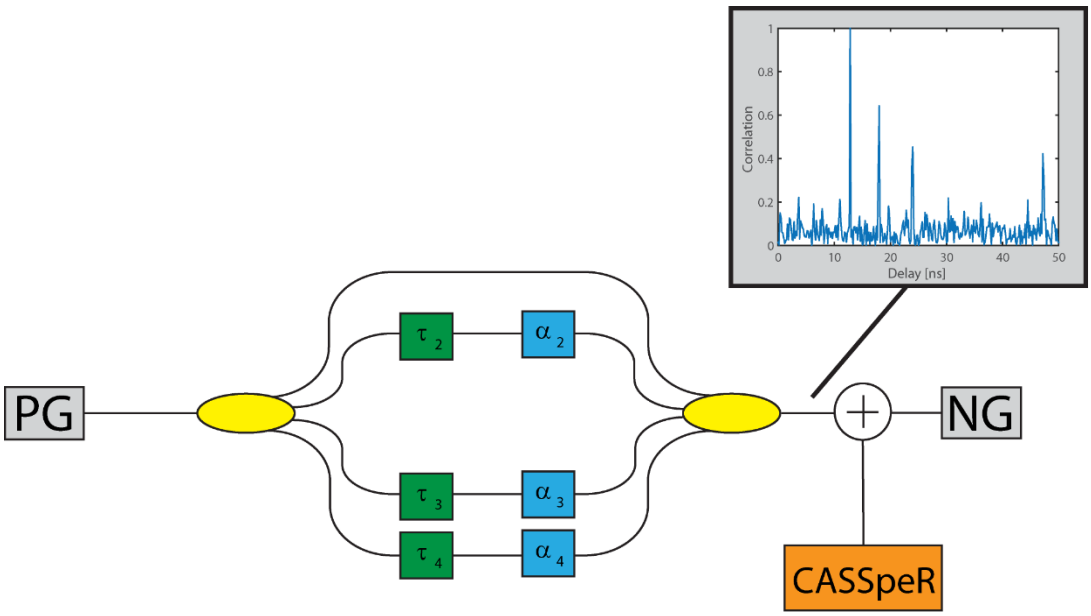

Figure 4.6 Multi-Path Generation Schematic used for emulating a Multi-Path Environment. PG: Pulse generator, τ: Delay, a: Attenuator, NG: Noise Generation, CASSpeR: Comb-Assisted Spread Spectrum Receiver (see Figure 4.1). Inset figure shows correlation with generated sequence.

To demonstrate the capabilities of the proposed scheme, MPI was emulated. As shown in Figure 4.6, to generate MPI, the 6 GHz DSSS electrical signal out of the PG was first amplified and then split into four RF paths with a coupler. Subsequently, a delay and attenuation value was assigned to each RF path. The four paths with varying delay were then recombined in a second coupler. The MPI signal was then combined with electrical Gaussian noise in an RF coupler to simulate a low SNR received signal. The MPI signal was generated with delays of 12.8, 18, 24, and 47.2 ns, each with varying SNR, as seen in the correlation plot in Figure 4.6. The SNR of each path was measured by terminating the other 3 paths and comparing the signal and noise SPD.

4.1.4 Discussion

To demonstrate the performance of the new receiver in predicting the timing offset, a 1024-bit packet was generated and used to acquire synchronization using 25 sub-rate detectors. Bits were generated at 20 MHz rate and spread to 6 GHz rate using a 300 length PRBS. As shown in Figure 4.7, SNR conditions were varied by changing the signal and noise power ratio. The electrically generated signal and noise were then modulated onto the signal comb (i.e., OFC_S) consisting of 300 spectral tones effectively replicating the signal. To synthesize the response of a fully populated detector array (i.e. 300 of 20 MHz bandwidth detectors), a tunable optical filter was used to select each channel from the signal and LO combs individually and route to a single coherent detector. Each of the 300 channels was digitized using an ADC and recorded. While it was not necessary to perform the measurement of all 300 tributaries to characterize the 25-subset, the full complement of experimental capture has allowed to test the hypothesis of the selection function uniqueness. Rather than performing a blind search over 1.95×10^{36} different subset combinations, a subset of 10^{10} combinations were examined, and a unique selection function was chosen shown in Figure 4.7. It should be noted that the selection function shown in Figure 4.7 corresponds to a sparse, aperiodic 25-long sequence. The selection function performance is characterized by a contrast of P/p ~ 15. Consequently, an optimal detector subset, shown in Figure 4.7, was used to measure synchronization performance.

At high SNR, a single bit was sufficient to interpolate a 25-point DFT constellation in complex plane and achieve 100% timing accuracy, as shown in Figure 4.8. However, when the noise power is an order of magnitude higher than the signal (SNR=-10dB), full timing accuracy required observation over 18 bits. It should be emphasized that, while the selection function is referred to as being optimal in this

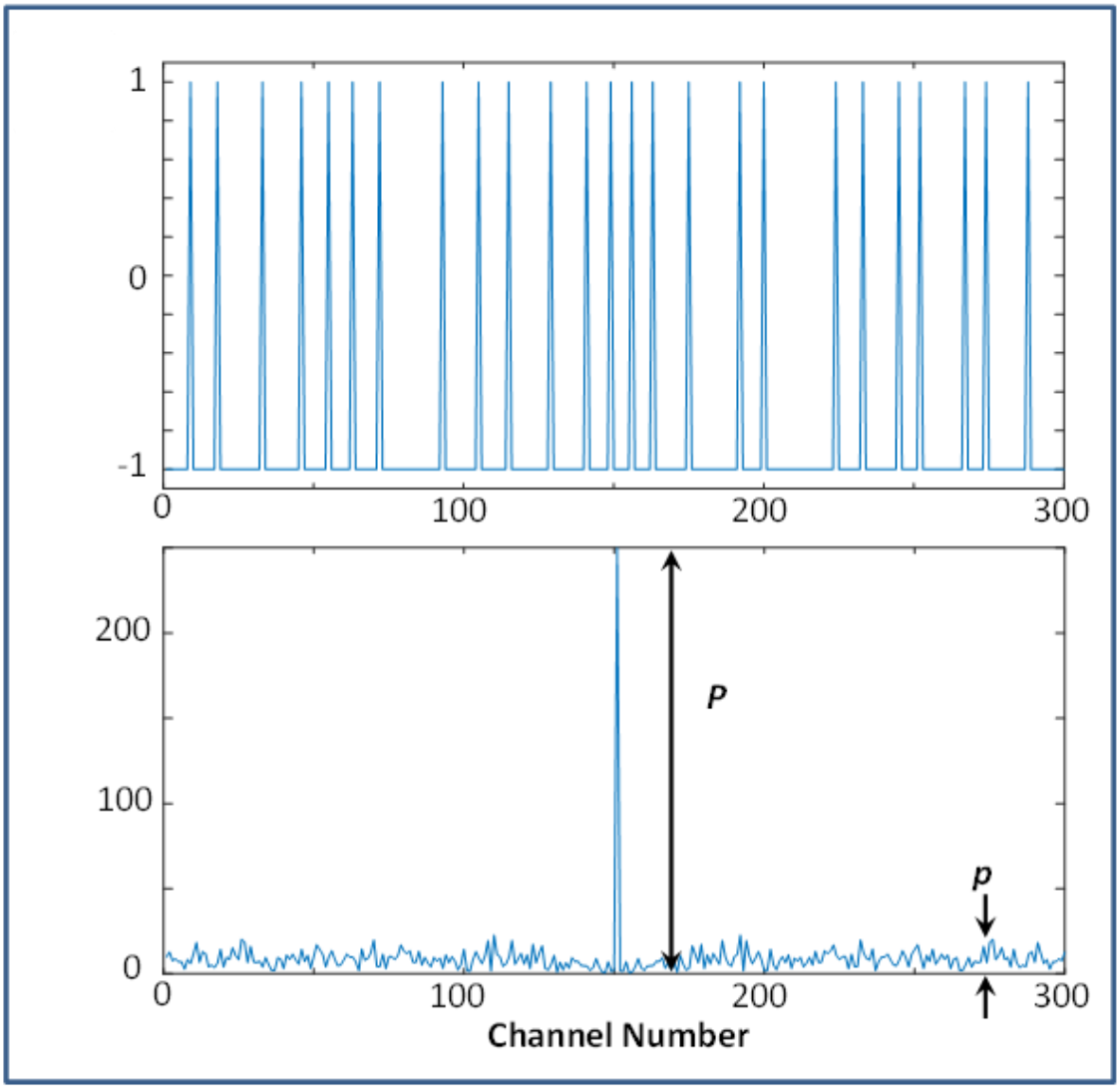

Figure 4.7 Optimal selection function for 25-sub-rate detector frequency bins selected from 300-bin backplane; Selection function correlation has decoding contrast of $P/p \sim 15$.

dissertation, this is not correct in a strict sense. Indeed, the selection function is the result of a search that covers only a fraction of the entire array combination space; it is highly likely that a more optimal selection (with superior synchronization properties) does exist. Consequently, a significant challenge that remains in comb-assisted receiver construction is further progress on optimal detector selection.

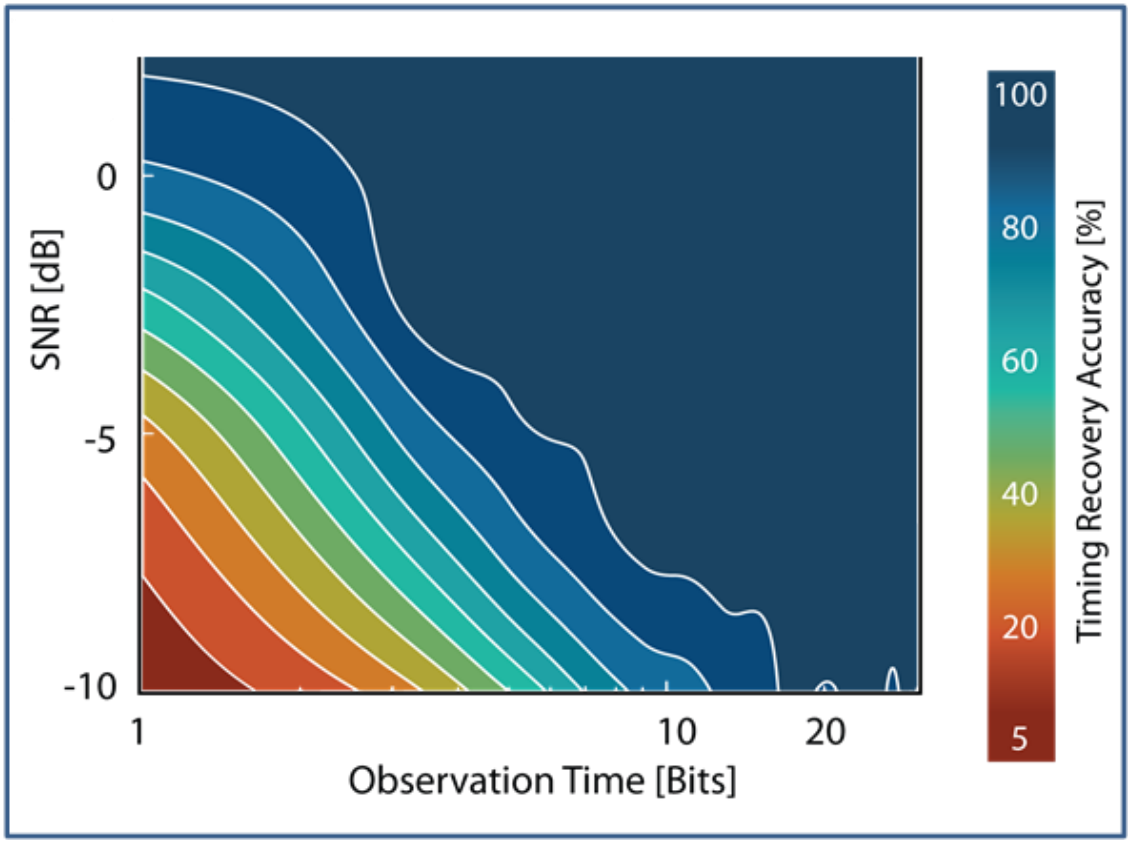

Figure 4.8 Measured synchronization performance of 6 GHz-wide spread-spectrum channel generated by 300-long code and native 20 Mb/s data and optimal sparse backplane (25-detector subset). Timing accuracy represents the number of correctly decoded bits from the received 2^{10}-bit long data stream.

The ability to operate in asynchronous mode permits the ability to rigorously measure the coding gain, being the most important performance metrics of the new receiver. Consequently, a channel carrying a 1024-bit packet was spectrally spread and

used to decode data using a single sub-rate detector. Signal-modulated OFC_S and codeword-modulated OFC_{LO} were combined in a single coherent detector. The LO comb downconverts and demodulates all 300 signal optical carrier frequencies to baseband, where 20 MHz band-limited coherent summation is achieved, resulting in computation-free decoding. The output is captured by an ADC to extract the bits and measure the coding gain. As an illustration, with an input SNR of 10, -5 and 0 dB a total coding gain of 23.4, 22.6 and 23.8 dB was achieved, as shown in Figure 4.9. When compared to the theoretical gain of 10×log(300) = 24.7 dB, this corresponds to a difference of 0.6, 2.1 and 0.9 dB, respectively.

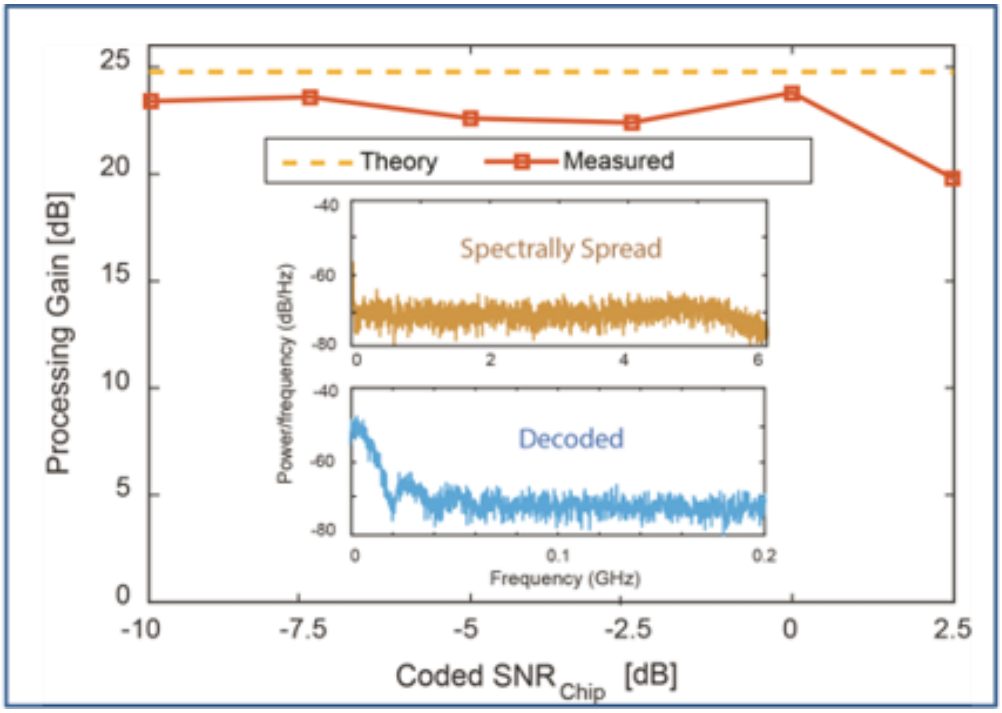

Figure 4.9 Decoding of a Subnoise Spread-Spectrum Signal. Theoretical coding gain of 300-fold spectral spreading (24.7 dB) compared with measurement. Insets measurements show the spectrally spread emission (6 GHz), and original decoded channel bandwidth (20 MHz).

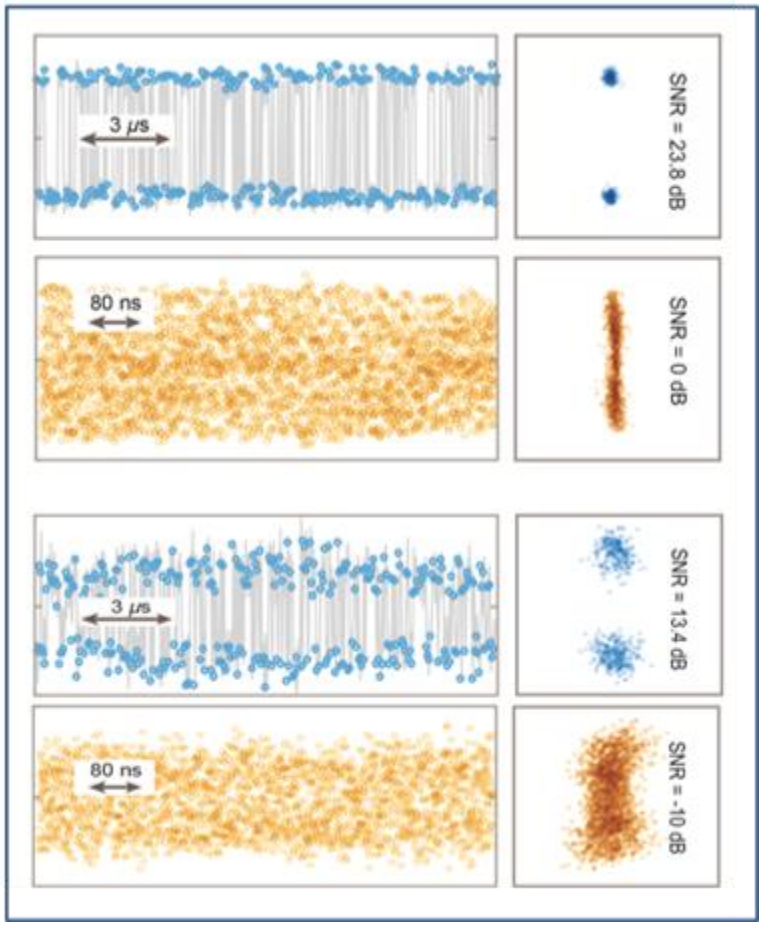

Figure 4.10 Received and decoded signals are shown in case when input SNR = −10 dB and 0 dB. Decoded channel SNR corresponds to 13.4 and 23.8 dB, respectively.

To demonstrate the capabilities of the proposed scheme in the presence of MPI, the timing delay of each path is demonstrated to be accurately measured. The timing offset is measured using the 25 subset receiver array shown in Figure 4.7A, and the offset is predicted using Eq. (4.2). Figure 4.11 shows the performance results of predicting the timing offset of each MPI path with various SNRs. As there are 4 timing predictions to be made for each received bit, the timing accuracy in Figure 4.11 is defined as the sum total of the correctly estimated timing offset for each path for every bit, divided by the total number of timing estimations (4×210). The results show that

with 30 bits of observation at 20 MHz, a high level of confidence can be achieved to predict the timing offset of each multipath.

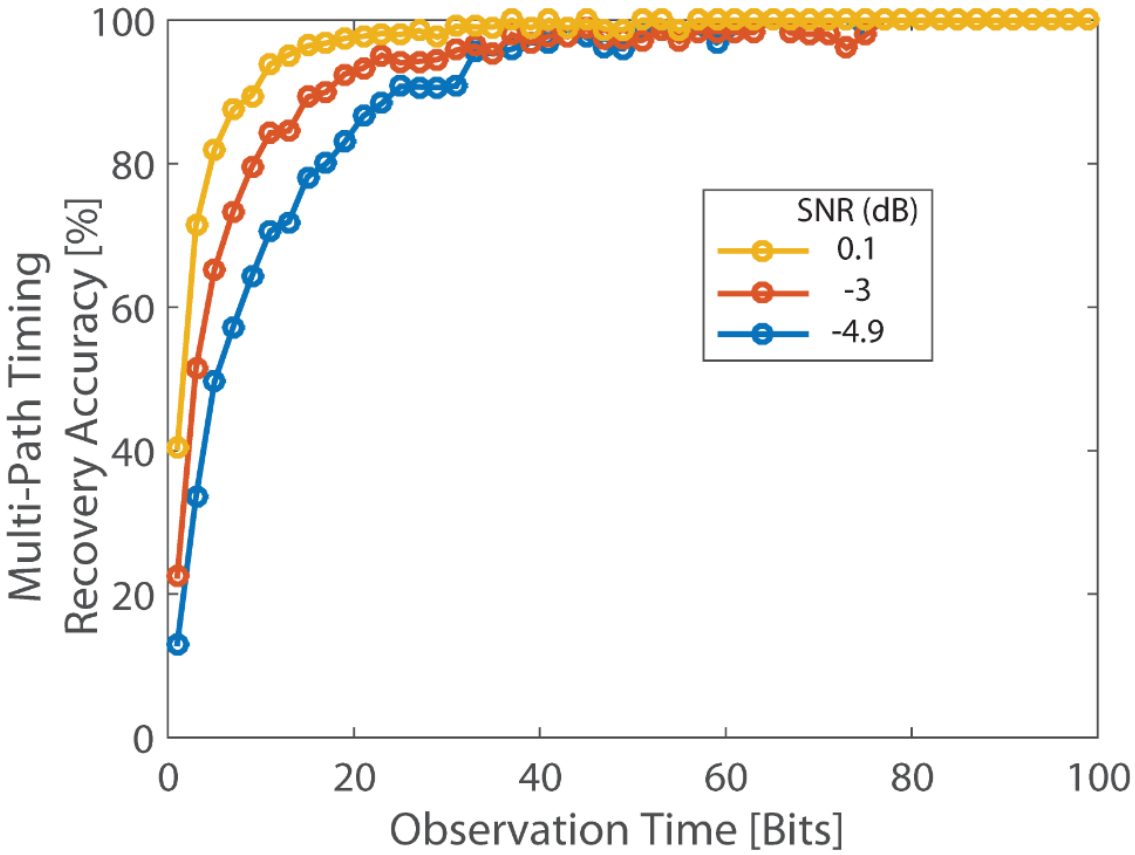

Figure 4.11 Measured synchronization performance of 6 GHz wide spread spectrum channel under MPI conditions. A subset of size 25 sub-rate detectors was used (see Figure 4.7A). Quoted SNR in legend corresponds to the main path SNR. Path 2, 3 and 4 had 1.6, 3.5 and 5.8 dB lower SNR, respectively.

These results prove that a spread-spectrum signal can be received and decoded in a computation-free manner. While this chapter describes the measurements of a 6 GHz-wide channel, it is clear that the new receiver speed can be easily scaled by increasing the count of mutually coherent frequency comb tones. In contrast to conventional receivers that are ultimately limited by the speed at which a signal can be digitized and subsequently processed, the new device offers a clear path to full RF

coverage that extends beyond 100 GHz, as described in the next section. Measurements indicate that the comb-assisted receiver can operate in asynchronous mode, even when the received signal is noisy. However, it is also clear that significant work remains on a new class of algorithms necessary to interpret low-speed waveforms produced by the comb-assisted receiver.

4.2 Comb Assisted High Spread Factor Spread Spectrum Receiver

The results from 4.1 have the unique advantage of performing synchronization and demodulation in real time, and with little computation by offloading much of the computational burden to the analog domain. Another advantage is that the same experimental setup can perform both synchronization and demodulation without changing any components. However, the main disadvantage to the approach is that the amount of spreading that can be achieved is limited by the number of available comb tones (<1000). As a result, if processing gains of 40 dB or higher are required, a different approach should be used as discussed in this section. Section 4.2.1 is dedicated to the principle of operation to achieve a high spread factor spread spectrum receiver. The experimental test bed is discussed in Section 4.2.2, with the results and concluding remarks in Section 4.2.3.

4.2.1 Principle of Operation

Arguably, the most challenging aspect of receiving a high spreading rate (>30 dB) DSSS channel is the synchronization process. Indeed, if synchronization is already achieved, the demodulation can be done simply by multiplying the known codeword

with the received signal in the analog or digital domain. With this in mind, if synchronization can be achieved quickly and accurately, large processing gains can be readily achieved. In this demonstration, a processing gain of nearly 40 dB is achieved with a novel synchronization technique and subsequent demodulation in the analog domain.

The synchronization was achieved using a similar technique as Section 4.1.1. However, a direct implementation of the timing estimation shown in Figure 4.1 for a DSSS channel with 40 dB processing gain would require over 800 optical receivers if 8% of the full backplane were chosen as the subset. Rather than constructing an optical frequency comb with 800 lines mated with an identical number of coherent receivers in the backplane, a new concept was developed to relax the total number of required comb lines and receivers. Specifically, two optical frequency combs, OFC_S and OFC_{LO}, are generated with a pitch of ΔF and $\Delta F+\delta f$, respectively. The received electrical spectrum is them modulated onto OFC_S by an MZM, effectively replicating the electrical spectrum onto each mode of the OFC. Instead of setting the pitch difference between the two combs to the data rate as was done in Section 4.1.1, the pitch difference between the two combs was increased by M times the data rate. Each comb can then be sent to an arrayed waveguide grating (AWG), and pairwise overlapping tones can then be sent to a coherent detector. Each coherent detector in this case should have a bandwidth of at least M times the data rate. Then, in the digital domain, an M point FFT can then be implemented after each coherent detector, allowing for each of the N DFT coefficients to be streamed in parallel in real time. Next, either a subset of coefficients can be chosen, or the entire N DFT coefficient array can be used, depending on the

available digital processing speeds. The conjugate of the DFT coefficients of the known codeword can then be multiplied in the digital domain, leaving only a linear phase, whose slope is proportional to the time of arrival difference. Next, the linear phase of the remaining coefficients can then be estimated, and the timing difference between the received signal and the known codeword can be removed by delaying the known codeword at the receiver. After synchronizing, the original transmitted bit sequence can then be extracted by multiplying the synchronized codeword with the received signal using an RF mixer.

4.2.2 Experimental Demonstration

To experimentally prove this newly developed system, a comb-assisted spread-spectrum synchronization receiver was constructed by deriving two mutually coherent but frequency-tunable combs from a single master laser to perform timing recovery. The signal comb (OFC_S), with the same experimental setup as described in Section 3.1, possessed more than 300 highly coherent optical frequency tones separated by ΔF_S = 25 GHz, with over 43 dB OSNR at 0.1 nm is plotted in . The LO comb had a similar construction and the pitch was set to ΔF_{LO} = 24.9375 GHz. The optical modulator was used to replicate the combined spread-spectrum and noise input onto N = 160 comb tones.

The receiver was first tested to measure the synchronization performance, as shown in Figure 4.12. To do this, a preamble was constructed by spreading a repeated 1 μs long bit to 10 GHz bandwidth. The preamble was spectrally spread in the digital domain, using a 13 GHz-wide pulse PG to synthesize a 10 GHz-wide coding sequence.

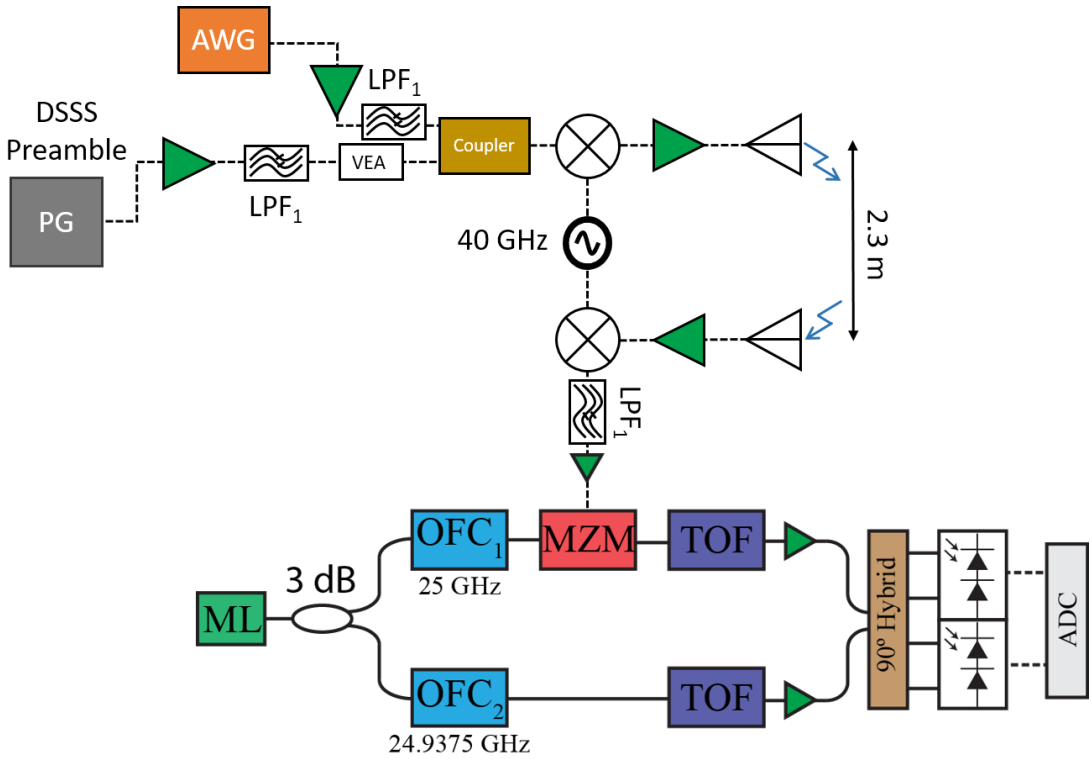

Figure 4.12 Comb-assisted spread spectrum receiver synchronization experiment. PG: Pattern generator, AWG: Arbitrary waveform generator, VEA: Variable electrical attenuator, ML: Master laser, OFC: Optical frequency comb, MZM: Mach Zehnder modulator, TOF: Tunable optical filter, ADC: Analog to digital converter.

The minimum transition time that could be created in this manner was 20 ps. The DSSS signal is created by DSP, prior to its mapping into the optical domain. The 1 MHz BPSK preamble content was generated by a 2^{10} long repeated "1" bit sequence. This bit pattern was then multiplied by a 10,000-long codeword, spreading the 1 MHz signal to 10 GHz bandwidth (chip duration Δt = 100 ps). The codeword was synthesized by selecting the first 10,000 symbols of a 2^{14} long PRBS. The resultant waveform was then uploaded to the PG and subsequently amplified by a 32 GHz bandwidth, 27 dB gain electrical amplifier. The output was then electrically low pass filtered to limit the output bandwidth to 7.46 GHz. Separately, a 6 GHz wide, 1.023 ms long WGN waveform was generated using a 10 GS/s, 10-bit resolution DAC. Digital noise generation, while

requiring a high-speed DAC, was specifically selected over a simpler, conventional (analog) noise source in order to allow for repeated backplane measurements under identical noise loading conditions, similar to the technique used in section 4.1.3. This allows for a complete and calibrated measurement of the receiver without physically assembling a full 160-detector sub-rate array. An arbitrary detector element response and its contribution to the array output can be measured by repeating the digital noise stimulus at the input. The synchronization between the noise-generating DAC and the data pattern generator was controlled to guarantee that the sequential capture of sub-rate detector outputs (corresponding to DFT coefficients) was performed under a precise noise-loading condition. The output of the pattern generator was attenuated to vary the received signal power and combined with calibrated noise power to create a given SNR level at the receiver input. The combined signal and noise were then upconverted using a double balanced RF mixer driven with a 40 GHz RF tone. The upconverted signal was then amplified with a 45 GHz bandwidth, 27 dB gain electrical amplifier. Next, the signal was transmitted wirelessly over 2.3 meters using a pair of 23 dBi gain pyramidal horn antennas. After reception, the signal was then amplified with a low noise, 4 GHz bandwidth (centered at 40 GHz), electrical amplifier. The signal was then downconverted using a second double balanced mixer driven with the same 40 GHz clock source. In a real system, an identical 40 GHz source would not be available on both the receiver and transmitter side, but due to the unavailability of equipment, a single 40 GHz tone was used in this experiment. After downconversion, another 7.46 GHz low pass filter was used to filter out only the downconverted signal, which was subsequently amplified using a 27 dB gain electrical amplifier. Finally, the

electrical signal was then imprinted onto modes of the signal comb using a null-biased MZM.

To synthesize the response of a fully populated detector array (i.e. 160 of 64 MHz bandwidth detectors), a tunable optical filter was used to select each channel from the signal and LO combs individually and route to a single coherent detector. Each of the 160 channels was digitized using a 64 MHz ADC and recorded. After capturing all tones offline digital signal processing was applied. The pitch difference (δf = 62.5 MHz), and receiver bandwidth (64 MHz) allowed for each of the 160 detectors to see 64 coefficients. Each of the receivers had an overlapping DFT coefficient, allowing for the random phase as a result from vibrational path length changes to be estimated and removed. After all of the 10,000 DFT coefficients were estimated for each of the transmitted 2^{10} bits, the phase of each of the coefficients were estimated. Next, the phase of the known DFT coefficients were subtracted, leaving only a linear phase, with a slope proportional to the time of arrival difference. The linear phase estimator used was similar to Eq. 4.2, except instead of multiplications, addition was used as only the phase is used:

$$\tau = \max_{\tau_i} \left| \sum_{k=1}^{N} e^{j(\arg(\tilde{X}[k]) - \arg(\tilde{C}^*[k]) - 2\pi k \delta f \tau_i)} \right| \tag{4.5}$$

where $\tau_i = i/(N\delta f),\ i = -\frac{N}{2}, -\frac{N}{2}+1, \ldots, \frac{N}{2}+1$. The main difference between this approach for timing estimation and the approach that was used in section 4.1 is that in this case, no channel selection function was used, meaning all 10,000 coefficients were utilized to estimate the linear phase. However, for computational complexity, if a look up table is used for phase estimation and the conversion to Cartesian coordinates, only

the addition operation is required, allowing for a large relaxation in the amount of processing power needed to estimate the linear phase. The performance of this method is discussed in the next section.

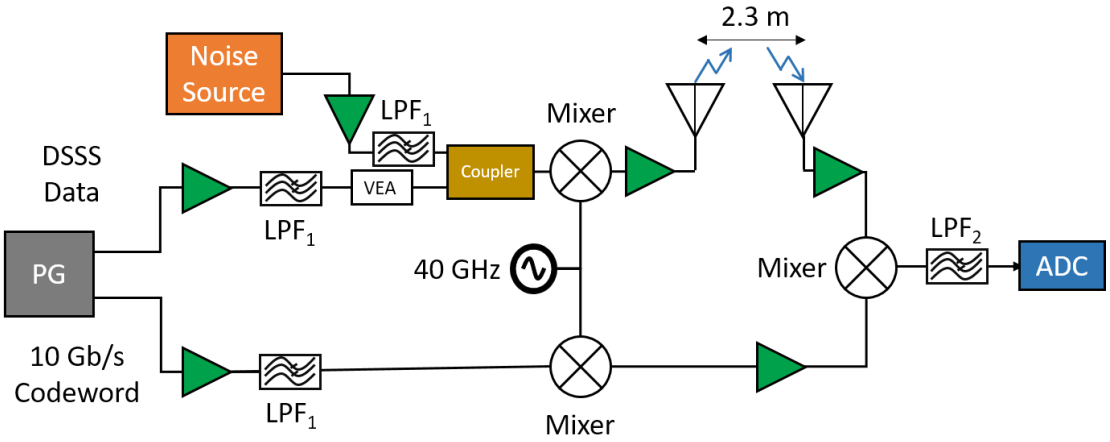

Figure 4.13 Synchronized demodulation setup. PG: Pattern generator, DSSS: Direct sequence spread spectrum, LPF: Low pass filter, VEA: Variable electrical attenuator, ADC: Analog to digital converter.

After timing estimation, the performance of the DSSS link can be characterized in terms of the processing gain. To experimentally test the processing gain, the experimental setup shown in Figure 4.13 was used. Specifically, a 2^{10} long, 1 MHz BPSK PRBS data sequence was generated digitally. The 1 MHz data sequence was then spread digitally to 10 GHz using the first 10,000 symbols of a 2^{14} long PRBS sequence. The spread data was then uploaded to the PG and subsequently amplified with a 32 GHz, 27 dB gain electrical amplifier. The amplified spread data was then low pass filtered to 7.46 GHz bandwidth. The signal power was controlled by a variable electrical attenuator to adjust the signal power relative to the noise and generate a calibrated SNR. The signal was then combined with a wideband (7.46 GHz) noise source. The noise source was generated by optical amplified spontaneous emission that

was band pass filtered to 0.6 nm bandwidth. The filtered optical noise was then amplified in an erbium doped fiber amplifier (EDFA) before being sent to a photodiode. The output of the photodiode was amplified with a 30 GHz bandwidth, 30 dB gain electrical amplifier, and then low pass filtered to 7.46 GHz bandwidth. The combined signal and noise were then upconverted using a double balance RF mixer driven with a 40 GHz sinusoid. The upconverted signal was then amplified with a 45 GHz bandwidth, 27 dB gain electrical amplifier. Next, the signal was transmitted wirelessly over 2.3 meters using a pair of 23 dBi gain pyramidal horn antennas. After reception, the signal was then amplified with a low noise, 4 GHz bandwidth (centered at 40 GHz), electrical amplifier.

A second channel of the PG was also used to generate the synchronized 10 GHz known codeword. The codeword was first amplified with a 12 GHz bandwidth, 16 dB gain electrical amplifier and subsequently low pass filtered to 7.46 GHz bandwidth. The amplified codeword was then upconverted using a double balanced RF mixer driven with a 40 GHz tone. The upconverted signal was then amplified using a 38 GHz bandwidth, 29 dB gain electrical amplifier. Finally, the received signal centered at 40 GHz, and the generated synchronized known codeword centered at 40 GHz were multiplied together in a doubled balanced RF mixer. The demodulated data sequence was then low pass filtered with a 225 MHz filter to help avoid aliasing of high frequency content. After filtering, the demodulated data was captured with a 350 MHz bandwidth ADC. Next, in the digital domain, a 1 MHz low pass filter was applied and the received Q^2 value was estimated. In an ideal system, an analog 1 MHz filter coupled with a 1 MHz bandwidth ADC could be used to avoid any digital processing. The

results of the synchronized demodulation scheme are presented and discussed in the next section.

4.2.3 Discussion

The results of the timing estimation are plotted in Figure 4.14. The input SNR is estimated by measuring the relative power between the electrical signal and noise using an electrical spectrum analyzer integrating over 10 GHz bandwidth. The input SNR was varied by changing the variable electrical attenuation of the signal, to match different SNR conditions. At high SNR, a single bit was sufficient to interpolate the 10,000-point

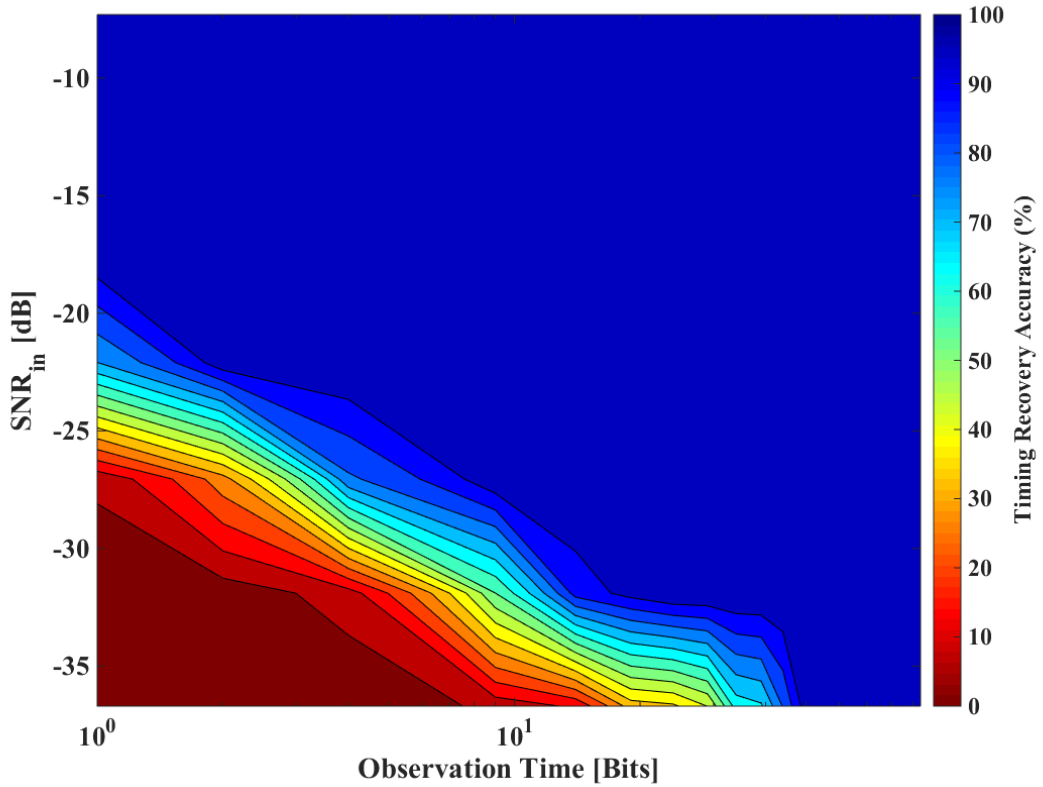

Figure 4.14 Measured synchronization performance of 10 GHz-wide DSSS channel generated by 10,000-long code and native 1 Mb/s data. Timing accuracy represents the number of correctly decoded bits from the received 2^{10}-bit long data stream.

DFT constellation in complex plane and achieve 100% timing accuracy. However, when the noise power is over three orders of magnitude higher than the signal (SNR<-35 dB), full timing accuracy required observation over 60 bits. This indicates that the preamble for timing estimation should be 60 bits long (60 μs for a 1 MHz data rate) if the signal is transmitted -36 dB below the noise. Assuming the velocity between the transmitter and receiver is under 100 mph, a 60-bit preamble will allow for a 600-bit data packet (payload) to be transmitted before the receiver needs to be resynchronized.

The ability to operate in asynchronous mode permits the ability to rigorously

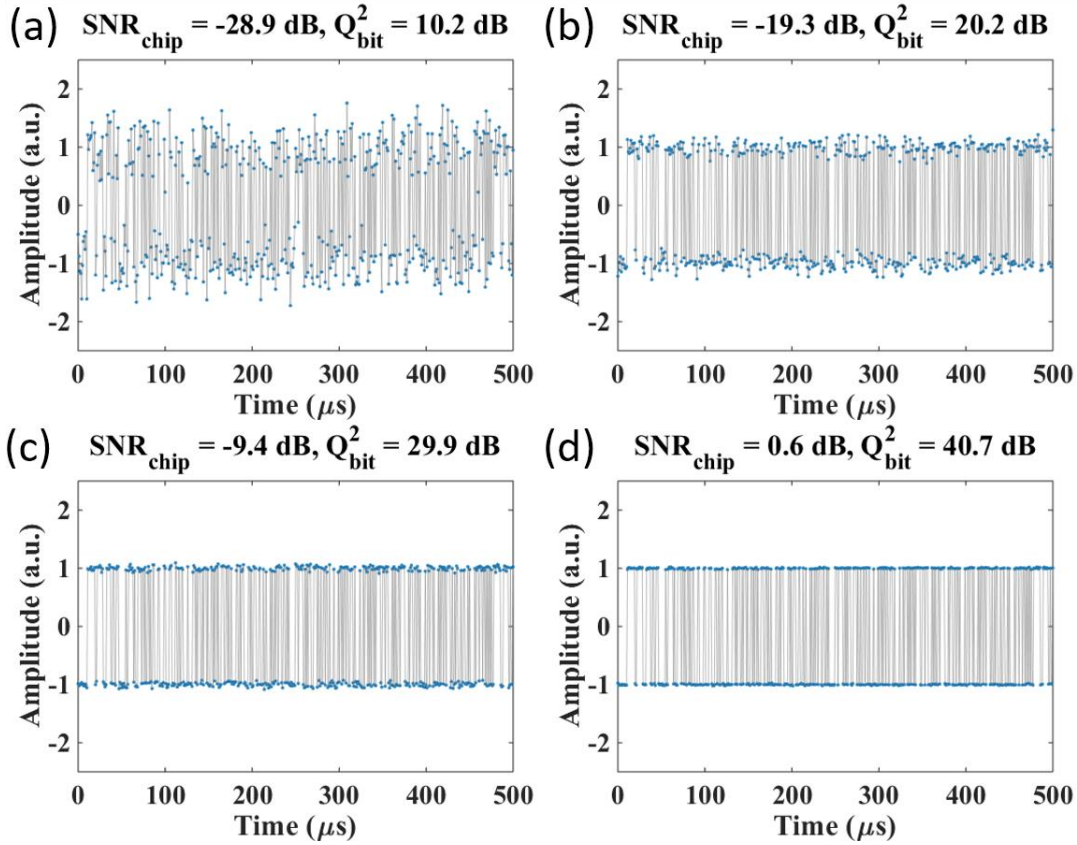

Figure 4.15 Experimental results for the demodulation scheme. SNR_{chip} represents input SNR measured with electrical spectrum analyzer. Q^2_{bit} represents measured Q value at output. (a) Input SNR of -28.9 dB and received Q^2 of 10.2 dB. (b) Input SNR of -19.3 dB and received Q^2 of 20.2 dB. (c) Input SNR of -9.4 dB and received Q^2 of 29.9 dB. (d) Input SNR of 0.6 dB and received Q^2 of 40.7 dB.

measure the processing gain, being the most important performance metrics of the new receiver. As a result, a 2^{10} long 1 Mb/s BPSK PRBS data packet was generated and spread to 10 GHz bandwidth. The transmitted signal was received and multiplied by the known synchronized codeword in the analog domain using an RF mixer. The Q^2 values of the demodulated data sequences were then estimated. Some examples of the received demodulated data sequences are plotted in Figure 4.15 for various input SNRs. Specifically, even when the transmitted signal was 28.9 dB below the transmitted noise field (SNR = -28.9 dB), the demodulated data was recovered with $Q^2 = 10.2$ dB, as shown in Figure 4.15(a).

The measured and ideal Q^2 values of the received demodulated data versus the input SNR is plotted in Figure 4.16(a). In Figure 4.16(b), the measured and ideal coding gain are plotted versus input SNR. Specifically, for input SNRs of -28.9 dB, -19.3 dB, -9.4 dB, 0.6 dB, total processing gains of 39.1 dB, 39.5 dB, 39.3 dB, 40.1 dB were achieved, respectively, as shown in Figure 4.16(b). If compared to the theoretical

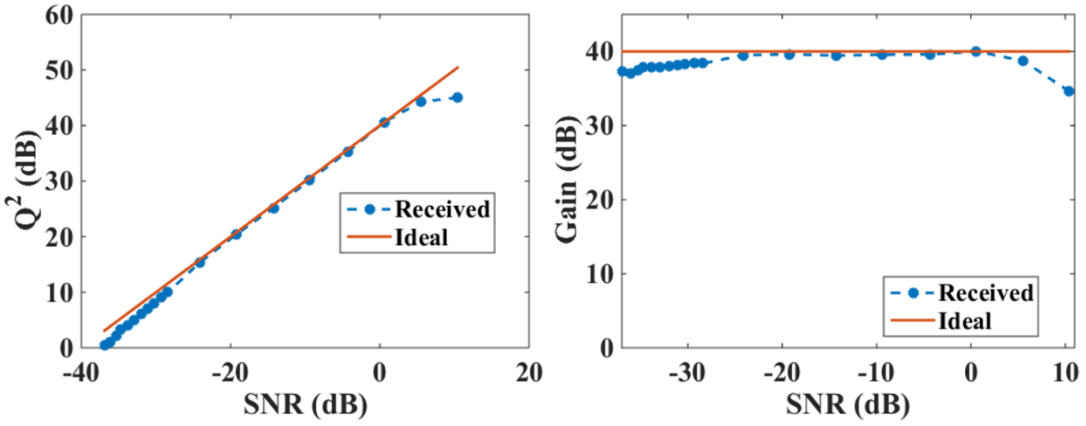

Figure 4.16 Experimental results for the demodulation scheme showing the measured Q^2 value measured at the output versus input SNR and the measured and ideal processing gain of the DSSS receiver versus input SNR.

processing gain of 10×log(10,000) = 40 dB, this corresponds to a deviation of 0.9 dB, 0.5 dB, 0.7 dB, and 0.1 dB, respectively. At high input SNR (>10 dB), the received processing gain deviates from the ideal processing gain by over 5 dB. The main reason for this is that the received demodulated signal ideally should have a >50 dB Q^2 value. This value sets a strict SNR limit on the RF mixer linearity and receiver SNR, which will ultimately limit the total receive SNR, as indicating by the measured curve in (a) saturating at higher input frequencies. However, this receiver is not designed to detect signals transmitted above the noise floor, but rather, signals buried under noise by orders of magnitude in power.

Similar to Section 4.1, these results prove that a spread-spectrum signal can be received and decoded in a computation-free manner, even when the spread factor approaches 10,000. The increase in the spreading factor to such amounts is a direct result of shifting the demodulation to the electrical domain, coupled with the idea that each coherent detector can receive multiple DFT coefficients simultaneously. While this section describes the secure transmission of a 1 Mbps BPSK data sequence, it is clear that the new receiver can be adapted to transmit much faster data with this technique. The measurements indicate that the comb-assisted receiver can operate wirelessly in asynchronous mode, even when the signal is buried more than 30 dB under the background noise.

4.3 Pulse Position Modulation Receiver

Recognizing the frequency hopping pulse position modulation (FH-PPM) UWB reception challenge discussed in Section 2.3, a new receiver was developed, with a

specific goal of eliminating the high-rate electronic front-end. The new architecture rests on the idea of physical spectral decomposition, allowing for a relaxation in the required processing speed of the backplane electronics. Section 4.3.1 is dedicated to the principle of operation for the newly developed receiver. The experimental testbed is discussed in Section 4.3.2, with results and concluding remarks in Section 4.3.3.

4.3.1 Principle of Operation

The principle of the PPM receiver relies on three unique attributes: low-noise and low-distortion coherent signal replication, filter-less frequency decomposition, and a single-step phase estimation. A simple overview of the principle is shown in Figure 4.17, a more extensive discussion can be found in [22]. The received FH-PPM signal is replicated in a noise- and distortion-free manner by modulating an optical frequency comb, pitched at ΔF. Effectively, the electrical signal field (rather than its spectral power) is replicated onto each of the N modes (carriers) of the comb. The filter-less frequency decomposition is achieved by generating a second reference optical frequency comb with a precise frequency pitch offset by δf with respect to the signal comb. Next, the optical modes are then separated with a spectral demultiplexer, and overlapping tones sent to a coherent detector element. This allows for the reference comb tone to beat with a specific portion of the FH-PPM spectrum and down-convert its immediate spectral vicinity. In essence, each of the sub-band frequency slices of the original RF spectrum are addressed by self-referenced LO modes. As a result, only low-speed coherent detectors and sub-rate electrical digitizers are necessary to synthesize

bandpass frequency filtering, rejecting the signal content that is too distant from the selected signal frequency slice of the received signal.

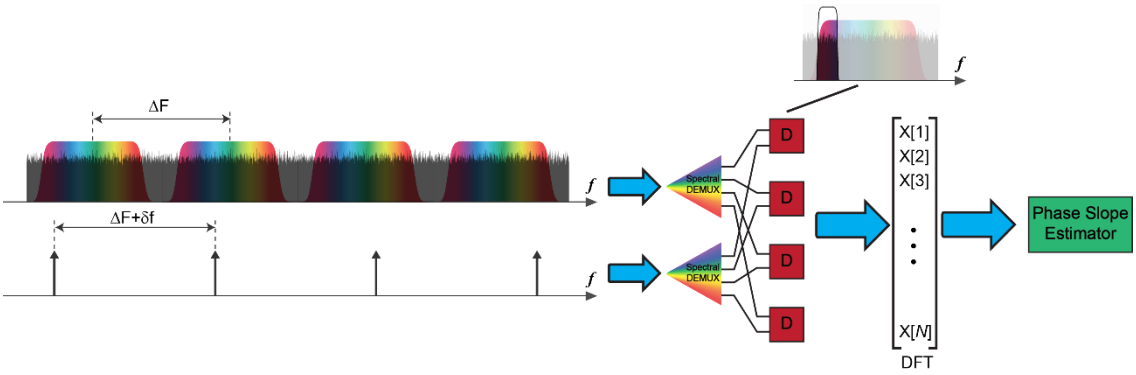

Figure 4.17 Comb-Assisted FH-PPM Receiver. Signal optical frequency comb and Vernier reference comb are generated with a pitch of ΔF and $\Delta F+\delta f$, respectively. The signal comb is modulated with the incoming electrical signal effectively replicating it onto each comb tone and the Vernier reference comb is used as probe to select which frequency component of the signal is digitized. A coarse spectral demultiplexer splits the replicated signal and Vernier comb tone pairs into individual coherent detectors, yielding the DFT coefficients. A linear phase slope estimator is then employed to retrieve the transmitted data stream. D: Coherent Detector.

Next, the decomposed spectrum is sent to low speed electrical digitizers. In effect, these stream the measured DFT coefficients of the FH-PPM RF signal without any additional computation step. Finally, the phase is extracted from each of the DFT coefficients, and a linear phase slope estimator is used to decode the position of each transmitted pulse. Physical access to the complex DFT of the received signal eliminates the need for high-rate computation that must match the rate (bandwidth) of the incoming signal. In case of ordinary (single-carrier) PPM demodulation, the frequency phase slope should be measured to estimate the received pulse position. Consequently, the resolution of the frequency decomposition should be sufficient to provide accurate pulse position estimation: the resolution in this case is directly proportional to the number of frequency comb tones used. Correspondingly, a wideband optical frequency comb with high tone count is superior but imposes distinct implementation challenges.

In the simplest implementation, the architecture calls for a complement of coherent detectors that matches comb tone count. To stream hundreds of DFT coefficients simultaneously, it appears that a significant hardware burden must be accepted, since a large number of receivers and digitizers would need to be employed.

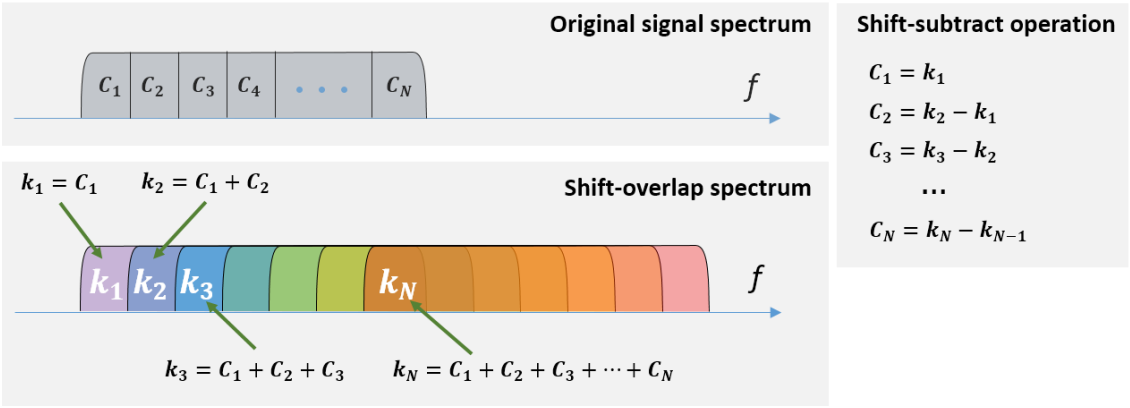

Figure 4.18 Frequency shift-and-subtract algorithm. The original signal spectrum is overlapped into a single coherent receiver. Subsequently, a frequency shift-subtract operation can be used to extract the original signal spectrum.

However, each receiver-digitizer element operates at a very low speed compared to the FH-PPM bandwidth, allowing for a full bank of low-dissipation architecture to be monolithically integrated. Alternatively, multiple DFT coefficients can be processed by a single, faster receiver-digitizer element. To do this, a wideband spectral demultiplexer is implemented, simultaneously selecting multiple frequency tones from each of the optical frequency combs to be received by a coherent detector. The input electrical spectrum will then be shifted M times in frequency by the frequency comb pitch difference and repeatedly added to itself, as illustrated in Figure 4.18. To extract each of these M DFT coefficients, a digitizer must have sampling bandwidth of $M\delta f$, with $M<<N$. In the DSP domain, a shift and subtract operation could be utilized to extract each of the M DFT coefficients, while still not requiring a strict, optical filtering layer.

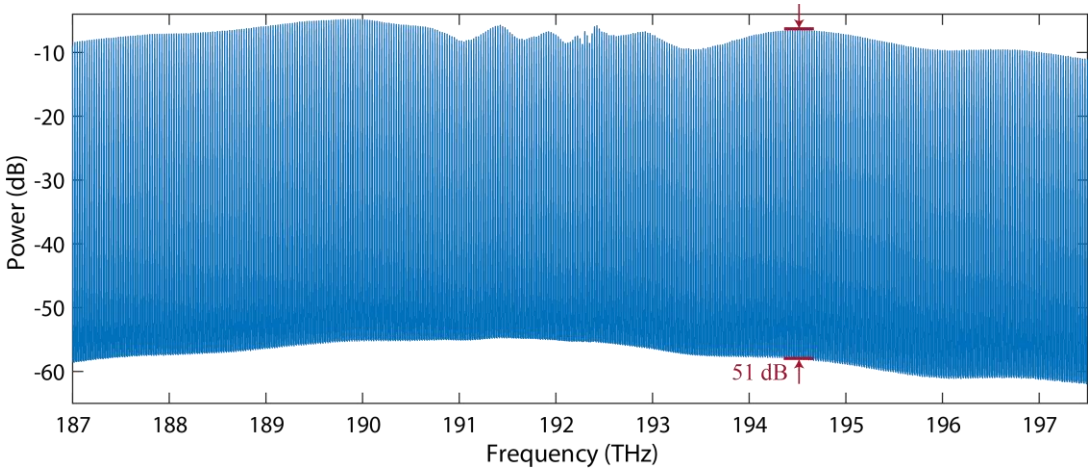

Figure 4.19 Generated 25 GHz tunable optical frequency comb with 0.02 nm resolution bandwidth.

4.3.2 Experimental Demonstrations

The receiver architecture relies on the generation of two, high fidelity, frequency locked optical frequency combs each with high power per generated tone, frequency stability, frequency configurability, and spectral purity. To meet these requirements, two tunable optical frequency combs (OFC) were generated using a cavity-less seed source, as described in Section 3.1. The master seed for both OFCs was a single, narrow-linewidth master oscillator operating at 1559.2 nm. The master oscillator was split into two paths with a 3 dB coupler to seed both OFCs. In each arm, broad optical pulses were carved with an MZM, driven with a 25 GHz RF tone. Next, the pulses were routed to a compression stage where the broad pulses were first chirped using a phase modulator driven with the 25 GHz tone. The chirped pulses were then compressed in single mode fiber (SMF). After amplification and subsequent filtering, the pulses were subject to a second compression stage. The chirp in this stage was induced by SPM in an HNLF. The pulse compression was again achieved in a second

SMF stage. Next, the pulse pedestals were then suppressed in a NOLM. Finally, the high peak power pulses were routed into a final HNLF stage for generation of a wideband 25 GHz optical frequency comb. The high quality 25 GHz OFC with $OSNR_{0.1nm}$ over 40 dB is shown in Figure 4.19. Additionally, a second OFC was generated with a pitch of 24.92 GHz, indicating a pitch offset of 80 MHz between the two generated combs.

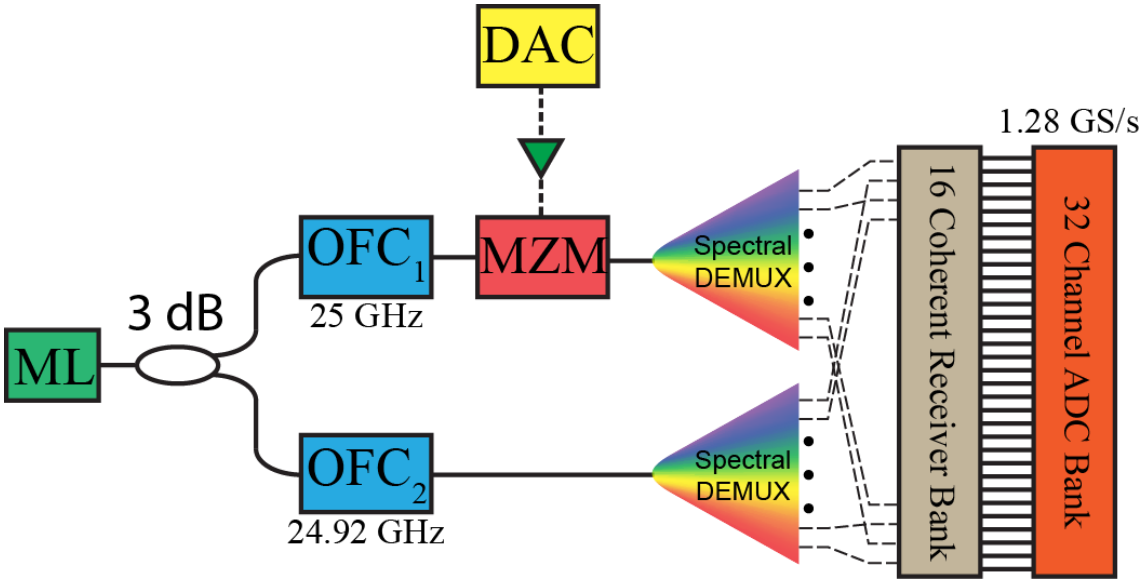

Figure 4.20 Experimental Setup. ML: Master laser, DAC: Digital-to-analog converter, ADC: Analog-to-digital converter.

The 25 GHz comb was sent to a MZM as shown in the schematic in Figure 4.20, where the received electrical signal was modulated onto each of the comb tones. The electrical signal was synthesized using a 64 GS/s DAC. The DAC was programmed with the FH-PPM data and was electrically amplified and used to modulate the comb. Subsequently, the two generated optical frequency combs were sent to a constructed coarse spectral demultiplexer. The demultiplexer block consisted of a bank of wavelength division multiplexers (WDM) that emulated a conventional (single-element) spectral demultiplexer with 400 GHz spacing. As a result, a 16 port spectral

demultiplexer was realized, each with 16 adjacent optical frequency tones spaced 25 GHz apart. Specifically, each of the 16 ports carried 16 signal tones from the signal comb and an identical 16 ports were constructed for the overlapping 16 tones from the reference comb. Each of these ports were then routed into separate coherent receivers. The received data was then captured with a bank of 32 ADCs, one for each quadrature, each operating at 1.28 GS/s. As a result, each pair of receivers yields 16 DFT coefficients at a 12.5 ns (1/80 MHz) update rate.

After capturing all 16 I/Q channels, DSP was applied to extract each of the 256 DFT coefficients, using the frequency shift-and-subtract method. Subsequently, with 256 estimated DFT coefficients spanning 20.48 GHz, the bandwidth of interest is selected, and the phase is calculated in each of the corresponding DFT coefficients. Finally, the phase slope is estimated using the physically acquired DFT coefficients, and the pulse position is extracted. This process is repeated for each of the transmitted pulses.

4.3.3 Discussion

The system performance was characterized first with an 80 Mbps PPM signal. The pulses generated were raised cosine shaped pulses with 0.25 roll-off factor, 320 MHz bandwidth, 20 MHz average repetition rate, and modulated with 16 time positions. The electrical signal was also up-converted to 1.92 GHz, and for this initial test, no frequency hopping was used. The electrical PPM signal was then modulated onto the 25 GHz optical frequency comb and subsequently sent to the receiver

backplane. After estimating the phase slope from the resulting DFT coefficients, the received PPM stream was estimated.

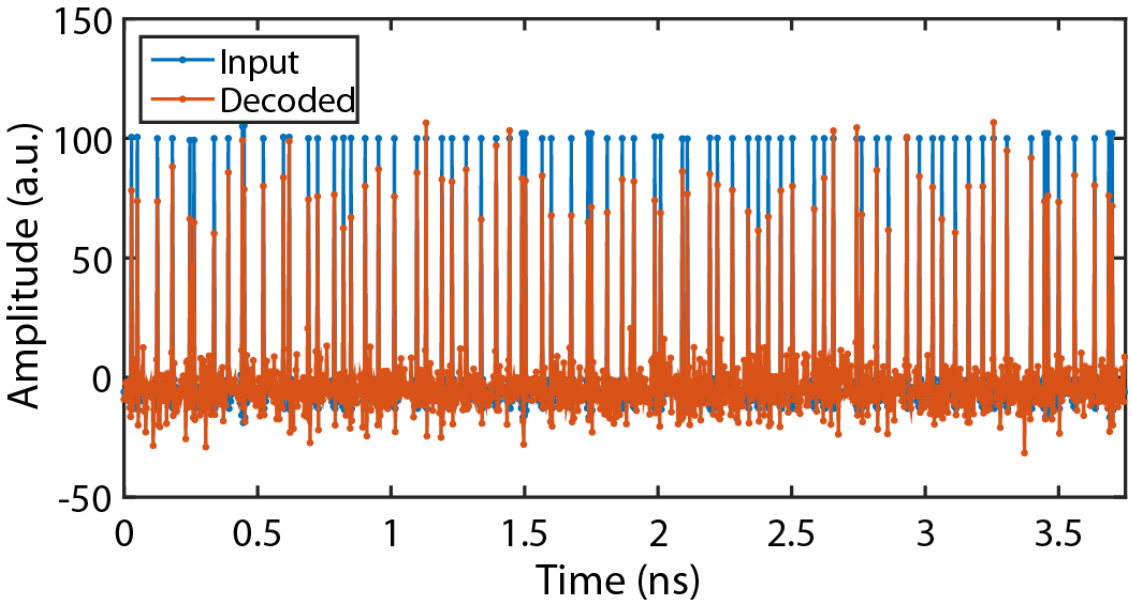

Figure 4.21 Transmitted and received 80 Mbps PPM signals.

The performance of the new receiver architecture was characterized in two ways: first, the inverse Fourier transform was performed using the received DFT coefficients, constructing the time-domain data which was then compared to the transmitted pulse stream. Second, the SNR at the output was measured, defined as the amplitude squared of the received data where a pulse is present divided by the variance of the received noise. The inverse Fourier transform implemented here was only used for characterization of the receiver architecture: the new receiver does not need an inverse Fourier transforms to be computed since only the slope of the phase function needs to be estimated. The performance results are shown in Figure 4.21, showing a successful demodulation of the transmitted 80 Mbps PPM signal, achieving an SNR of 23.2 dB at the receiver. In Figure 4.22, the measured results both before and after the

shift and subtract rectification are shown. The performance of the receiver is indeed greatly limited by the accuracy of the shift and subtract method. Ideally, a full receiver backplane would overcome this limitation.

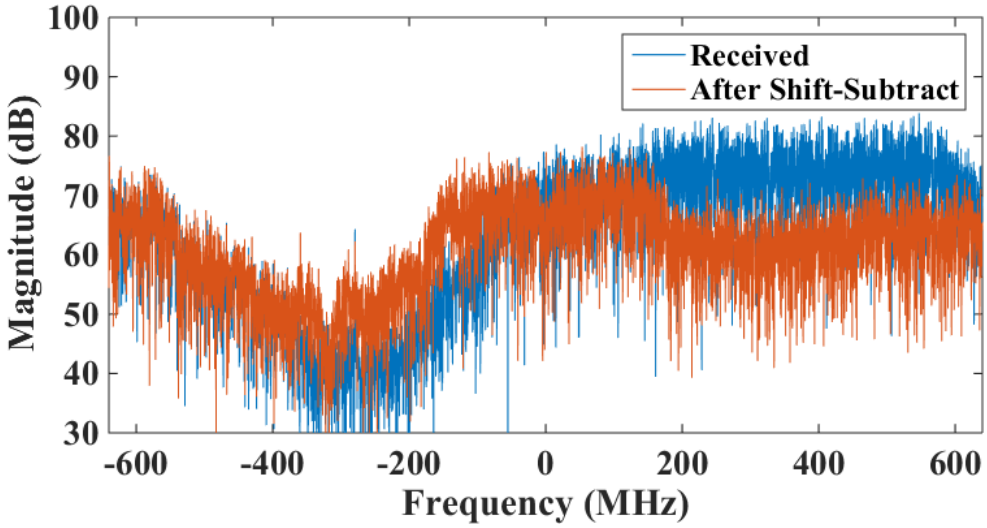

Figure 4.22 Electrical spectrum before and after the shift-and-subtract operation.

The system performance was also characterized for a faster signal, consisting of a 160 Mbps PPM signal. The 160 Mbps PPM signal consisted of raised cosine pulses, 640 MHz bandwidth, 40 MHz average repetition rate, and 16 modulated pulse time positions. The PPM signal was then upconverted to 1.28 GHz. The performance results of the demodulation are plotted in Figure 4.23. Even at double the data rate, the receiver can still demodulate the PPM data successfully. The 160 Mbps PPM channel was characterized with 15.2 dB SNR, indicating the scalability of this architecture. The performance was again limited by the shift and subtract method, and due to having a larger bandwidth, or equivalently, possessing more DFT coefficients to estimate, the shift and subtract method performed even worse. Still, the receiver architecture was

successfully scaled to double the original data rate, and could nevertheless be demodulated. Indeed, with a full receiver backplane, the shift and subtract method would not be necessary, and as a result, the performance of the receiver would be significantly better.

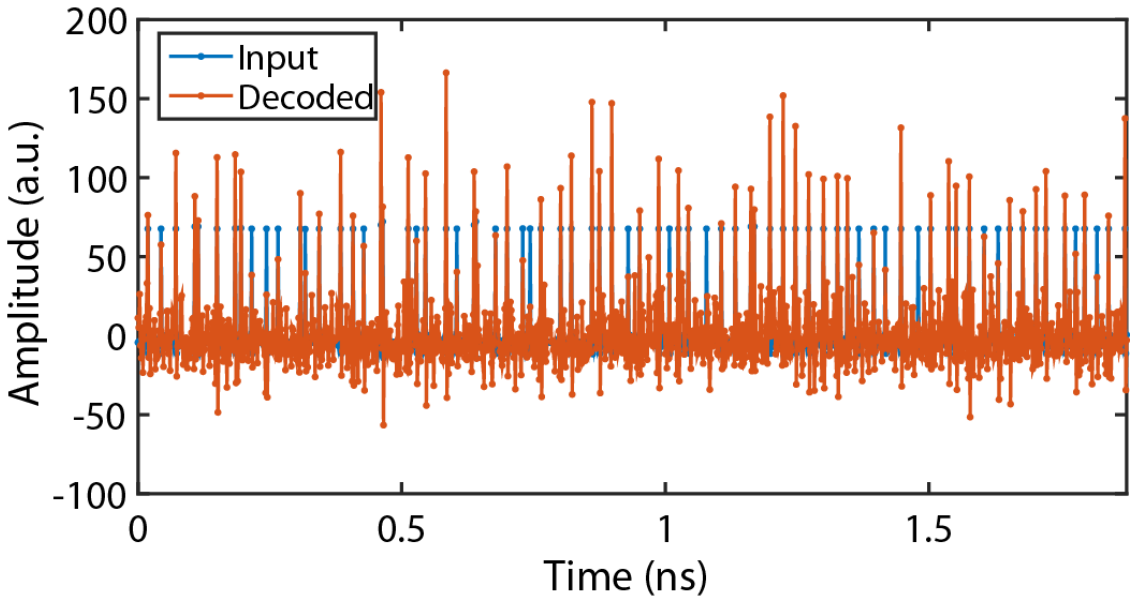

Figure 4.23 Transmitted and received 160 Mbps PPM signals.

Finally, to demonstrate the versatility of the proposed receiver, frequency hopping was implemented. In particular, an 80 Mbps PPM signal with 20 MHz average repetition rate, 320 MHz bandwidth, and 16 pulse positions was generated. The signal was programmed to randomly frequency hop between 1.6 GHz and 4.16 GHz carrier frequencies with 20 MHz average hopping rate. The carrier frequencies were specifically chosen so that the signal would fall into two distinct receivers. The two coherent receivers stared at the frequency ranges of 1.28 GHz to 2.56 GHz and 3.84 GHz to 5.12 GHz, respectively. The performance of the reception in each receiver is shown in Figure 4.24. The two receivers were successful in capturing both carrier

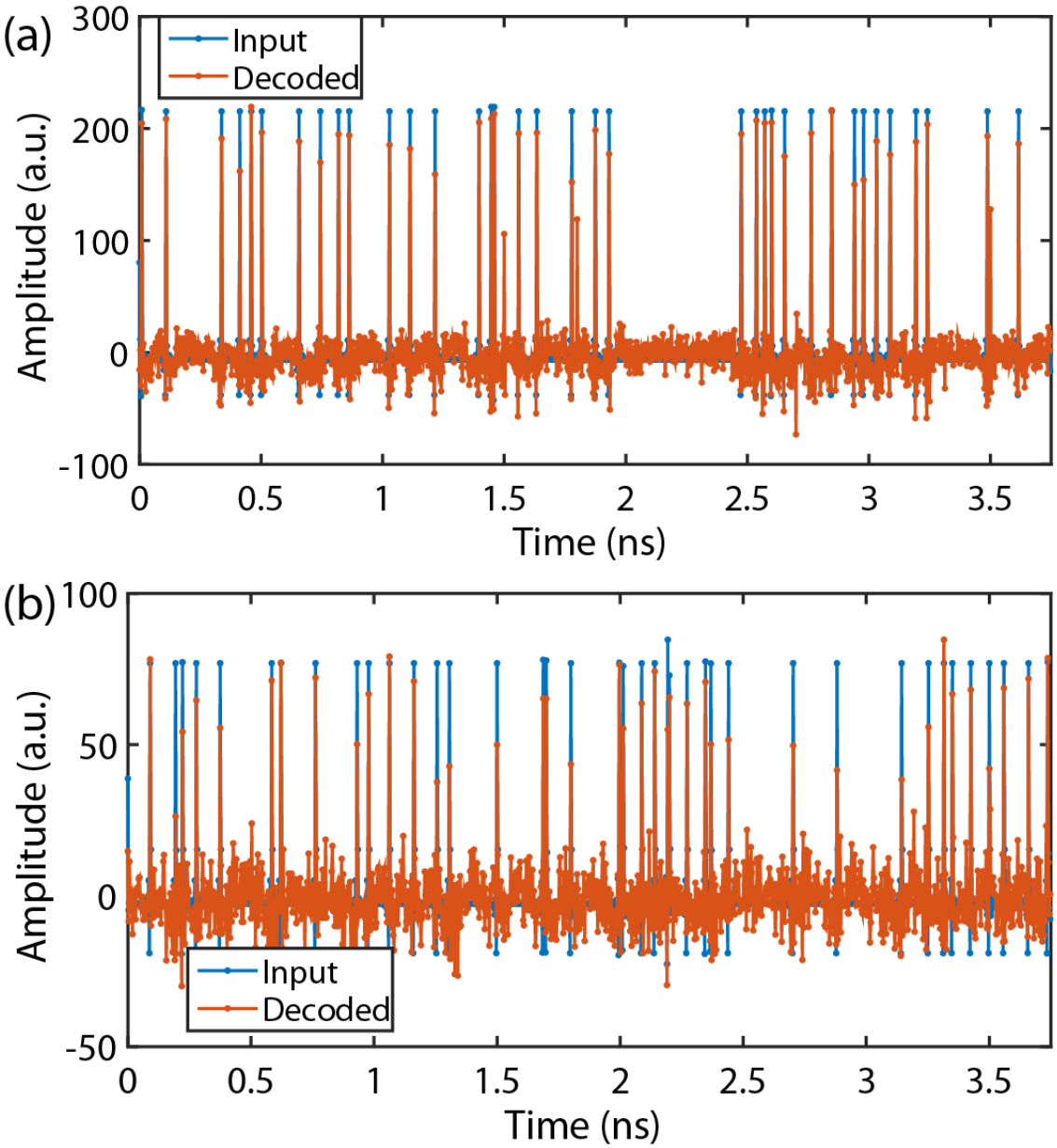

Figure 4.24 Transmitted and received 80 Mbps PPM signal frequency hopping between (a) 1.6 GHz and (b) 4.16 GHz.

frequencies, allowing for accurate demodulation of the transmitted PPM signal. The receiver was characterized with 19.8 dB and 13.4 dB SNR for the 1.6 GHz, and 4.16 GHz carrier frequencies, respectively.

The receiver was designed and the performance was characterized as an agile frequency hopping PPM receiver. The new architecture represents a low-complexity

receiver and needs only a linear phase estimator to successfully demodulate a FH-PPM signal. The receiver performance was characterized with both an 80 Mbps and 160 Mbps PPM input stream. The versatility of the receiver was also demonstrated in the capture of a frequency hopping 80 Mbps PPM signal. While the receiver performance was defined by the accuracy shift-and-subtract method in the backplane, each of the transmitted FH-PPM signals were successfully demodulated. A full scale architecture, populated with sub-rate detector array, circumvents the need for iterative DFT recovery, since each frequency component is addressed independently by a single (low-rate) receiver. The unique ability to simultaneously address a large RF bandwidth exceeding 20 GHz, and support high frequency resolution was leveraged to detect and demodulate a frequency hopping UWB PPM signal experimentally for the first time. While results represent an important operational mode of the comb-assisted receiver, it is clear that a more efficient backplane construction and matching algorithms will lead to an even more efficient and faster sub-noise link realization.

Chapter 4, in part, is a reprint of the material as it appears in the IEEE/OSA Journal of Lightwave Technology, volume 34, issue 22, 5214-5219 (2016), titled "Subnoise Signal Detection and Communication," by Daniel Esman, Vahid Ataie, Bill P.-P. Kuo, Nikola Alic, and Stojan Radic. Chapter 4 also contains in part material submitted for publication as it may appear in the IEEE/OSA Journal of Lightwave Technology, titled "Comb Assisted Spread Spectrum Subnoise Wireless Communication Link," by Daniel J. Esman, Vahid Ataie, Bill P.-P. Kuo, Nikola Alic, and Stojan Radic. Lastly, Chapter 4 in part is a reprint of the material as it appears in the IEEE/OSA Journal of Lightwave Technology, volume xx, issue xx, x-x (2016),

titled “Frequency-Hopping Pulse Position Modulation Ultrawideband Receiver,” by Daniel Esman, Vahid Ataie, Bill P.-P. Kuo, Nikola Alic, and Stojan Radic. The dissertation author was the primary investigator, and the primary author of these articles.

Chapter 5 Transient Signal Detection

Recognizing the transient signal detection challenge discussed in Section 2.4, a new receiver was developed, with a specific goal of eliminating any conventional replication techniques and any high-rate electronic front-end. The new architecture rests on the idea of physical spectral replication by use of an OFC. Subsequently, physical spectral decomposition can be achieved to allow for a relaxation in the required processing speed of the backplane electronics. Section 5.1 is dedicated to the principle of operation for the newly developed receiver. The experimental testbed is discussed in Section 5.2, with results and concluding remarks in Section 5.3.

5.1 Principle of Operation

To describe noise discrimination in a single-instance signal, consider a set of lossless periodic bandpass filters with bandwidth δf, as shown in Figure 5.1(a). When mapped contiguously, the N-filter set covers the entire signal bandwidth, defined as $\Delta f = N\Delta f$. Each filter selects a specific sub-band, spectrally decomposing the total received field $r(t)$ that combines the signal $s(t)$ and noise $n(t)$. If the filter output is shifted to baseband (i.e. k-th filter output is translated in frequency from $f_k = k\delta f$ to $f = 0$), then the resulting spectral decomposition can be described by the short-time Fourier transform (STFT) $\int_{-1/2\delta f}^{1/2\delta f} w(t-\tau)r(\tau)e^{j2\pi k\delta f\tau}\,d\tau$, where $w(t) = \sin(\pi\delta f t)/\pi t$ is a window function with bandwidth δf. Since the STFT is a bandlimited, complex function, then sampling within the interval $[t \pm 1/(2\delta f)]$ [80] can be associated with the phasor sum

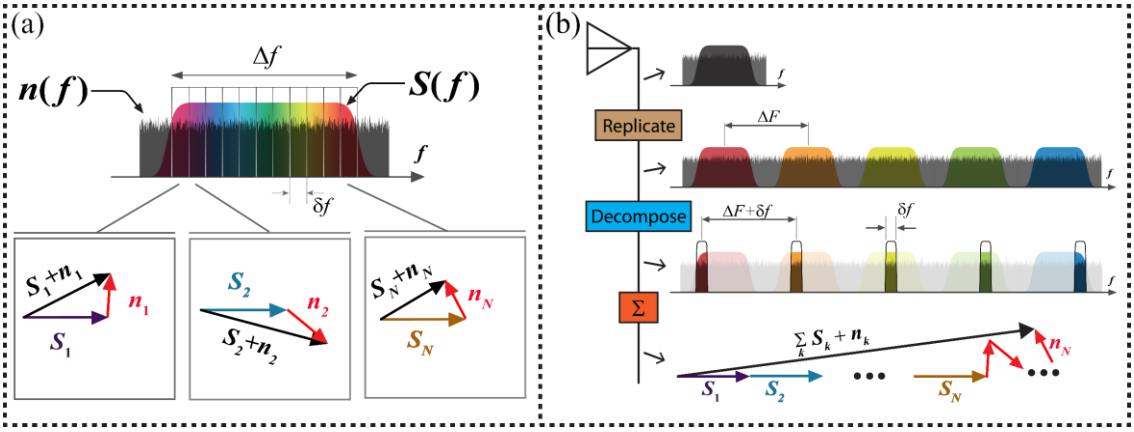

Figure 5.1 (a) Spectral decomposition of signal spectrum, $S(f)$, and noise spectrum, $n(f)$, by ideal bandpass filters (δf) yields set of S_k and n_k phasors. (b) Single-event noise discrimination is achieved by replicating the single event spectrally, and decomposing the signal to generate set of S_k and n_k phasors. Bringing each decomposed element to baseband and subsequent summation yields coherent signal phasor summation, thus allowing for spectral averaging.

$R_k(f) = S_k(f) + n_k(f)$. In this notation, $R(f)$ corresponds to the Fourier transform of the total received field $r(t)$. In the ideal case, when only signal is present and noise is absent, the magnitude of R_k corresponds to the incoming signal spectral density centered at f_k. When only noise is present, the magnitude of R_k is defined by the statistics of the incoming noise field centered at f_k, and, in practical terms characterizes the interferer power. Consequently, when only achromatic noise is present in the incoming field, factors comprising the spectral decomposition are inherently uncorrelated, as long as the spectral width of each sub-band remains finite. Intuitively, in case of a noiseless transform-limited signal pulse, this decomposition is readily associated with a set of collinear phasors; the magnitude of a specific phasor simply measures the signal strength in a specific frequency bin. As a result, by summing these spectral decomposition components that span Δf, each with bandwidth δf, the effective SNR enhancement compared to the performance of a single channel with bandwidth δf should scale with replication count N as $\sim \left(\frac{N}{\sqrt{N}}\right)^2$ [81]. However, the SNR enhancement

should no longer scale with N if the bandwidth of each of the spectral slices is increased so that the total bandwidth of all the spectral decomposition slices is larger than Δf, since outlier spectral slices do not contribute to coherent summation. Intuitively, this is the spectral analogue of the conventional time averaging: SNR enhancement is only observed if the signal averaging is performed over a time when the signal is present.

Although the single-event detector is conceptually simple, its realization faces a set of basic challenges. In the first of these challenges, the spectral decomposition process must be distortion-free and lossless. This requirement is easily satisfied for slow, microsecond-scale events that can be quantized with high precision [12], [13]. In this case, the digitized field can be used to calculate the sampled STFT and emulate the coherent sub-band summation (Figure 5.1(a)). However, when the event is fast (sub-nanosecond), signal quantization imposes a fundamental resolution limit [12], [13], eliminating such a computational approach. Its alternative, physical channelization [82], is neither distortion-free nor lossless.

To achieve such an SNR enhancement, an incoming RF signal must be first replicated onto multiple, equidistant optical frequency modes that are separated by ΔF, as shown in Figure 5.1(b). While spectral decomposition can be readily realized by periodic optical filters such as a Fabry-Perot and more complex structures [83], these are inherently lossy, introduce chromatic distortion and do not remove the carrier frequency offset. To address these deficiencies and simultaneously down-convert each spectral bin to baseband, a coherent receiver is used in conjunction with a matched LO comb with frequency pitch $\Delta F+\delta f$. It should be noted that this technique can also be applied to an incoming optical signal and is not limited only to the RF domain. In case

when a signal of interest is in the optical domain, the incoming field can be replicated using parametric cloning [84], and a similar technique that matches the coherent receiver backplane with LO comb can be applied.

In a full-scale implementation of a comb-assisted receiver, the replicated optical signal comb and the optical LO comb are routed by a chromatic element such as a high channel count AWG [85], to a set of slow (sub-rate) coherent receivers. As a result, each detector yields a single spectral decomposition component (phasor) of the received field. Subsequently, measured phasors are selectively added to achieve the desired degree of averaging and noise separation. To demonstrate the scalability of this architecture without a fully populated sub-rate detector array, the performance of a comb-assisted receiver can be rigorously characterized by a single coherent receiver. Similar to the characterization technique long established in WDM transmission, where performance of each channel is measured sequentially (using a single receiver), it is possible to apply a nearly identical strategy here. Mirroring the WDM characterization, a single, sub-rate coherent receiver is used to sequentially sweep over each of signal and LO optical modes until the full spectral composition is acquired. However, this approach also requires that the noise portion of the receiver stimulus be accurately repeated during each measurement instance. Consequently, the noise is synthesized digitally and converted to an analog waveform that must be combined with the signal stimulus during each measurement. While this procedure allows for scaled receiver testing without supplying the fully populated sub-rate detector backplane, it also imposes two rigorous requirements. First, the noise portion of the stimulus must be generated by a DAC that possesses sufficient bandwidth and resolution (effective

number of bits – ENOB). At the minimum, DAC bandwidth must match the signal of interest and provide sufficient ENOB to match SNR level. Secondly, the entire receiver construct, and primarily two frequency combs must remain stable (with respect to frequency and noise characteristics) during the entire measurement procedure. In practical terms, this poses a significant challenge that can be addressed by mastering both frequency combs using a single laser oscillator.

The received spectral decomposition components of a noiseless, transform-limited pulse each have a phase offset from each other. The phase offset is from two effects: a random, slow phase variation, and a deterministic linear rotation. The former phase offset is well known in channelizer devices [86], and full field analyzers [87], and is attributed to slow path-length variations in the fiber waveguide. These random phase fluctuations can be easily mitigated by frequency overlapping [87], dithering [88] or by sending a short preamble [22] before an actual measurement takes place. On the other hand, the deterministic linear phase rotation is a result of the inherent random time of arrival of the incoming pulse. As the spectral decomposition performed by the cloning receiver can be represented as a STFT, a pulse delay in time necessarily results in a linear phasor rotation in the Fourier plane. To arrest this rotation, the linear phase can be estimated [22] and subsequently removed. In particular, to avoid well-known phase unwrapping issues for low SNR linear phase estimation [89], the maximum likelihood linear phase estimator is used [77] as described in Eq. (4.2).

5.2 Experimental Demonstration

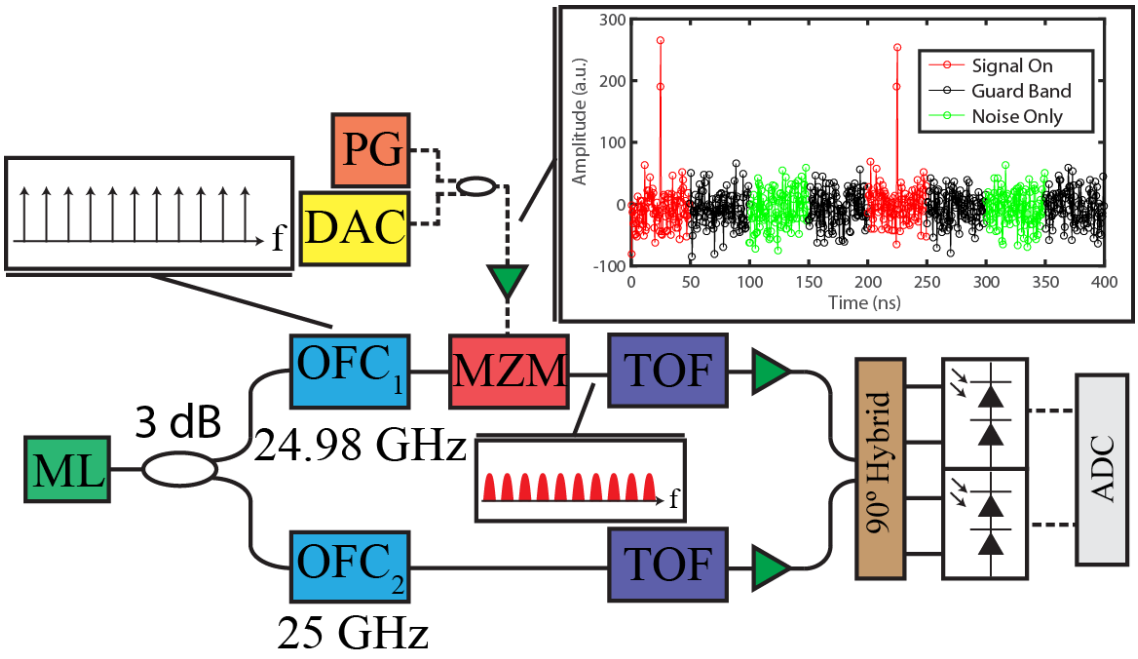

Figure 5.2 Experimental Setup. ML: Master laser, PG: Pattern generator, DAC: Digital-to-analog converter, MZM: Mach-Zehnder modulator, TOF: Tunable optical filter, ADC: Analog-to-digital converter. Figure inset shows a representation of the structure of the data uploaded to the pattern generator for characterization.

The optical signal carriers as well as the local oscillator carriers were generated by a cavity-less tunable OFC source [72] as described in Section 3.1. The highly coherent, high SNR combs were generated from a single master oscillator, operating at 1559.2 nm, which was split into two paths with a 3dB coupler. In the signal path, the seed was first amplitude modulated with an MZM using a 25 GHz electrical tone. The 25 GHz optical signal generated was then chirped using a phase modulator. Short, optical pulses were then generated in the first compression stage, consisting of single-mode fiber (SMF). Further pulse compression was achieved in a second stage, where chirping of the pulses was achieved with SPM in an HNLF. Subsequent pulse compression was then achieved in a second SMF stage. Next, the pulses were shaped,

and pedestals removed in a nonlinear optical loop mirror. Finally, the high peak power, pedestal free optical pulses were routed into the final HNLF stage of the comb generation process. The generated 25 GHz optical frequency comb consisted of over 300 optical modes, each with over 40 dB $OSNR_{0.1nm}$, limited by the measurement device. The generated 25 GHz comb is shown in **Error! Reference source not found.**. A similar comb generation technique was used to generate the 24.98 GHz pitched LO comb with a small offset (δf = 20 MHz).

The experimental setup is shown in Figure 5.2. The signal comb was modulated with the electrical input test signal using an MZM. Subsequently, the LO and modulated signal combs were routed into two separate programmable optical filters. The filters were used to emulate an AWG, and set to sweep through each of the signal and LO comb tones individually. The selected signal and LO modes were then optically amplified with a C- or L-band EDFA. The selected modes with 12 dBm and 9 dBm for signal and LO modes, respectively are then sent to a 40 GHz coherent detector. The output is captured by an ADC operating with 7 GHz bandwidth, 50 GS/s, and with 4.9 ENOB (measured under 23 GHz bandwidth). While such high bandwidths for the receiver and ADC are not necessary when a fully populated detector backplane is implemented, the excess bandwidth was used to achieve accurate timing alignment between each of the channels captured. Subsequently, the programmable optical filter is changed to select the next pair of signal and LO comb tones. DSP is applied after all 300 optical tones are captured with the ADC.

The electrical pulses used to test the system were generated by a 13 GHz wide pulse PG. The PG was used to synthesize 6 GHz wide electrical pulses and were set

with a repetition rate of 5 MHz. The low reprate of the pulses was chosen so that both the signal plus noise, and the noise only case could be simultaneously captured in a single measurement. Specifically, for a 50 ns ($1/\delta f$) time observation window, 4 observation windows occur between 2 electrical pulses, allowing for a signal plus noise measurement, and a noise only measurement, with a time domain guard band in between each, as depicted in the inset of Figure 5.2. Following the PG, 7 GHz wide electrical low pass filters were used to shape the pulses. In order to vary the SNR of the electrical pulses, synthetic white noise was generated using a 10 GS/s, 10-bit resolution DAC, triggered to the signal PG. The amplitude of the 6 GHz wide noise was controlled using a variable electrical attenuator. The synthetic noise generation, as opposed to analog noise generation, was specifically chosen so that repeated backplane measurements could be made using identical noise seeds. This allows for an emulated measurement of a 300 channel sub-rate receiver backplane, while utilizing only one sub-rate receiver that sweeps through all channels. The electrical pulses and noise were combined with an electrical coupler, amplified, and subsequently modulated onto optical modes of the signal comb using a null-biased MZM. Null bias was specifically chosen to minimize the amount of carrier beating between signal and LO tones.

The DSP applied involved first aligning any time shifts of each of the captured tones, and subsequently removing the random phase fluctuations using the frequency overlapping technique [86]. The captured channels were then filtered and downsampled to 20 MS/s. Each resulting complex vector corresponds to the amplitude and phase of the electrical signal at frequency f_k. The performance of the receiver is then characterized in two ways. First, the performance is measured in terms of SNR of each

of the 300 channels individually, corresponding to the performance one might expect from a low bandwidth integrating receiver. Next, to evaluate the performance of the proposed spectrally cloning and decomposition receiver, the time of arrival for each 50 ns window is first predicted using the maximum likelihood solution. The predicted linear phase is then removed, and the 300 resulting phasors are summed.

5.3 Discussion

The performance of the system was characterized with 6 GHz wide electrical pulses subject to varying noise levels. The noise power was controlled using a variable electrical attenuator and the SNR of the combined signal and noise was calibrated using

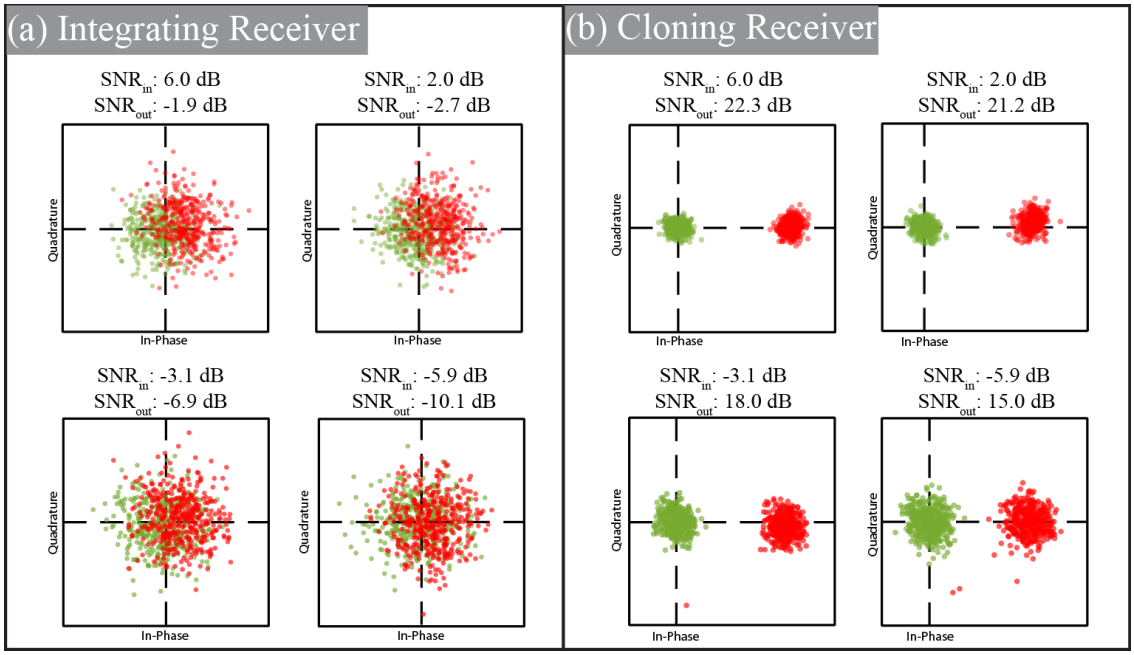

Figure 5.3 A 160 ps pulse is detected with varying noise levels by (a) an integrating receiver integrating over a 50 ns window, and (b) a 300 channel cloning receiver, each integrated over a 50 ns ($1/\delta f$) window and subsequently added. SNR_{in} is measured using an electrical spectrum analyzer over 20 MHz bandwidth, and SNR_{out} is measured based off the received clouds. Green dots indicate captures with only noise present, red dots indicate captures with signal present.

an electrical spectrum analyzer set to 20 MHz bandwidth. Each of the 300 channels captured were treated identically, with DSP applied to each 50 ns observation time window independently.

First, the average performance of the system was characterized by measuring the average SNR of each of the 300 captured tones. With a total capture time of 80 μs, 400 instances of the signal plus noise were captured, and 400 instances of the noise only case were captured. This generates two clouds in the complex field. The larger the separation from these clouds, the higher the confidence level of detection. The SNR in this case is defined as the mean value squared of the absolute value of the signal present cloud over the variance of the noise only cloud. The performance of the single channel

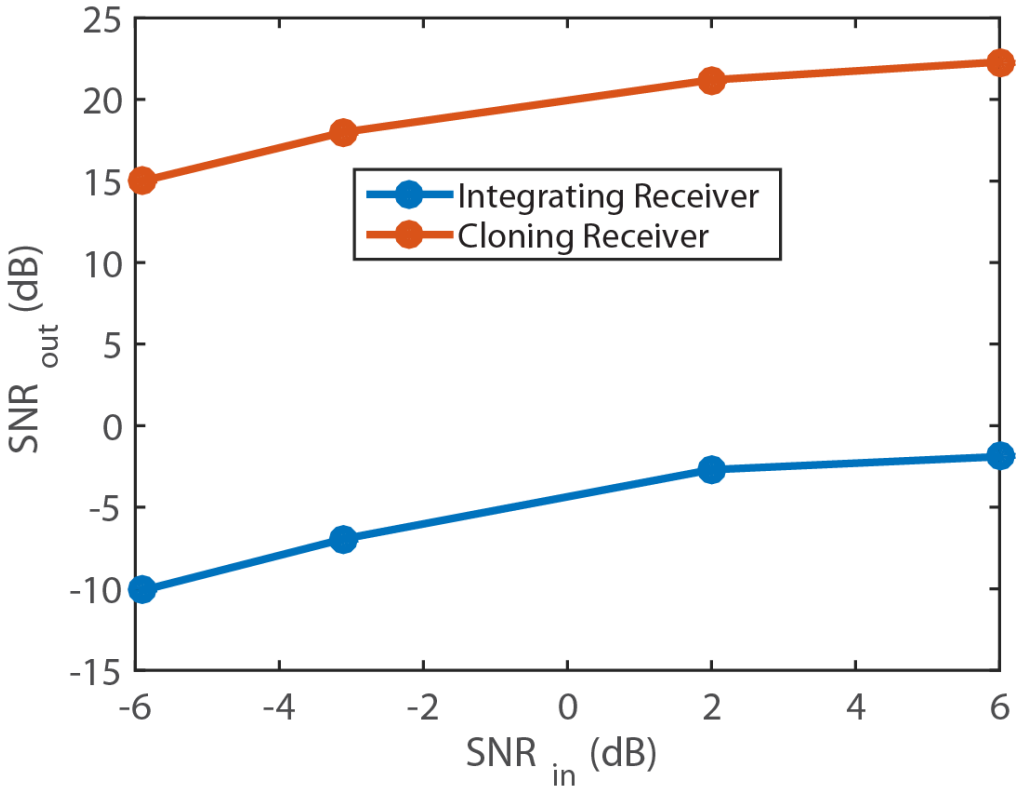

Figure 5.4 Performance results for the low bandwidth integrating receiver and the 300 spectrally cloning and decomposition receiver.

case is shown in Figure 5.3(a) for various input electrical SNR conditions. The single channel performance corresponds to an integrating receiver with 20 MHz bandwidth.

To measure the performance of the spectrally cloning and decomposition receiver, the linear phase associated with each of the captured 300 channels over a 50 ns window was first estimated and removed. The resulting 300 phasors were then summed together in the digital domain. The SNR was then measured the same way as the single channel case, by comparing the two generated clouds. The results are shown in Figure 5.3(b) for various input electrical SNR conditions. As can be seen, the spectral cloning and decomposition receiver yields clouds with much higher separation than that of the single channel case, indicating a considerably larger detection confidence for the spectrally cloning and decomposition receiver. Indeed, in all input SNR cases, a clear threshold can be drawn between the signal on and off clouds in Figure 5.3(b), but no such threshold exists for any of the figures in Figure 5.3(a) despite being under the same level of noise conditions. This demonstrates the clear advantage of the spectral cloning and decomposition receiver over a low bandwidth integrating receiver.

Figure 5.4 shows an overview of the performance results captured. Specifically, for SNRs in of -5.9, -3.1, and 2.0 dB, outputs of -10.1, -6.9, and -2.7 dB were achieved for the single receiver architecture, and an output of 15, 18, and 21.2 dB for the spectrally cloning, respectively. Indeed, a large SNR improvement is observed between the two detection techniques. The performance improvement between the single integrating receiver architecture and the spectrally cloning receiver are specifically plotted in Figure 5.5. Remarkably, the performance matches within 0.9 dB with the predicted theoretical gain of $10\times\log(300) = 24.8$ dB. These results, made possible by the

availability of tunable wideband optical frequency combs, validates the spectral cloning and decomposition technique as well as demonstrating the ability of this architecture to scale to even higher detection gains by increasing the number of spectral copies.

The proposed receiver was designed and tested for the reception of a single event, capable of increasing the detection sensitivity over 23.9 dB compared to a low bandwidth integrating receiver, even under varying noise power conditions. The characterization confirmed the remarkable performance of the system to detect subnoise single random events with high confidence. In fact, the receiver was characterized to increase the SNR of a –5.9 dB pulse to 15 dB SNR, allowing for high confidence detection of a subnoise random event. The enabling technology for this improvement is the introduction of wideband, low noise and distortion, tunable optical frequency combs. The ability to replicate a signal in a noise and distortion free manner is verified by the ability to average the signal spectrally, leading to the detection of single event signals with unprecedented confidence levels. Although the system is only characterized in terms of detection gains of coherent summation, the ability to replicate a single random event onto a large number of spectrally distinct copies leads to a low-latency, computation free Fourier processor.

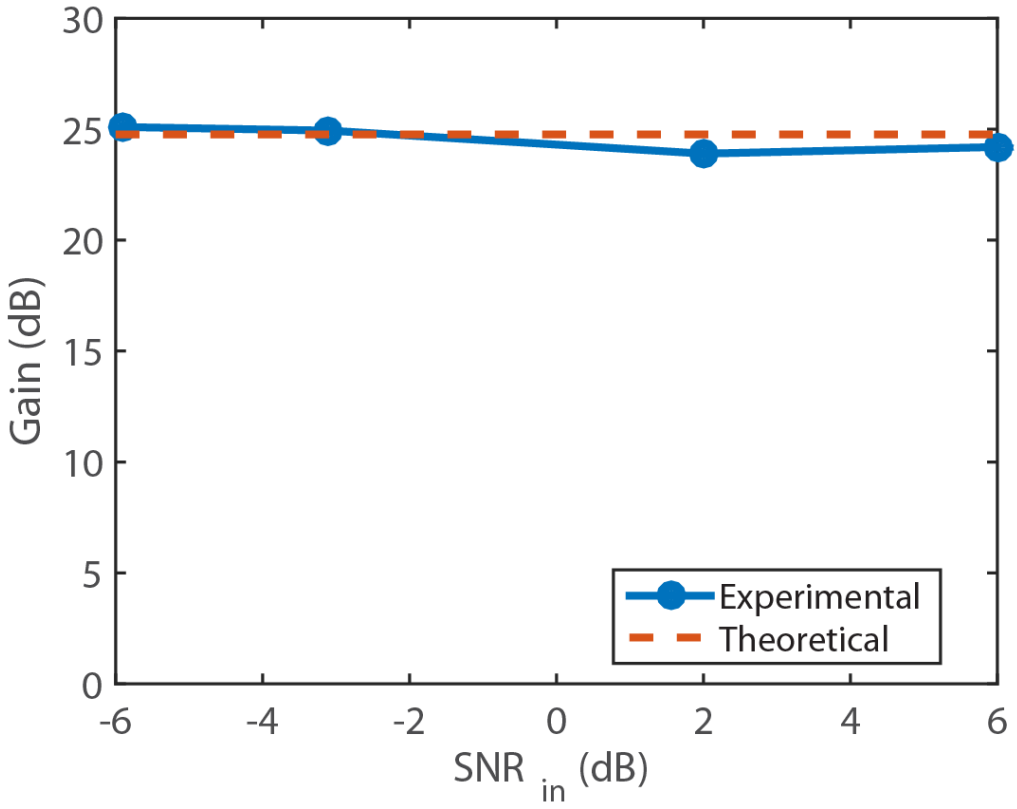

Figure 5.5 The measured gain between the two receivers under test and the expected theoretical gain.

Chapter 5, in part, is a reprint of the material as it appears in the IEEE/OSA Journal of Lightwave Technology, volume 34, issue 24, 5669-5674 (2016), titled "Detection of Fast Events in a Noisy Background" by Daniel Esman, Vahid Ataie, Bill P.-P. Kuo, Eduardo Temprana, Nikola Alic, and Stojan Radic. Chapter 5 also contains in part material submitted for publication as it may appear in the OSA conference proceedings, titled "Comb Assisted Subnoise Microwave Signal Detection," by Daniel J. Esman, Vahid Ataie, and Stojan Radic. The dissertation author was the primary investigator, and the primary author of these articles. Lastly, Chapter 5 in part is a reprint of the material as it appears in the Science Journal, volume 350, issue 6266, 1343-1346 (2015), titled "Subnoise detection of a fast random event" by Vahid Ataie, Daniel

Esman, Bill P.-P. Kuo, Nikola Alic, and Stojan Radic. The dissertation author was the primary investigator, and the co-primary author of this article.

Chapter 6 Comb Assisted Cyclostationary Analysis

The introduced dual OFC has already been demonstrated for many applications in previous chapters. However, each of these particular applications presented inherently assumes some knowledge of the signal. Specifically, in each of the presented applications in Section 4 assume that the carrier frequency and bandwidth of the signal are known. In instances where knowledge of the transmitter and the transmitted signal is completely unknown, an estimation of such parameters should be achieved first. One promising solution for estimating these parameters, even in high noise environments, is by using cyclostationary analysis as described in Section 2.2. To attain an accurate measurement of the desired signal parameters, a sufficient resolution in the spectral correlation function (SCF) should be used. This, unfortunately, is unfeasible for all electronic approaches as the frequency range of interest increases, as discussed in Section 2.2.

Recognizing the need for low complexity, high resolution cyclostationary analysis, as discussed in Section 2.2, the new dual OFC receiver was modified, with a specific goal of eliminating as much of the high-rate electronic front-end as possible. Similar to the previous approaches, the new architecture relies on the physical spectral decomposition of the wideband input signal, allowing for a relaxation in the required processing speed of the backplane electronics. Section 6.1 is dedicated to the principle of operation for the newly developed receiver. The experimental testbed is discussed in Section 6.2, with results and concluding remarks in Section 6.3.

6.1 Principle of Operation

Recognizing the fundamental limits imposed on both the ADC and FFT processing cores in a CS receiver, the new architecture eliminates both stages. Rather than digitizing a wideband signal and then computing its FFT in real time and at high precision, the received field is mapped to the Fourier domain in a computation-free manner, as shown in Figure 6.1. The new CS analyzer front end uses two coherently coupled frequency combs; the first one serves to replicate the received radiation, while the second one provides an array of LO tones, frequency-matched to each generated signal copy. The two combs possess a different frequency pitch, with the difference (δf) defining the frequency resolution of the physical Fourier preprocessor, and not necessarily that of the composite CS analyzer. In contrast to incoherent spectral analyzers, the received RF signal is used to modulate a frequency comb and create N spectral replicas, preserving both phase and amplitude. These copies are combined with a coherent LO comb, allowing each pair to be received by a low-bandwidth (δf) detector array. As a result, the backplane array outputs the DFT of the received field (denoted as $\tilde{r}[k]$, k=1,…,N in Figure 6.1). The tone-count of frequency combs directly controls the speed of the fastest electronic component in the processing chain.

As an illustration, 100 GHz CS analysis performed by combs with moderate (1500) tone count, dictates a 60 MHz-rate electronic backplane. Remarkably, a high-precision (ENOB > 10) ADC operating at this rate consumes approximately 0.2 mW [13], in sharp contrast to a full-band (100 GHz) device. More importantly, an FFT processor is entirely eliminated, thus resolving one of the most important technological limitations of a wideband CS analyzer.

The use of near-noiseless and distortion-free signal replication and subsequent frequency decomposition are unique attributes of the new cyclostationary receiver, as illustrated in Figure 6.1. First, the received electrical signal is replicated onto a coarsely

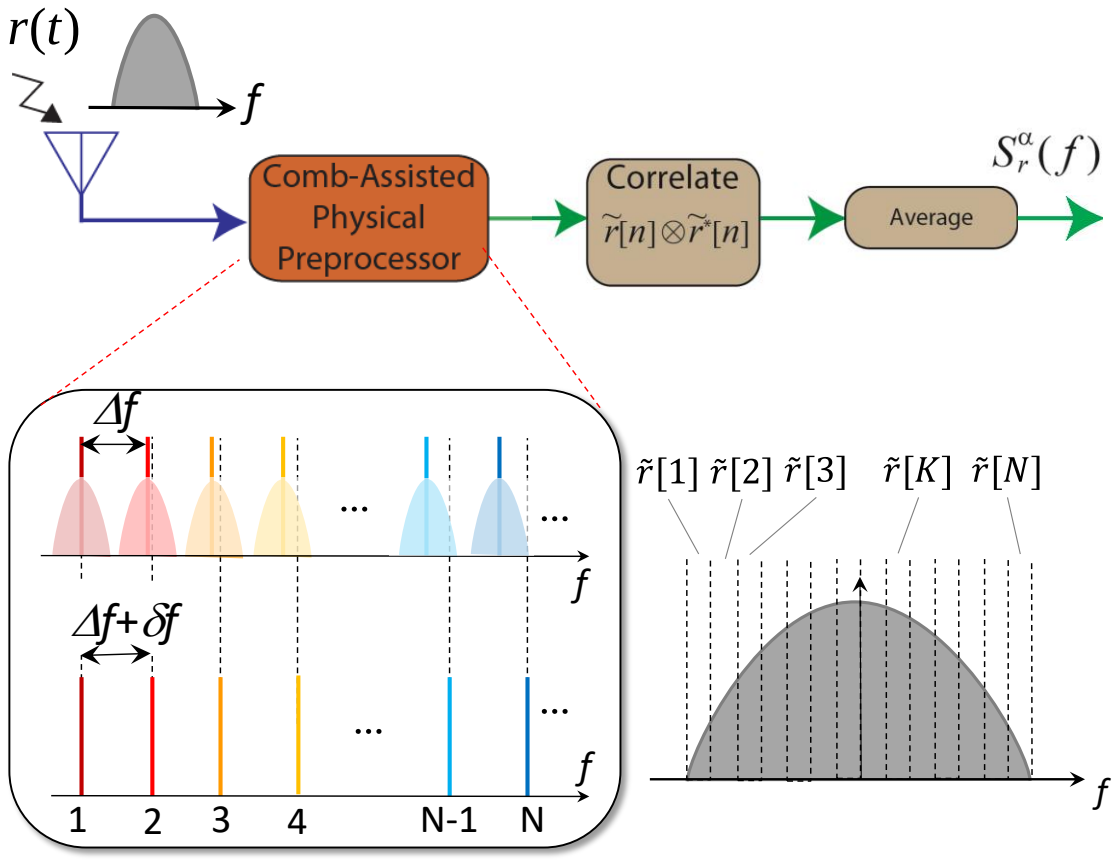

Figure 6.1 Comb-Assisted CS analyzer architecture: mutually coherent combs with precisely controlled frequency pitch eliminate ADC-FFT processing chain. Local oscillator comb probes signal at different frequencies, resulting in coherent band segmentation (right bottom).

spaced (ΔF) optical frequency grid. This is achieved by modulating the received electrical signal onto an optical frequency comb (signal frequency comb). A second, Vernier comb, referenced to the signal comb with a pitch offset δf from ΔF is generated. The two combs were frequency locked by sharing the same master optical oscillator as a seed, and frequency-locked RF synthesizers. Each comb is then sent to unique AWG, which splits each optical mode into individual fibers. Finally, each of the overlapping comb tones is sent to a low speed coherent receiver. The selected Vernier comb line acts as a frequency-referenced local oscillator for a specific sub-band of the electrical signal, effectively down-converting the designated frequency band to baseband. The down-converted electrical frequency components are then captured by the low speed receiver. Consequently, the input electrical spectrum is completely decimated, akin to a lossless, but coherent channelization. It should be noted that the architecture, while resembling the conventional channelizer, does not have any physical filters, and, more importantly, does not operate on signal spectral power, but on the entire received field. In this respect, the preprocessor is more similar to the vector analyzer, except that it can operate in real time, without any blind intervals.

The resolution at which the frequency decomposition can be achieved is directly proportional to the number of optical frequency comb modes that are utilized. In the simplest implementation, high resolution is achieved by incorporating maximal number of optical frequency modes. Although it is possible to drastically reduce the number of comb tones and corresponding sub-rate detector elements while maintaining the same resolution, this was not done in this report.

A literal implementation of a comb-assisted CS architecture calls for each signal-LO pair created by the modes from the signal and reference comb to be routed by an AWG and subsequently to a bank of low speed coherent detectors. Each detector would yield a single spectral decomposition element of the received electrical field. However, to demonstrate the scalability of this architecture without fully populating the low speed detector backplane, the performance of the receiver can be rigorously characterized with a single low speed receiver. The use of a single receiver in capturing multiple channels is a well-established technique in WDM transmission, where the performance of each channel is measured sequentially at the end of the link. Applying the equivalent to WDM sequential approach, a single, low speed coherent receiver is used to successively capture each of the signal and LO modes individually. For an accurate emulation of the full-scale implementation, the received electrical noise has to be repeated during each of the successive captures. Consequently, the noise was generated in the digital domain and added to the electrical signal before being converted to the analog domain with a DAC. However, this technique, while relieving the construction from assembling the full detector array, also imposes a unique challenge in the characterization of the receiver. Firstly, the noise statistics and bandwidth will be set by the resolution and bandwidth of the DAC, respectively. Consequently, it is necessary to use a DAC with a high bandwidth and sufficient ENOB to synthesize adequate noise statistics during the characterization of the CS receiver. Secondly, the sequential signal capture imposes a unique stability challenge during the characterization of the receiver: the entire receiver, and in particular, the two optical frequency combs must remain stable during the entire capture time. To appreciate this

requirement, it should be noted that a typical signal of interest lasts nanoseconds; in contrast, sequential CS capture can last hours. This limitation is substantially mitigated by the fact that frequency-referenced combs have been derived from a single (fixed) frequency source and that no stabilized optical cavity was used anywhere in the testbed. As a result, all results reported here were easily replicable, both over short scale (minutes) and long scale (hours). This feature has particular importance in case when the entire CS analyzer must operate in harsh (airborne or space borne) environments subject to stress and temperature variation. Intuitively, the observed stability is rooted to a simple fact that two frequency combs, while drifting in frequency over time (master oscillator was not locked), they do so together, strictly maintaining their relative frequency/phase relations.

Finally, after spectral decomposition, the SCF is estimated by taking the vector outer product of the physically generated DFT components with the conjugate of itself. The entire process is repeated and averaged over time, varied with different signal stimuli.

6.2 Experimental Demonstration

The experimental comb generation technique is depicted in Figure 3.2. A single high quality master laser (ML) oscillator operating at 1559.2 nm was used as a seed to both optical frequency combs. The ML was split into two paths with a 3-dB coupler. The signal path was defined by a 25 GHz-pitched optical frequency comb. To generate a high SNR optical frequency comb, broadband optical pulses were first synthesized using the master oscillator as a carrier and a conventional MZM driven with an RF 25

GHz tone. The pulses were subsequently tailored in the first compression stage, first by inducing a chirp with a PM, driven with identical RF 25 GHz tone, and subsequently compressed within a section of single mode fiber (SMF). After amplification and filtering, the optical pulses were then shortened in a second compression stage. The chirp in the second compression stage was generated by SPM in an HNLF, with subsequent compression achieved in a 2nd section of SMF. Next, the pulses were precisely shaped in a NOLM architecture. Finally, the high peak power, pedestal-free pulses were launched into the final HNLF stage, where cascaded FWM was used to generate a wideband optical frequency comb with 25 GHz spacing. The generated comb is shown in **Error! Reference source not found.** and consisted of over 400 optical modes, with minimum of 43 dB $SNR_{0.1nm}$. It should be noted that OSNR was limited by the measurement device sensitivity; true OSNR was likely higher. A similar

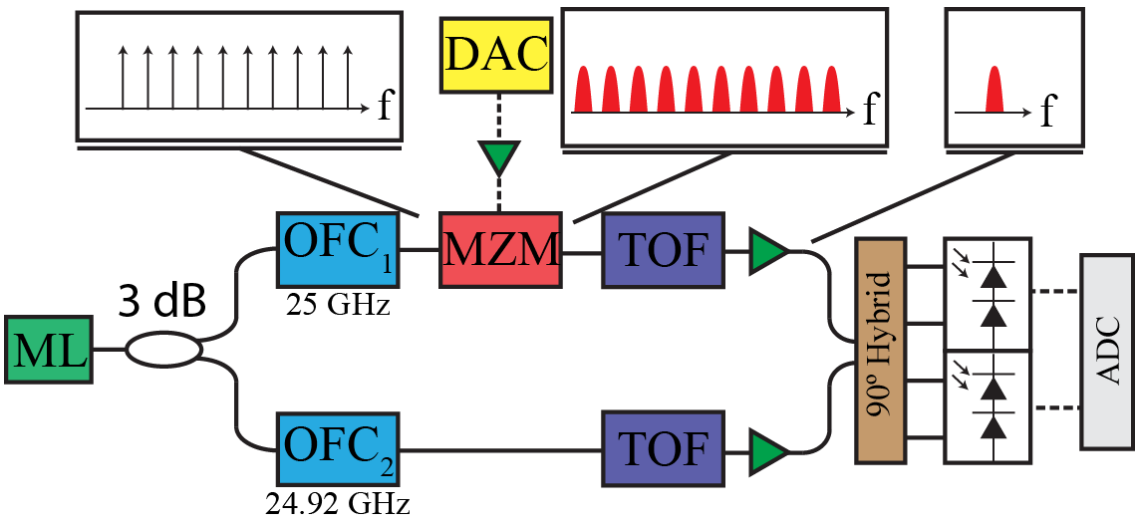

Figure 6.2 Experimental Setup. ML: Master laser, MZM: Mach-Zehnder modulator, DAC: Digital-to-analog converter, TOF: Tunable optical filter, ADC: Analog-to-digital converter.

technique was used to generate a second (reference) comb, using a 24.92 GHz RF seed to generate the desired δf = 80 MHz pitch difference between the two combs.

The experimental CS setup is shown in Figure 6.2. After the comb generation, the signal comb was modulated by the electrical input test signal. This effectively replicated the incoming electrical signal onto each of the 250 optical carriers. Next, both optical frequency combs were sent to two separate programmable optical filters. The filters were used to emulate an AWG, whereby each optical mode was sequentially filtered out individually. The pair of overlapping signal and reference comb tones were

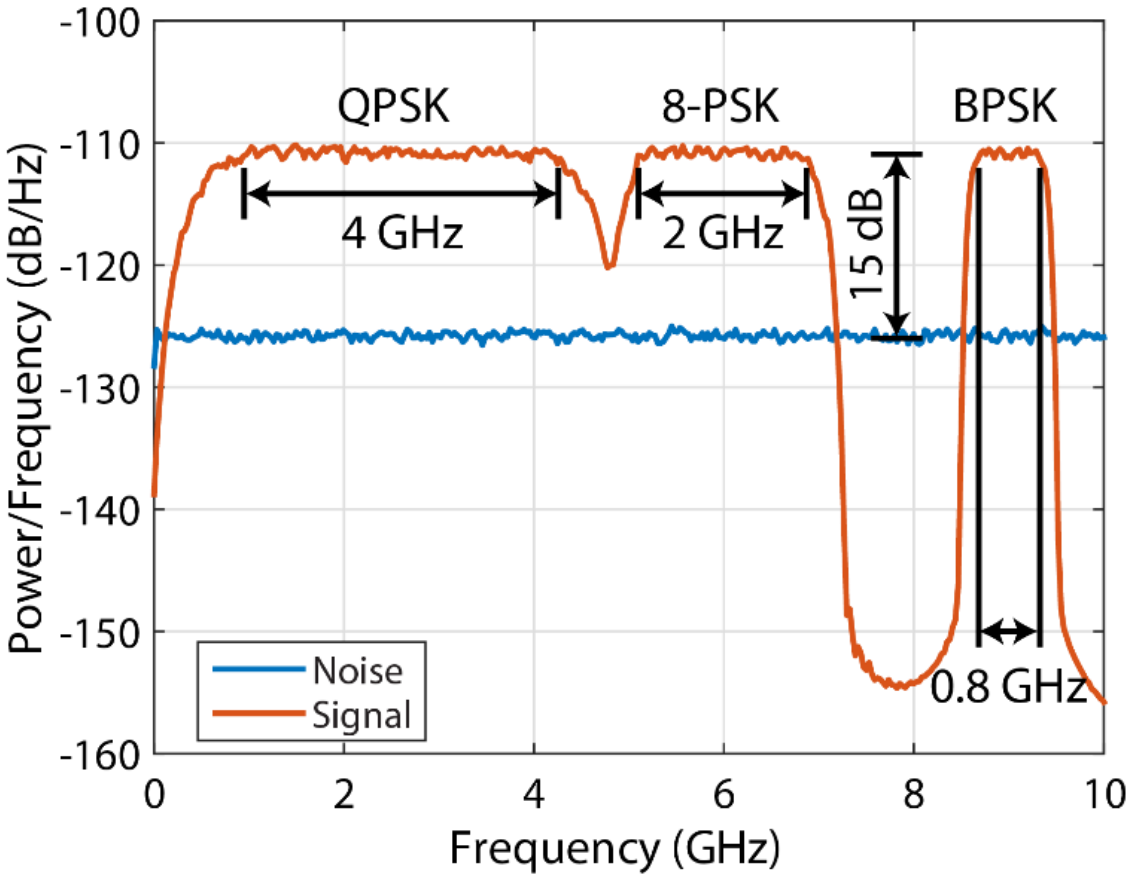

Figure 6.3 Electrical 15 dB SNR input Spectrum consisting of 4 GHz QPSK signal at 2.5 GHz carrier frequency, 2 GHz 8-PSK signal at 6 GHz carrier frequency, and 800 MHz BPSK signal at 9 GHz carrier frequency.

then amplified with either C- or L- band EDFA before being sent to a 40 GHz hybrid detector. The output was then sent to an electrical ADC whose bandwidth and sampling rate were set to 80 MHz. After the capture, the programmable optical filter was then tuned to select the next pair of overlapping optical tones. Finally, post-processing was applied after all 250 optical modes were captured by the ADC.

The electrical test signal was generated using a 60 GS/s DAC. The DAC was used to synthesize both the signal and noise. The signal consisted of 4 GHz quadrature phase shift keyed (QPSK) raised cosine shaped data with 0.25 rolloff factor and upconverted to 2.5 GHz carrier. Additionally, a 2 GHz wide, 8-PSK raised cosine shaped signal and an 800 MHz BPSK raised cosine shaped signal were also generated and upconverted to 6 GHz, and 9 GHz, respectively. The three signals were simultaneously stimulated with noise to achieve an in-band SNR of 15 dB, 10 dB, and 5 dB. The digital signal stimuli and noise spectrum are illustrated in Figure 6.3. The generated electrical signal was then amplified and used to modulate the 25 GHz signal comb utilizing a null-biased MZM.

The DSP that was applied at the receiver consisted of channel timing and phase alignment, filtering and subsequent downsampling to 80 MHz in order to estimate the 250 DFT coefficients over a 12.5 ns window. The SCF function was then calculated by taking the vector outer product of the estimated DFT coefficients with the conjugate of itself. The process was repeated and averaged over an approximately 4.2 μs time window, corresponding to 333 total averages. The number of averages was limited by the total memory depth of the DAC utilized.

6.3 Discussion

To test the performance of the new analyzer architecture, the SCF was calculated in two ways. First, the SCF was simulated in the digital domain, computing the 250 point DFT, and subsequently yielding the SCF estimation. The estimation was reached by averaging 333 realizations of the SCF of the input electrical signal. Secondly, the electrical signal was then sent into the cyclostationary receiver whereby the 250 DFT coefficients were estimated using the new architecture, and the SCF

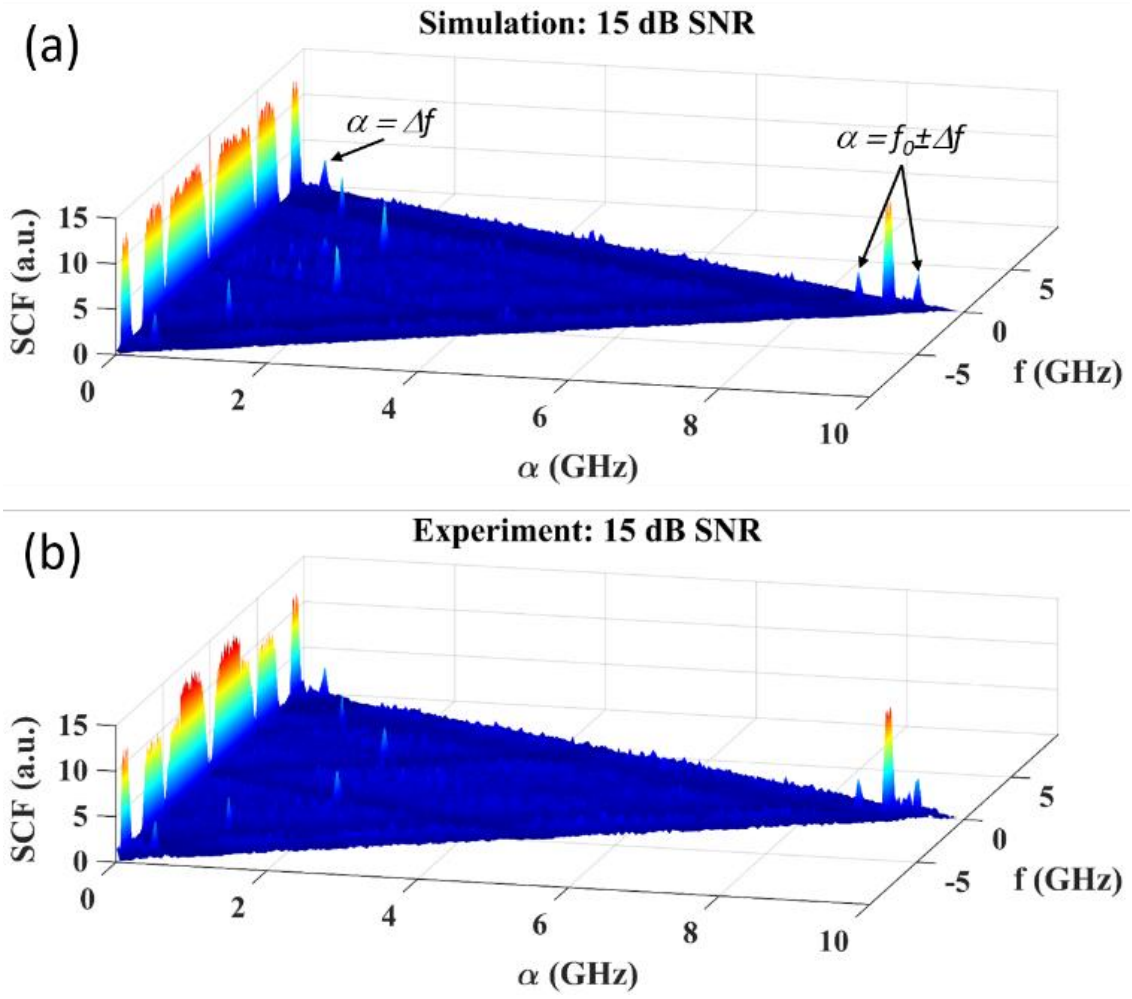

Figure 6.4 (a) Simulated SCF results with 250 point DFT and 15 dB SNR. BPSK features at Δf and $f_0 \pm \Delta f$ are distinguished. (b) Measured experimental SCF results with 250 point DFT and 15 dB SNR.

estimation was then reached by averaging 333 realizations of the SCF. The estimated SCF was then compared with the simulated SCF. The simulated SCF and experimental SCF for an input SNR of 15 dB is shown in Figure 6.4(a) and (b), respectively. In both plots, distinct features appear in the α-f domain, as expected from the QPSK, 8-PSK, and BPSK modulated signals. It should be noted that simulated and experimental results match extremely well, both with respect to feature extraction and overall magnitudes. Indeed, for a BPSK signal, strong spectral correlation exists at the carrier frequency rate $\alpha = f_0$, at the modulation rates $\alpha = \pm\Delta f$, and at $\alpha = f_0 \pm \Delta f$ [90], as indicated in Figure 6.4(a) and (b). For QPSK and 8-PSK, strong spectral correlation does not exist at the carrier frequency, due to the modulation being balanced between in-phase and quadrature components [90]. In both the simulated and experimental data, strong spectral correlation for QPSK and 8-PSK is indeed only observed at the keying rates $\alpha = \pm\Delta f$, as depicted in Figure 6.4(a) and (b).

The proposed system was also characterized in lower SNR regimes. This was achieved by increasing the noise power relative to the signal in the digital domain before uploading the data to the DAC. For an input SNR of 10 dB, the simulated and experimentally estimated SCF are plotted in Figure 6.5(a) and (b), respectively. Even at this lower input SNR, both the simulated and the computationally efficient experimental SCF exhibit strong features in the cyclic domain. Also, even in the lower SNR regime, the experimental data matches closely with the simulated data, with

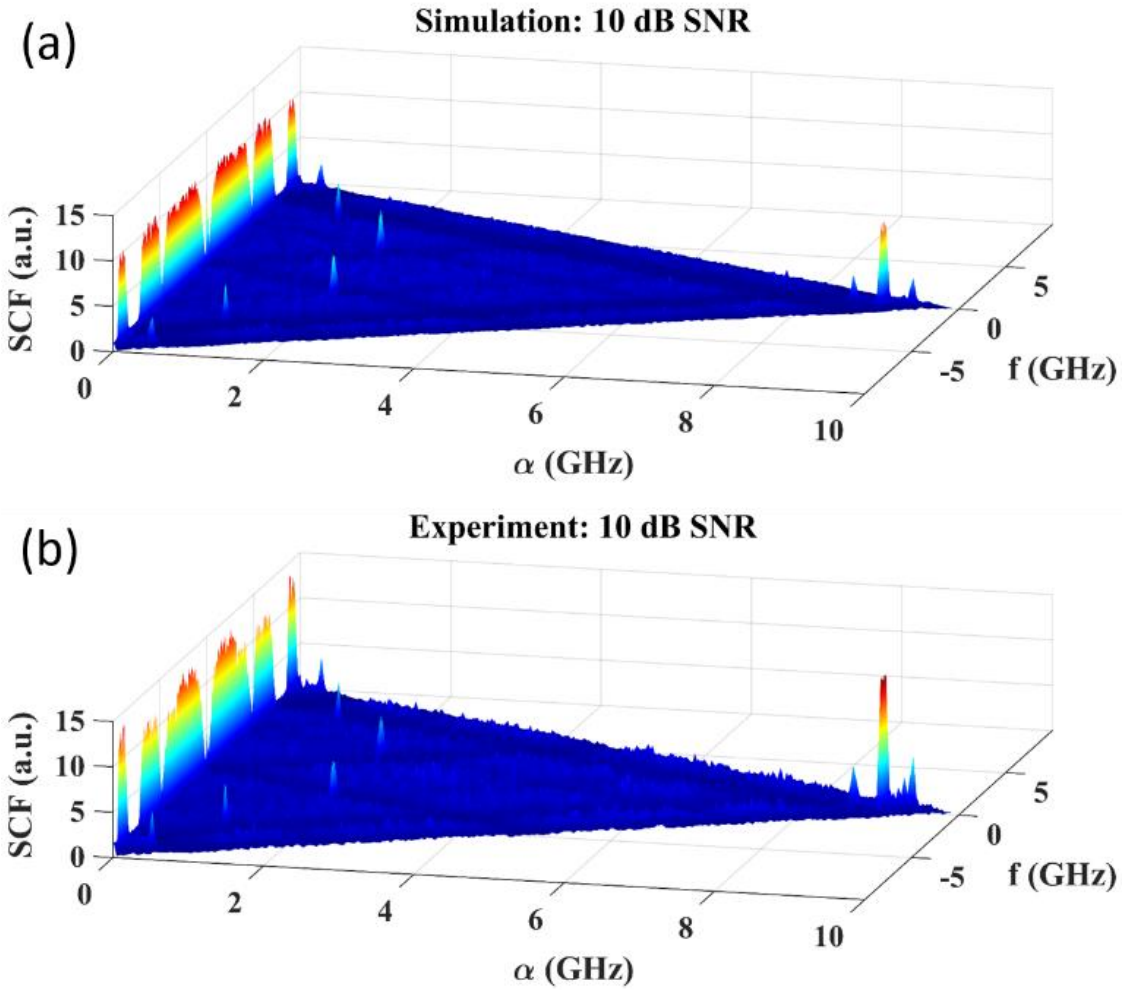

Figure 6.5 (a) Simulated SCF results with 250 point DFT and 10 dB SNR. (b) Measured experimental SCF results with 250 point DFT and 10 dB SNR.

features that match well with the analytic expectation. Remarkably, the system SNR was lowered to 5 dB, maintaining the similar agreement between the simulation and experiment. Even in this low SNR regime, the simulated SCF matched closely with the low complexity experimental SCF, as shown in Figure 6.6(a) and (b). In both cases, strong spectral correlation peaks are observed in the cyclic domain that match the theoretically predicted features. Specifically, for an environment with large interfering noise, where the signal is only 5 dB above the noise, high confidence signal detection

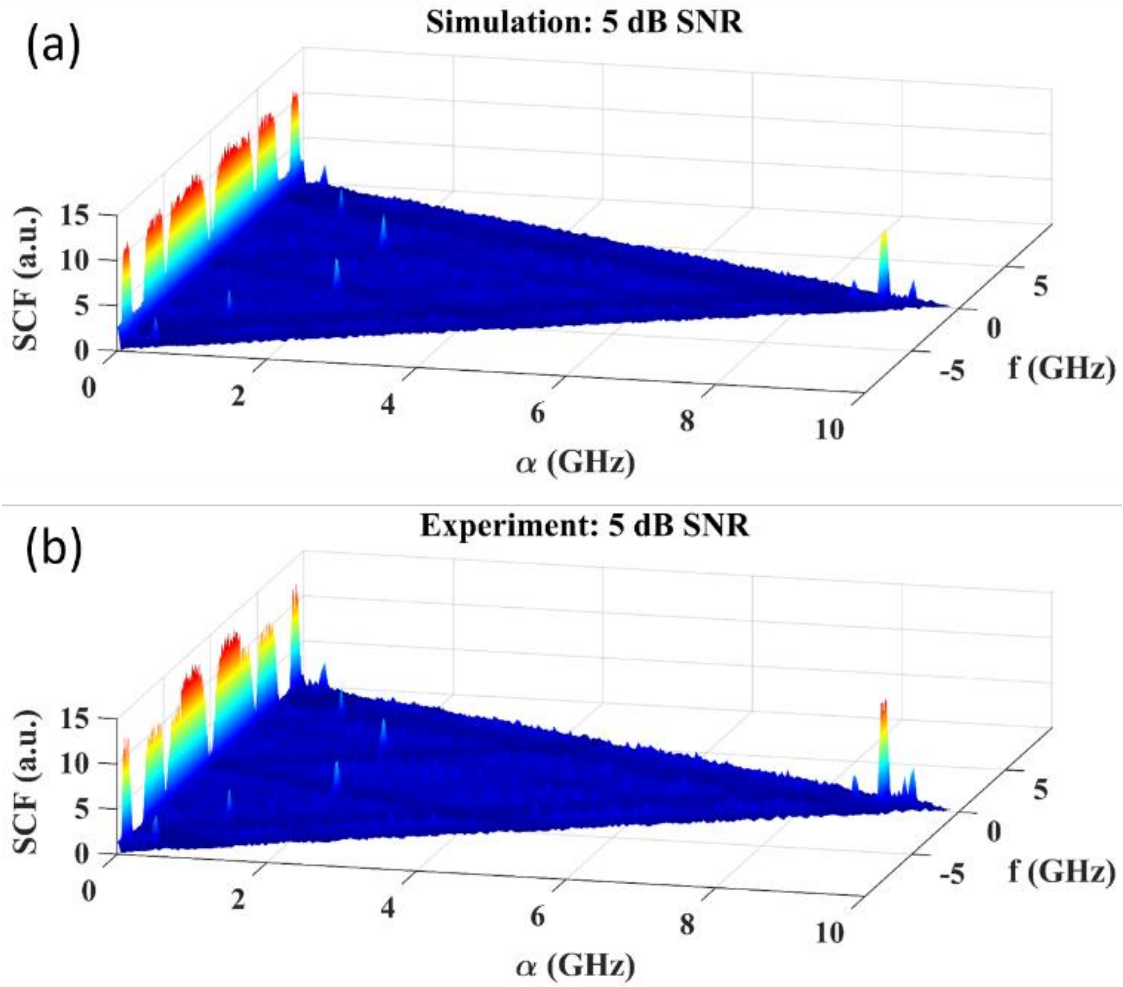

Figure 6.6 (a) Simulated SCF results with 250 point DFT and 5 dB SNR. (b) Measured experimental SCF results with 250 point DFT and 5 dB SNR.

and classification can be achieved with low computational complexity utilizing the new experimental architecture.

Finally, to demonstrate the practical utility of the new approach, a CS receiver was designed, constructed and packaged within a standard telecommunication module, as shown in Figure 6.7(a). This portable system operated over 16 GHz bandwidth with

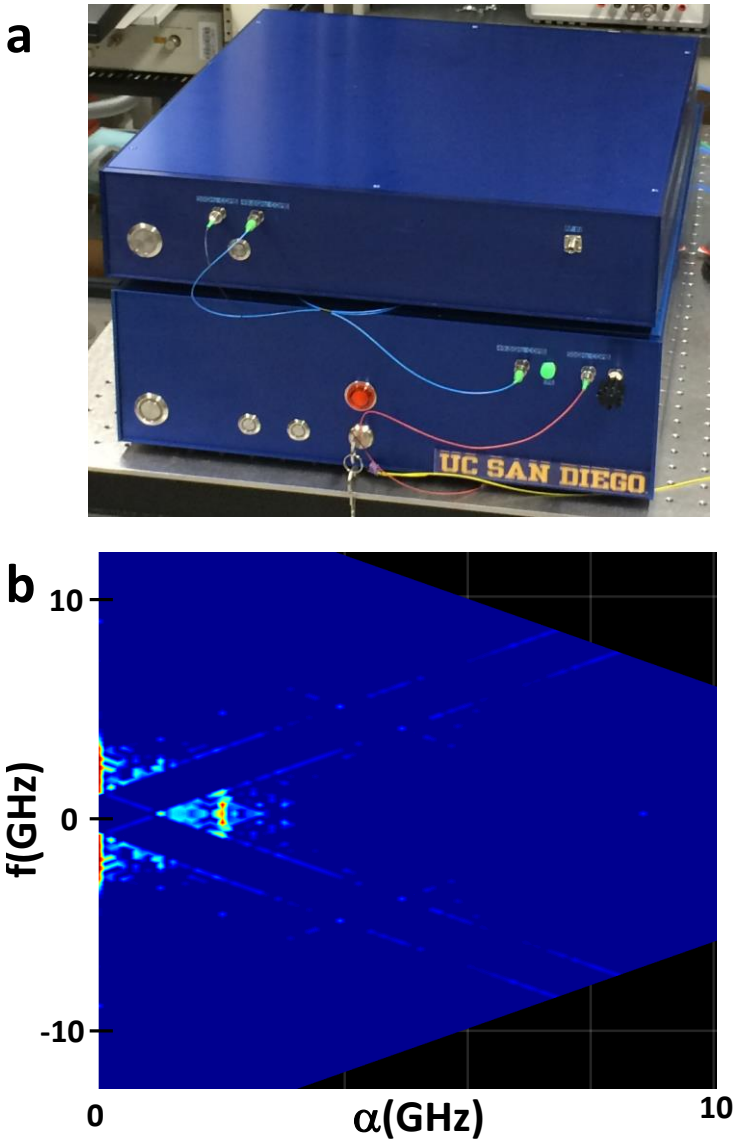

Figure 6.7 (a) Packaged CS Analyzer consisting of two mutually coherent optical frequency combs (lower box), and receiver backplane for electrical input modulation and CS analysis (upper box). (b) SCF output generated by 2 GHz BPSK signal stimulus at a 2 GHz carrier frequency.

200 MHz spectral resolution. To validate the packaged receiver performance, a 2 GHz BPSK signal up-converted to 2 GHz carrier frequency was used as a stimulus to the system. The output of the system which calculates the SCF function of the input is plotted in Figure 6.7(b).

The proposed ultrawideband cyclostationary receiver was designed, constructed and tested for the first time, eliminating the need for full-band digitization and real-time Fourier computation. The low complexity of the new wideband receiver was made possible by generating a Fourier representation in the physical domain. The received field was decimated in the spectral domain using tunable, coherently coupled frequency combs that were derived from a single master oscillator. The new receiver was used to generate the SCF of multiple RF signal stimuli, and under varied SNR conditions. While this demonstration used only 250 comb tones to demonstrate the feasibility of computation-free Fourier mapping in a CS receiver, it should be recognized that parametric combs operating with thousands of tones allow for considerably higher performance, both with respect to spectral resolution and signal selectivity. It should be expected that the new architecture evolves into different topologies that will optimize between the need to fully populate the receiver backplane and a need for low-latency operation.

Chapter 6, in part or in full is currently being prepared for submission for publication of the material by Daniel. J. Esman, Vahid Ataie, Bill P.-P. Kuo, Eduardo Temprana, Nikola Alic and Stojan Radic. The dissertation author was the primary investigator, and the primary author of this article.

Chapter 7 Conclusion

Owing to the exponential growth in data traffic, the amount of data transmitted in any given frequency channel has increased drastically. This has caused a drought in the available radio frequency (RF) spectrum and pushed these frequency channels to much higher frequencies to avoid interference with other users. This dissertation's contribution to this issue is two-fold. First, a novel solution to the drought in the available RF spectrum is introduced, allowing for secure, regulation free communication over the entire RF range without interfering with other users in the same frequency channels. Secondly, in order to blindly capture the data channels that are being pushed to higher and higher frequencies, a receiver is designed to capture these high frequencies and simultaneously process and classify them.

The tunable parametric optical frequency comb (OFC) is the cornerstone of this thesis, allowing for an all optical receiver and processing scheme. Correspondingly, the theoretical background of the parametric process, specifically four wave mixing (FWM), is introduced in Chapter 3. This theoretical background allows for the introduction of generating an OFC using the parametric process, with the unique advantage over other OFC generation techniques of possessing agile frequency configurability. The generation of a frequency tunable OFC allowed for the generation of two optical frequency combs with a precise frequency pitch offset.

The first application of the dual OFC receiver was proposed in Chapter 4, allowing for the simultaneous capturing and demodulation of a transmitted coded signal. Two receiver schemes for the reception of a direct sequence spread spectrum

(DSSS) channel were presented in this chapter. The first scheme showed the ability of the dual OFC to both synchronize and demodulate a spread spectrum channel with 23 dB processing gain. The main limitation of the scheme was also discussed, indicating that such a scheme could not capture a DSSS channel with ultra-high spreading rates. The receiver was then modified to use the dual OFC receiver as a synchronization tool only, and subsequent demodulation in an all-analog-electronic approach. This proposed receiver was shown to generate nearly 40 dB of processing gain. Finally, the dual OFC receiver was shown to have the ability to demodulate and capture a frequency hopping (FH) pulse position modulation (PPM) signal. The receiver was characterized for various data rates and a FH signal.

In Chapter 5, a new application of the dual OFC receiver was proposed to detect a single transient event buried in noise. The scheme exploits the fact that a signal and noise field inherently have completely different statistics. Specifically, the signal possesses frequency correlated statistics, while the noise does not, allowing for an averaging of the frequency components to increase the confidence in detection. To exploit this fact, the proposed receiver discussed in this chapter uses the OFC to replicate the signal without any loss or amplification, as would be required with conventional replication techniques. The dual OFC receiver was shown to increase the detection confidence of a 6 GHz wide transient signal by over 24 dB.

The last part of this dissertation, presented in Chapter 6, was dedicated to the detection, classification and interpretation (DCI) of unknown received signals. To do this, high resolution cyclostationary analysis was performed to compute the spectral correlation function (SCF). The use of cyclostationary analysis, while computationally

expensive, provides the ability to detect various attributes of a signal, including its modulation type, modulation rate, carrier frequency and bandwidth. To reduce the inherent computational complexity, the dual OFC receiver was used to remove two of the major bottlenecks of conventional cyclostationary analysis, the analog to digital converter (ADC) and the discrete (or fast) Fourier transform (DFT). The proposed receiver was demonstrated to simultaneously detect and classify various modulation types and rates even when the signal to noise ratio (SNR) was reduced to 5 dB.

7.1 Future Directions

Although this dissertation goes into depth to the many applications and theory of the proposed dual OFC receiver, many open questions still remain for the introduced applications. The sections that follow discuss the possible future directions for each of the proposed applications.

7.1.1 Comb Assisted Spread Spectrum Receiver Enhancements

One topic that is introduced in Section 4.1.2 is the recipe for the channel selection function. While the channel selection function used in Section 4.1 and Section 4.2 is referred to as ideal, there may be a more suitable channel selection function. Specifically, a truly ideal channel selection function will take into consideration both the sparsity of the selection as well as the SNR of each of the coefficients, instead of one or the other. The recipe to yield this truly ideal channel selection function is still unknown at this time and a possible research topic to increase the performance of the synchronization scheme.

Another further step for the proposed DSSS scheme is combining both the synchronization and demodulation schemes. This thesis describes the performance of each of the schemes independently, but a truly autonomous receiver will need to have both schemes coupled together and running simultaneously. Such a receiver will also need to perform clock recovery before demodulation, introducing yet another challenge. Finally, in order for this receiver to truly become ubiquitous, the size, weight, and power of the device should be greatly reduced. To do this, both of the OFCs, the arrayed waveguide grating, and the subsequent detector array should all be integrated onto a photonic integrated circuit to allow for such a device to become portable to a handheld wireless device.

7.1.2 Pulse Position Modulation Receiver: Noise Reduction

The main limitation of the proposed dual OFC receiver in its applicability to detect a FH-PPM signal is the received SNR. Currently, the received SNR is limited by the shift and subtract method used. As a future direction, this limit could be resolved in one of two ways. First, the receiver count could be increased so that the shift and subtract method would not be necessary to implement. As a result, the limited received SNR would be greatly increased since each of the received DFT coefficients would be sent to its own individual detector. However, increasing the total detector count will also increase the complexity and power consumption of the receiver. To avoid this, the shift and subtract method performance can be improved. If achieved, the total number of receivers would remain much lower than the total number of received DFT coefficients. Such a case would be a huge advantage to every receiver design proposed

in this dissertation, allowing for a largely reduced number of receivers in the backplane while maintaining a large number of DFT coefficients.

The shift and subtract method used in Section 4.3 can be understood in simpler terms:

$$k_N = \sum_{n=1}^{N} a_n c_n \tag{7.1}$$

$$k_{N+1} = \sum_{n=1}^{N+1} a_n c_n \tag{7.2}$$

where k_N is the output of a detector at frequency component *N*, c_n is the sought after DFT coefficients and a_n is a scaling constant on each of the coefficients. In Section 4.3, the scaling constants a_n are assumed to be equal to one. With this assumption, it is clear to see that $c_{N+1} = k_{N+1} - k_N$. However, the assumption that $a_n = 1 \; \forall n$ is not correct and may be the main limitation of the results from Section 4.3. Indeed, the scaling coefficient a_n is altered as a result of the power difference of each mode of the OFC, as well as the receiver responsivity difference per optical frequency. In practice, the value of a_n could be calibrated by measuring the receiver responsivity, and comb tooth power, and applying the appropriate scaling to Eq. 7.1 and Eq. 7.2. This should greatly increase the performance of the shift and subtract method and allow for an increase in the received SNR.

7.1.3 Transient Signal Detection: Generalization

The scheme presented in Chapter 5 provides a great means of increasing the detection confidence of a transform limited single transient event. However, the

assumption of a transform limited signal, and the assumption of a single event limits the applicability of the proposed scheme. Indeed, naturally occurring transient events may not possess these attributes. Even synthetic signals can possess a chirp, or may include a fine structured waveform. As a result, a future direction for the scheme introduced in Chapter 5 could be to process much more difficult waveforms. In the easiest case, if the waveform is known a priori, the amplitude and phase of each of the coefficients could be modified accordingly to achieve coherent phasor summation as described in Section 5.1.

A much more challenging and interesting case is when the waveform is completely unknown a priori. This case could be solved in one of two ways. First, if the SNR of the received signal is known to be high, the amplitude and phase of the received coefficients could be measured directly. The coefficients could then be determined to be either from background noise or a signal of interest. If the SNR cannot be assumed to be high, then a different approach needs to be taken. In this case, a bank of possible waveform DFT coefficients could be stored. Then, after the received DFT coefficients are measured, the amplitude and phase of the DFT coefficients from one of potential waveforms in the bank could be removed before subsequent addition. This would then be repeated for each of the possible waveforms in the bank. If the received DFT coefficients came from a similar waveform that is in the bank, this will lead to coherent phasor summation as described in Section 5.1. Unfortunately, this approach does require more digital processing and introduces latency.

7.1.4 Cyclostationary Analyzer: Resolution Enhancement

The results from the proposed scheme in Chapter 6 provide a great means for performing DCI on incoming electrical signals. However, the resolution of the spectral correlation function is limited in Chapter 6 to 80 MHz. One future direction for this scheme is to improve the resolution to capture much slower signals. This can be done directly by reducing the comb pitch difference and simultaneously increasing the total number of comb tones used to cover the same bandwidth. However, this also comes with the penalty that the total number of required receivers in the backplane also increases. To avoid this penalty, a similar approach to Section 4.3 could be used whereby multiple DFT coefficients could be sent to a single coherent receiver, and extracted later in the digital domain. This, too, would come with a penalty from the shift and subtract method. However, if the shift and subtract method could be improved as described in Section 7.1.2, this would be a viable solution to greatly enhancing the resolution of the receiver.

Another improvement in the receiver design presented in Chapter 6 is to reduce the computational complexity even further. Indeed, the approach presented in this dissertation requires that the spectral correlation be computed in the digital domain. This computation is quite expensive and is proportional to N^2 where N is the length of the DFT. However, this computation is only a multiplication of DFT coefficients, which could be achieved in the analog domain.

Finally, the results from Chapter 6 could be extended to a new application. Specifically, if the proposed DSSS method to solve the available spectral drought as proposed in Section 4.1 and Section 4.2 come to fruition, the security of the DSSS

scheme could be potentially compromised by using cyclostationary analysis as a method to estimate the coding word. Specifically, each unique codeword will manifest itself as a unique feature in the spectral correlation function. As a result, if the spectral correlation function could be measured with high accuracy as proposed in Chapter 6, the codeword could potentially be measured, allowing to demodulate the original transmitted data without a priori knowledge of the codeword.

Chapter 8 Bibliography

[1] G. H. Forman and J. Zahorian, "The Challenges of mobile computing," *IEEE Computer,* vol. 27, pp. 38-47, 1994.

[2] I. Ferrain, C. A. Colinge and J.-P. Colinge, "Multigate transistors as the future of classical metal-oxide-semiconductor field-effect transistors," *Nature,* vol. 479, no. 7373, pp. 310-316, 2011.

[3] J. Alden, "Exploring the Value and Economic Valuation of Spectrum. ITU reports on broadband," April 2012. [Online]. Available: http://www.itu.int/ITU-D/treg/broadband/ITU-BB-Reports_SpectrumValue.pdf. [Accessed 9 January 2017].

[4] R. N. Clarke, "Expanding mobile wireless capacity: The challenges presented by technology and economics," *Telecommunications Policy,* vol. 38, no. 38, pp. 693-708, 2014.

[5] C. L. Jackson, "The allocation of the radio spectrum," *Scientific American,* vol. 242, no. 2, pp. 34-39, 1980.

[6] M. Hilbert and P. Lopez, "The world's technological capacity to store, communicate, and compute information," *Science,* vol. 332, no. 6025, pp. 60-65, 2011.

[7] N. Y. Agafanova and e. al, "Measurement of the Velocity of Neutrinos from the CNGS Beam with the Large Volume Detector," *Physical Review Letters,* vol. 109, no. 7, p. 070801, 2012.

[8] J. R. Lakowicz, Introduction to Flourescence, New York: Springer, 2006.

[9] D. Thornton, B. Stappers, M. Bailes, B. Barsdell, S. Bates, N. Bhat, M. Burgay, S. Burke-Spolaor, D. Champion, P. Coster, N. D'Amico, A. Jameson, S. Johnston, M. Keith, M. Kramer, L. Levin, S. Milia, C. Ng, A. Possenti and W. Straten, "A Population of Fast Radio Bursts at Cosmological Distances," *Science,* vol. 341, no. 6141, pp. 53-56, 2013.

[10] W. Wells, R. Stone and E. Miles, "Secure communications by optical homodyne," *IEEE Journal on Selected Areas in Communication,* vol. 11, no. 5, pp. 770-777, 1993.

[11] A. O. Wiberg, D. J. Esman, L. Liu, J. R. Adleman, S. Zlatanovic, V. Ataie, E. Myslivets, B. Kuo, N. Alic, E. W. Jacobs and S. Radic.

[12] R. H. Walden, "Analog-to-digital converter survey and analysis," *IEEE Journal on Selected Areas of Communication,* vol. 17, pp. 539-550, 1999.

[13] B. Murmann, "ADC Performance survey," 2016. [Online]. Available: http://web.stanford.edu/~murmann/adcsurvey. [Accessed 9 January 2017].

[14] G. C. Valley, "Photonic analog-to-digital converters," *Optics Express,* vol. 15, pp. 1955-1982, 2007.

[15] D. J. Esman, A. O. Wiberg, E. Temprana, E. Myslivets, B. P.-P. Kuo, N. Alic and R. S., "A Fully Frequency Referenced Parametric Polychromatically Sampled Analog-to-Digital Conversion," in *Conference on Optical Fiber Communication,* San Francisco, 2014.

[16] M. Skold, M. Westlund, H. Sunnerud and P. A. Andrekson, "100 GSample/s optical real-time sampling system with nyquist-limited bandwidth," in *European Conference on Optical Communications,* Berlin, 2007.

[17] A. Wiberg, C.-S. Bres, B.-P. Kuo, J. Chavez Boggio, N. Alic and S. Radic, "Polychromatic Sampling for High-Speed Real-Time Processing," in *Optical Fiber Communication Conference,* San Diego, 2010.

[18] D. J. Esman, A. O. Wiberg, N. Alic and S. Radic, "Highly Linear Broadband Photonic-Assisted Q-Band ADC," *Journal of Lightwave Technologies,* vol. 33, no. 11, pp. 2256-2262, 2015.

[19] U. Meye-Baese, "Fourier Transforms," *Digital Signal Processing with Field Programmable Gate Arrays,* vol. 17, no. 4, pp. 417-464, 2014.

[20] G. W. Bewick, "Fast Multiplication: Algorithms and Implementation," *Ph.D. dissertation, Stanford University, Stanford, CA,* 1994.

[21] E. Pop, S. Sinha and K. E. Goodson, "Heat Generation and Transport in Nanometer-Scale Transistors," *Proceedings of IEEE,* vol. 94, no. 8, pp. 1587-1601,

2006.

[22] V. Ataie, D. J. Esman, B. P.-P. Kuo, N. Alic and S. Radic, "Subnoise detection of a fast random event," *Science,* vol. 350, no. 6266, pp. 1343-1346, 2015.

[23] R. A. Scholtz, "The spread spectrum concept," *IEEE Transactions on Communications,* Vols. COM-25, pp. 748-755, 1977.

[24] R. A. Scholtz, "The origins of spread-spectrum communications," *IEEE Transactions on Communications,* vol. 30, pp. 822-854, 1982.

[25] A. J. Viterbi, CDMA: Principles of Spread Spectrum Communication, Redwood City: Addison Wesley Longman Publishing Co., 1995.

[26] Y. Bouvier, M. Nagatani, H. Nosaka, K. Kurishima, N. Kashio, M. Ida and K. Murata, "A 100-Gbps low-power PRBS generator based on a half-rate clock architecture using InP HBTs," in *Proceedings of IEEE MTT-S International Microwave Symposium*, 2014.

[27] J. Proakis, Digital Communications, McGraw-Hill, 2012.

[28] J. D. Choi and W. E. Stark, "Performance of ultra-wideband communications with suboptimal receivers in multipath channels," *IEEE Journal of Selected Areas in Communications,* vol. 20, no. 9, pp. 1754-1766, 2002.

[29] A. Goldsmith, Wireless Communications, Cambridge University Press, 2005.

[30] H. V. Sorensen, M. T. Heideman and C. S. Burrus, "On Computing the split-radix FFT," *IEEE Transactions on Acoustics, Speech and SIgnal Processing,* vol. 34, no. 1, pp. 152-156, 1986.

[31] S. N. Tang, J. W. Tsai and T. Y. Chang, "A 2.4-GS/s FFT processor for OFDM-based WPAN applications," *IEEE Transactions on Circuits and Systems II,* vol. 57, no. 6, pp. 451-455, 2010.

[32] H. L. Hurd, An Investigation of periodically correlated stochastic processes, Durham, HC: Ph.D. Dissertaion, Duke University, 1969.

[33] W. A. Gardner, A. Napolitano and L. Paura, "Cyclostationarity: Half a century of research," *Signal Processing,* vol. 86, no. 4, pp. 639-697, 2006.

[34] A. Vecchia, "Periodic autoregressive-moving average (PARMA) modeling with applications to water resources," *Water Resources Bulletin*, vol. 21, no. 5, pp. 721-730, 1985.

[35] Y. P. Dragan and I. Yayorskii, "The periodic correlation-random field as a model for bidimensional ocean waves," *Peredacha Informatsii*, vol. 51, pp. 15-25, 1982.

[36] P. Bloomfield, H. L. Hurd and R. B. Lund, "Periodic Correlation in Statospheric Ozone Data," *Journal of Time Series Analysis*, vol. 15, no. 2, pp. 127-150, 1994.

[37] D. Konig and J. R. Bohme, "Application of cyclostationary and time-frequency signal analysis to car engine diagnosis," *Acoustics, Speech, and Signal Processing*, vol. 4, pp. 149-152, 1994.

[38] T. Li, T. Qui and H. Tang, "Optimum heart sound signal selection based on teh cyclostationary property," *Computers in Biology and Medicine*, vol. 43, pp. 607-612, 2013.

[39] E. Parzen and M. Pagano, "An approach to modeling seasonally stationary time series," *Journal of Econometrics*, vol. 9, pp. 137-153, 1979.

[40] A. Tkachenko, D. Cabric and R. W. Brodersen, "Cyclostationary Feature Detector Experiments using Reconfigurable BEE2," in *Proceeedings from IEEE International Symbosium on New Frontiers in Dynamic Spectrum Access Networks*, Dublin, 2007.

[41] T. Yucek and H. Arslan, "A survey of spectrum sensing algorithms for cognitive radio applications," *IEEE Communication Surveys Tutorials*, vol. 75, no. 1, pp. 325-342, 2003.

[42] R. S. Roberts, Architectures for Digital Cyclic Spectral Analysis, Davis: Ph.D. Dissertation, University of California, Davis, 1989.

[43] W. A. Gardner, Cycostationarity in Communications and Signal Processing, New York: IEEE Press, 1994.

[44] A. I. A. Kyouwoong Kim, "Cyclostationary Approaches to Signal Detection and Classification in Cognitive Radios," *DySPAN 2nd IEEE International Symposium*, pp. 212-215, 2007.

[45] K. Siwiak and D. McKeown, Ultrawideband Radio Technology, Chichester: John Wiley, 2004.

[46] K. Siwiak, "Ultra-Wideband Radio: Introducing a New Technology," in *Vehicular Technology Conference*, 2001.

[47] R. A. Scholtz, "Multiple Access with Time-Hopping Impulse Modulation," *MILCOM 93*, p. 1, 1993.

[48] M. Z. Win and R. A. Scholtz, "Ultra-Wide bandwidth time-hopping spread-spectrum impulse radio for wireless multiple-access communications," *IEEE Transactions on Communications*, vol. 48, no. 4, pp. 679-691, 2000.

[49] A. Lopez-Salcedo and G. Vazquez, "Detection of PPM-UWB Random Signals," *IEEE Transactions on Signal Processing*, vol. 56, no. 5, pp. 2003-2016, 2008.

[50] G. S. Biradar, S. N. Merchant and U. B. Desai, "An adaptive frequency and time hopping PPM UWB for multiple access communication," in *Proceedings of IEEE Conference on Information Communications*, Singapore, 2007.

[51] "First Report and Order, Revision of Part 15 of the Commision's Rules Regarding Ultra-Wideband Transmission Systems," FCC, ET Docket 98-153, Washington, DC, 2002.

[52] T. Muoi and J. Hullett, "Receiver Design for Optical PPM Systems," *IEEE Transactions on Communications*, vol. 26, p. 295, 1978.

[53] K. Stadius, T. Rapinoja, J. Kaukoyuori, J. Ryynanen and K. A. I. Halonen, "Multitone Fast Frequency-Hopping Synthesizer for UWB Radio," *IEEE Transactions on Microwave Theory and Technologies*, vol. 55, no. 8, pp. 1633-1641, 2007.

[54] W. M. Tolles, J. W. Nibler, J. R. McDonald and A. B. Harvey, "A review of the theory and application of coherent anti-stokes Raman spectroscopy," *Applied Spectroscopy*, vol. 31, pp. 253-271, 1977.

[55] C. Weitkamp, Lidar: Range-Resolved Optical Remote Sensing of the Atmosphere, New York: Springer, 2006.

[56] R. N. McDonough and A. D. Whalen, Detection of Signals in Noise, Academic

Press, 1995.

[57] R. A. Posel, Modern Communications Jamming, Boston: Artech House, 2011.

[58] B. McNamara and K. Wieseneld, "Theory of Stochastic Resonance," *Physical Review A,* vol. 49, no. 9, pp. 4854-4869, 1989.

[59] A. Jolly, J. F. Gleyze and J. C. Jolly, "Static and synchronized switching noise management of replicated optical pulse trains," *Optical Communications,* vol. 264, pp. 89-96, 2006.

[60] W. R. Donaldson, J. R. Marciante and R. G. Roides, "An optical replicator for single shot measurements at 10 GHz with a dynamic range of 1800:1," *IEEE Journal on Quantum Electronics,* vol. 46, pp. 191-196, 2010.

[61] G. P. Agrawal, Nonlinear Fiber Optics, San Diego: Academic Press, 2004.

[62] L. F. Mollenauer, R. H. Stolen and J. P. Gordon, "Experimental observation of picoseconds pulse narrowing and solitons in optical fibers," *Phys. Rev. Lett.,* vol. 45, no. 13, pp. 1095-1098, 1980.

[63] M. Cronin-Golomb, J. O. White, B. Fischer and A. Yariv, "Exact solution of a nonlinear model of four-wave mixing and phase conjugation," *Opt. Lett.,* vol. 7, no. 7, pp. 313-315, 1982.

[64] Y. Chen, "Four-wave mixing in optical fibers: exact solution," *J. Opt. Soc. Am. B,* vol. 6, no. 11, pp. 1986-1993, 1989.

[65] S. T. Cundiff and J. Ye, "Colloquium: Femtosecond Optical Frequency Combs," *Review of Modern Physics,* vol. 75, no. 1, pp. 325-342, 2003.

[66] A. Bartels, D. Heinecke and S. Diddams, "Passively mode-locked 10 GHz femtosecond Ti:sapphire laser," *Optics Letters,* vol. 33, no. 16, pp. 1905-1907, 2008.

[67] P. Del'Haye, O. Arcizet, A. Schliesser, R. Holzwarth and T. Kippenberg, "Full stabilization of a microresonator-based optical frequency comb," *Physical Review Letters,* vol. 101, no. 053903, pp. 053903-1-053903-4, 2008.

[68] J. Pfeifle, M. Lauermann, D. Wegner, J. Li, K. Hartinger, V. Brasch, T. Herr, D. Hillerkuss, R. M. Schmogrow, T. Schimmel, R. Holzwarth, T. J. Kippenberg, J.

Leuthold, W. Freude and K. Christian, "Microresonator-based frequency comb generator as optical source for coherent WDM transmission," in *Optical Fiber Communication Conference*, Anaheim, 2013.

[69] R. Wu, V. R. Supradeepa, C. M. Long, D. E. Leaird and A. M. Weiner, "Generation of very flat optical frequency combs from continuous-wave lasers using cascaded intensity and phase modulators driven by tailored radio frequency waveforms," *Optics Letters*, vol. 35, no. 19, pp. 3234-3236, 2010.

[70] L. P. Barry, R. Watts, E. Martin, C. Browning, K. Merghem, C. Calò, A. Martinez, R. Rosales and A. Ramdane, "Characterization of optical frequency combs for OFDM based optical transmission systems," in *International Conference on Fibre Optics and Photonics*, Chennai, 2012.

[71] B. P.-P. Kuo, E. Myslivets, N. Alic and S. Radic, "Self-seeded 1-to-60 Multicasting in a Two-pump Parametric," in *Optical Fiber Communication Conference*, Los Angeles, 2011.

[72] V. Ataie, E. Myslivets, B. P.-P. Kuo, N. Alic and S. Radic, "Spectrally equalized freqeuncy comb generation in multistage parametric mixer with nonlinear pulse shaping," *Journal of Lightwave Technology*, vol. 32, no. 4, pp. 840-846, 2014.

[73] T. Kobayashi, H. Yao, K. Amano, Y. Fukushima, A. Morimoto and T. Sueta, "Optical Pulse Compression Using High-Frequency Electrooptic Phase Modulation," *IEEE Journal of Quantum Electronics*, vol. 24, no. 2, pp. 382-387, 1988.

[74] Y. Liu, Z. Lv, Y. Dong and Q. Li, "Research on stimulated Brillouin scattering suppression based on multi-frequency phase modulation," *Chinese Optics Letters*, vol. 7, no. 1, pp. 29-31, 2009.

[75] J. M. C. Boggio, J. D. Marconi and H. L. Fragnito, "Experimental and numerical investigation of the SBS-threshold increase in an optical fiber by applying strain distribution," *Journal of Lightwave Technologies*, vol. 23, no. 11, pp. 3808-2814, 2005.

[76] E. Myslivets, C. Lundström, J. M. Aparicio, S. Moro, A. O. Wiberg, C. S. Bres, N. Alic, P. A. Andrekson and S. Radic, "Spatial Equalization of Zero-Dispersion Wavelength Profiles in Nonlinear Fibers," *IEEE Photonic Technology Letters*, vol. 21, no. 24, pp. 1807-1809, 2009.

[77] D. C. Rife and R. R. Boorstyn, "Single-Tone Parameter Estimation from Discrete-Time Observations," *IEEE Transactions of Information Theory,* vol. 20, no. 5, pp. 591-598, 1974.

[78] A. V. Oppenheim and R. W. Schafer, Discrete-Time Signal Processing, Pearson, 2010.

[79] B. P. Kuo, E. Myslivets, V. Ataie, E. Temprana, N. Alic and S. Radic, "Wideband parametric frequency comb as coherent optical carrier," *Journal of Lightwave Technologies,* vol. 31, no. 21, pp. 3414-3419, 2013.

[80] J. B. Allen, "Short Term Spectral Analysis, Synthesis, and Modification by Discrete Fourier Transform," *IEEE Transactions On Acoustics, Speech and Signal Processing,* Vols. ASSP-25, no. 3, pp. 235-238, 1977.

[81] Y. Rozanov, Probability Theory, Random Processes and Mathematical Statistics, Netherlands: Springer, 1995.

[82] G. W. Anderson, D. C. Webb, A. E. Spezio and J. N. Lee, "Advanced channelization for RF, microwave, and millimeterwave applications," *Proceedings of the IEEE,* vol. 79, no. 3, pp. 355-388, 1991.

[83] S. Cao, J. Chen, J. N. Damask, C. R. Doerr, L. H. G. Guiziou, Y. Hibino, H. Li, S. Suzuki, K.-Y. Wu and P. Xie, "Interleaver Technology: Comparisons and Applications Requirements," *Journal of Lightwave Technologies,* vol. 22, no. 1, pp. 281-289, 2004.

[84] Z. Tong and S. Radic, "Low-noise optical amplification and signal processing in parametric devices," *Advances in Optics and Photonics,* vol. 5, pp. 318-384, 2013.

[85] Y. Hida, Y. Hibino, T. Kitoh, Y. Inoue, M. Itoh, T. Shibata and A. Himeno, "400-channel 25-GHz spacing arrayed-waveguide grating covering a full range of C- and L-bands," in *Optical Fiber Communication Conference,* Anaheim, 2001.

[86] N. K. Fontaine, X. Liu, S. Chandrasekhar, R. Ryf, S. Randel, P. Winzer, R. Delbue, P. Pupalaikis and A. Sureka, "Fiber Nonlinearity Compensation by Digital Backpropagation of an Entire 1.2-Tb/s Superchannel Using a Full-Field Spectrally-Sliced Receiver," in *European Conference on Optical Communications,* London, 2013.

[87] N. K. Fontaine, R. P. Scott, L. Zhou, F. M. Soares, J. P. Heritage and S. J. B. Yoo, "Reat-time full-field arbitrary optical waveform measurement," *Nature Photonics,* vol. 4, pp. 248-254, 2010.

[88] F. Herzog, K. Kudielka, D. Erni and W. Bachtold, "Optical phase locking by local oscillator phase dithering," *IEEE Journal on Quantum Electronics,* vol. 42, pp. 973-985, 2006.

[89] S. Kay, "A Fast and Accurate Single Frequency Estimator," *IEEE Transactions on Acoustics, Speech and Signal Processing,* vol. 37, no. 12, pp. 1987-1990, 1989.

[90] W. A. Gardner, W. A. Brown III and C.-K. Chen, "Spectral Correlation of Modulated Signals: Part II-Digital Modulation," *IEEE Transactions on Communications,* vol. 35, no. 6, 1987.